

Sheffield Hallam University

Elemental analysis of glass optical fibres with high spatial resolution.

PUGH, Andrew.

Available from the Sheffield Hallam University Research Archive (SHURA) at:

<http://shura.shu.ac.uk/20251/>

A Sheffield Hallam University thesis

This thesis is protected by copyright which belongs to the author.

The content must not be changed in any way or sold commercially in any format or medium without the formal permission of the author.

When referring to this work, full bibliographic details including the author, title, awarding institution and date of the thesis must be given.

Please visit <http://shura.shu.ac.uk/20251/> and <http://shura.shu.ac.uk/information.html> for further details about copyright and re-use permissions.



Sheffield City Polytechnic Library

REFERENCE ONLY

ProQuest Number: 10700896

All rights reserved

INFORMATION TO ALL USERS

The quality of this reproduction is dependent upon the quality of the copy submitted.

In the unlikely event that the author did not send a complete manuscript and there are missing pages, these will be noted. Also, if material had to be removed, a note will indicate the deletion.



ProQuest 10700896

Published by ProQuest LLC (2017). Copyright of the Dissertation is held by the Author.

All rights reserved.

This work is protected against unauthorized copying under Title 17, United States Code
Microform Edition © ProQuest LLC.

ProQuest LLC.
789 East Eisenhower Parkway
P.O. Box 1346
Ann Arbor, MI 48106 – 1346

ELEMENTAL ANALYSIS OF GLASS OPTICAL FIBRES WITH HIGH
SPATIAL RESOLUTION

ANDREW PUGH BSc(Hons) ARCS

A Thesis submitted in partial fulfilment of the
requirements of the Council for National Academic Awards for
the degree of Doctor of Philosophy

December 1991

Sheffield City Polytechnic in collaboration with British
Telecom Research Laboratories, Martlesham Heath

Elemental Analysis of Glass Optical Fibres With High
Spatial Resolution

This thesis is based on an investigation carried out at Sheffield City Polytechnic between November 1988 and November 1991 under the supervision of Dr R P Stratton and Dr D B Lewis of Sheffield City Polytechnic and B J Ainslie of British Telecom Research Laboratories.

In support of the programme of work an intensive short course at the University of Surrey was attended entitled "Analytical Electron Microscopy" as was a Polytechnic M.Sc. module entitled "Magnetic and Optical Materials"

The results presented in this thesis are, to the best of my knowledge, original except where reference has been made to other authors or institutions.

No part of this thesis has been submitted for any other degree at any other college or university.

Andrew Pugh

December 1991

Abstract

The properties of glass optical fibres are very strongly dependent on the elemental concentration profiles of the fibre cores. Core dopants such as germanium define the core refractive index, which in turn defines the manner in which the light is transmitted through the fibre. Erbium in fibre cores can facilitate the operation of fibre lasers and aluminium in turn can control the erbium distribution.

The aim of the project described in this thesis was to measure the elemental concentration profiles in a variety of fibre cores using X-ray microanalysis in an electron microscope. Conventional X-ray microanalysis of bulk samples has an analytical resolution in the order of a micron. With monomode optical fibre cores having cores typically three microns in diameter the resolution of the conventional technique is plainly inadequate.

An experimental technique has been developed for the preparation of thin cross-sectional samples of glass optical fibres. Application of this technique has facilitated the preparation and analysis of thin film specimens with an average thickness of 400 microns. This approach has allowed analysis to be performed with an effective spatial resolution of 100-300 nm.

The technique has been applied to the determination of germanium concentration in Raman fibres, to the investigation of erbium confinement in erbium doped fibres and to the investigation of inter-ionic diffusion in semiconductor doped fibres.

It has been shown that the germanium, and hence refractive index, profile of germanium doped fibres is not changed by the process of fibre drawing. Evidence has been gathered supporting the theory of erbium confinement by aluminium and an important degree of elemental diffusion has been shown to take place during the drawing of semiconductor doped fibres.

In addition an experimental technique has been developed for the preparation of thin cross-sectional samples of glass optical fibres.

Acknowledgement

I would like to express my thanks to British Telecom Research Labs, Martlesham Heath for financial assistance and supply of fibre.

Thanks are also due to B J Ainslie (British Telecom Research Laboratories), Dr R P Stratton (Sheffield City Polytechnic) and Dr D B Lewis (Sheffield City Polytechnic) for their help and advice and to Dr H V Atkinson (Sheffield University) for her involvement in the early stages of the project.

Funding from the National Advisory Board is also gratefully acknowledged.

1	Introduction and Aims of the Investigation	10
2	Literature Review	12
2.1	Introduction	12
2.2	Light Guiding by Optical Fibres	14
2.3	Structure of Practical Optical Fibres	15
2.4	Physical and Microstructural Properties of Glass	16
2.4.1	Multicomponent Glasses	18
2.4.2	Diffusion in Glasses	19
2.5	Optical Properties of Glasses	24
2.5.1	Dispersion	24
2.5.2	Absorption	25
2.5.2.1.	Intrinsic Loss Mechanisms	26
	Intrinsic Absorption	26
	i) Electronic Transitions	26
	ii) Lattice Vibrations	26
	Intrinsic Scattering	27
	i) Rayleigh Scattering	27
	ii) Turbidity	28
2.5.2.2.	Extrinsic Absorption	28
	i) Impurity Absorption	28
	ii) Scattering due to Structural Imperfections	29
2.5.3	Summary of Fibre Attenuation Mechanisms	30
2.6	Specialised Optical Fibres	30
2.6.1	Raman Fibres	30
2.6.2	Erbium Doped Fibres	32
2.6.3	Semiconductor Doped Fibres	33
2.7	Manufacture of Optical Fibres	36

2.7.2 Fibre Drawing	40
2.8 Overview of Electron Microscopy	41
2.8.1 Electron Beam/Specimen Interactions	41
2.8.2 Specimen Coating	47
2.8.3.1 Conventional TEM	47
2.8.3.2 Scanning Transmission Electron Microscopy	48
2.8.3.3 Scanning Electron Microscopy	49
2.9 X-Ray Analysis	50
2.9.1 Energy Dispersive X-Ray Analysis	51
2.9.2 Wavelength Dispersive Spectrometry	54
2.9.3 Quantitative Analysis	56
2.9.4 Detection Limits	58
2.10 Ion-Beam Thinning	59
3 Experimental Procedure	63
3.1 Sample Preparation	64
3.1.1 Initial Technique	65
3.1.2 Development of Experimental Technique	66
3.1.3 Final Technique	70
3.1.4 Preparation of Bulk Samples of Preform	73
3.2 Examination of Samples	74
3.2.1 Concentration Profile Acquisition	74
3.3 Evaluation of the Experimental Technique	77
3.3.1 Calibration of Microscope Magnification	77
3.3.2 Determination of Effective Spot Size	78
3.3.3 Determination of Sample Thickness	79
3.3.4 Determination of Effectiveness of Scan Rotate Module	79

4 Experimental Results	80
4.1 Evaluation of the Experimental Technique	80
4.1.1 Calibration of Microscope Magnifications	80
4.1.2 Determination of Effective Probe Size	81
4.1.3 Limits of Detectability	82
4.1.4 Effectiveness of Scan Rotate Module	82
4.2 Raman Fibres	83
4.3 Erbium Doped Fibres	84
4.4 Semiconductor Doped Fibres	85
4.5 Investigation of Fibre Draw-Down Region	89
5 Discussion	90
5.1 Evaluation of the Experimental Technique	90
5.1.1 Calibration of Microscope Magnification	90
5.1.2 Effective Probe Size	92
5.1.3 Limits of Detectability	94
5.1.4 Effects of the Scan Rotate Module	98
5.1.5 Evaluation of the Experimental Technique; Conclusions	100
5.2 Raman Fibres	101
5.3 Erbium Doped Fibres	104
5.4 Semiconductor Doped Fibres	109
5.4.1 Interdiffusion Model for Potassium and Sodium	118
5.5 Fibre Draw-Down Region	121
6 Conclusions	124
6.1 Experimental Procedure	124
6.2 Fibre Investigations	124
7 Suggestions for Further Work	126
References	129

Figures

147

Appendix 1; Data Acquisition Program

Appendix 2; Data Manipulation and Plotting Program

Appendix 3; Analogue/Digital Converter Circuit

Chapter 1

Elemental Analysis of Glass Optical Fibres With High Spatial Resolution.

Aims of the Investigation

Optical fibres consist of long filaments of silica glass of extreme purity and transparency. Their operation relies on the refractive index differences between their core and cladding regions. This refractive index variation is controlled by doping the core glass with precise quantities of other elements such as germanium and phosphorus.

The long interaction length and tight confinement of light in optical fibres make them ideal hosts for a variety of non-linear optical phenomena such as the optical Kerr effect and stimulated Raman scattering. Optical fibres also make excellent laser cavities and their flexibility allows the laser cavity to be both extremely long and very compact.

The optical properties of fibres are very strongly dependent on the composition and dopant levels of the glass, but as a typical single mode fibre core diameter is $5\mu\text{m}$ conventional analytical techniques cannot achieve sufficiently high spatial resolution to investigate these properties.

The aim of this project, therefore, was to develop an experimental procedure to prepare and analyse samples of standard telecommunications type fibre. In addition the technique has been applied to a variety of fibres to demonstrate the effectiveness of this experimental procedure.

The following objectives have been achieved.

- 1) The development of a technique for the preparation of optical fibres for examination by transmission electron microscopy.
- 2) The development of computer hardware and software to facilitate the acquisition, storage, manipulation and display of compositional information gained from such samples.
- 3) The investigation of refractive index profiles in germanium doped fibres in order to discover any departures from the refractive index profile of the fibre preform.
- 4) The investigation of erbium confinement in fibre cores by interaction with aluminium.
- 5) The investigation of ionic interdiffusion during fibre drawing and subsequent heat treatment of semiconductor doped fibres.
- 6) The investigation of refractive index profile variation in the preform neck-down region.

Chapter 2

Literature Review

This literature review will first explain the reasons for the development of optical fibres. This will be followed by a brief description of the mechanism of their lightguiding properties and a description of the structure of practical optical fibres. This will be followed by reviews of the microstructural and optical properties of silica glass. A section will then follow describing the salient features of the specialised optical fibres investigated during the course of this project and a further section will then be included on the manufacture of such fibres. The literature survey will be concluded with a review of electron microscopy, x-ray analysis and ion-beam thinning.

2.1 Introduction

The use of light as a means of communication is not a new idea, bonfires on hilltops were used at least 400 years ago and, more recently, the Photophone of Alexander Graham Bell used a mirror mounted on a diaphragm to modulate a beam of sunlight and so transmit speech.

Interest in light for data transmission stems from the increase in bandwidth made available by an increase in the frequency of the carrier wave. The entire long wave radio spectrum can only accommodate around 100 music channels whereas an optical fibre working in the relatively narrow range from 1.5 to 1.51 μm could, in principle carry tens of millions of such music channels. Computer data links with

DX 97015 . Page count 184
Batch number 524

Comments:

INSTITUTION COPY

Institution SHEFFIELD POLYTECHNIC (CNAA)

Thesis by PUGH. A.

We have assigned this thesis the number given at the top of this sheet.

CNAA has been notified, and will pass the information on to ASLIB on your behalf so that it can be published with the relevant abstract in their *Index to Theses with Abstracts*.

THE BRITISH LIBRARY
DOCUMENT SUPPLY CENTRE

British Thesis Acquisitions

very high data rates and low interference susceptibility are also well suited to optical fibre technology, the fibre described above has been demonstrated to transmit data at frequencies in excess of 10 GHz. In comparison the highest data transfer rate usually used with copper wire pairs is 9600 bits per second.

To use light as a transmission medium, however, it has to be guided in some way. Simply broadcasting with light in the same way as a radio system is obviously impractical. Around 1959 Goubau and others investigated some candidate waveguides, namely iris waveguides [1], lens waveguides [2] and waveguides using convectionally distorted gasses [3] in an attempt to find a practical lightguide. (Interestingly the iris waveguide can have losses as low as 1dB/km but it is unable to accommodate changes in beam direction.)

Glass fibres were not at first considered practical as the glasses available at the time had attenuations in the region of 1000dB/km, two orders of magnitude higher than the maximum of 20dB/km acceptable for a practical communications system.

The advance which spawned the development of glass optical fibre communication systems came in 1970 when Kapron et al announced the development of the first glass fibre with losses less than this threshold value [4]. This caused an increase in interest in optical fibres such that losses were reduced to less than 7dB/km within two years [5]. Fibres are now routinely made with losses as low as 0.16 dB/km [6].

In silica glass fibres the low loss region is confined to two windows in the infrared at 1.2-1.32 μ m and 1.45-1.6 μ m and

so the available bandwidth is not as high as would be expected simply from consideration of the frequency of the carrier wave.

The ability of optical fibres to transmit several different data channels down each fibre, their small size and low cost relative to copper wires has obvious attractions to telecommunications companies and has led to their rapid adoption for trunk routes.

2.2 Light Guiding By Optical Fibres

A full explanation of light propagation in optical fibres requires the solution of Maxwell's equations in a cylindrical geometry. A qualitative understanding can, however, be gained from consideration of geometrical optics.

The simplest class of fibres, step index fibres can be explained on the basis of total internal reflection (See Fig 1).

Snell's law states that for a light ray propagating in a medium of refractive index n_1 , incident on a boundary with a medium of refractive index n_2 , at an angle θ_1 to the interface, then it will propagate in the second medium at an angle θ_2 to the interface such that

$$\frac{\cos\theta_1}{\cos\theta_2} = \frac{n_1}{n_2} \dots\dots\dots 2.1$$

It can be seen from the above equation that if $n_2 < n_1$, then for a small enough value of θ_1 , θ_2 is no longer defined. The physical meaning of this is that the light energy does not propagate into the second medium but is totally internally reflected back into the first medium. The geometry of an

optical fibre is such that within a very short distance into the fibre only the light rays travelling at small enough angles to the axis remain and these are confined within the fibre and propagate along it.

2.3 Structure of Practical Optical Fibres

A more rigorous application of the laws of optics shows that only the real part of the wave is undefined in the lower index material and that the imaginary part of the wave does exist on the far side of the interface as a rapidly decaying evanescent wave. This means that a significant proportion of the transmitted power travels outside the simple fibre considered above. To minimise attenuation it is important for this light energy to propagate in a medium of similar transparency to the fibre and so fibres are normally made with a core of high refractive index glass surrounded by a cladding with a lower index. This cladding layer also protects the reflecting surface of the core from damage which would impair performance and prevents light transferring into adjacent fibres. Such a core/cladding structure is known as a step index fibre, from the shape of the refractive index profile.

Fibres with cores in the region of five microns in diameter are referred to as monomode fibres whereas those with larger cores are multimode fibres. The distinction between the two will be explained in section 2.5.1.

Glass fibres as drawn are very strong, but, as the failure mechanism is brittle fracture, the slightest flaw in the pristine fibre surface can lead to a marked decrease in

the fibre strength. To prevent such damage fibres are coated with a protective layer. This is normally an ultra-violet or thermally curing polymer, although nickel, aluminium, indium, carbon and tin have also been tried as hermetic coatings by various workers [7].

2.4 Physical and Microstructural Properties of Glass

The glasses investigated in this project were, in the main, high silica glasses with small amounts of dopants such as fluorine and phosphorous and moderate amounts of germanium in the cores.

The presently accepted structure for silica glasses was first proposed by Zacharisen in 1932 [8]. In this model each silicon atom is surrounded by four oxygen atoms in a tetrahedron. These tetrahedra are joined together in an aperiodic lattice to form the glass. This structure has been verified by x-ray diffraction studies in terms of pair distribution functions by Mozzi and Warren [9]. These results are shown in Figure 2.

The first peak on the graph corresponds to the Si-O distance of 1.62\AA and the second to the O-O distance of 2.65\AA . Both these values are close to those found in crystalline silicates. The dotted curve in the diagram shows the calculated values expected for a tetrahedral arrangement. As can be seen the agreement is quite good up to the third peak, Si-Si at 3.12\AA . The broadening of the higher peaks is due to the distance variations induced by the variations in bond angles. This variation in bond angles is the cause of the

amorphous nature of silica glass and can be calculated from the width of the peaks. The Si-O-Si bond angle is found to peak at 144° with a maximum of 180° and a minimum of 120° . The majority of the bond angles are within 10% of the average.

Although the tetrahedral model works well at normal pressures it is known that six-co-ordinated silicon is found at high (geological) temperatures and pressures. NMR evidence [10] has also indicated the presence of small amounts of five-co-ordinated silicon in glasses at atmospheric pressures. These higher co-ordinations are also predicted at high temperatures by molecular dynamics studies [11] and are thought to be important for the viscous flow of silica.

In some earlier work Zarzycki [12] measured bond lengths and angles for both silica and germania. His silica results were in good agreement with the later results. His results for Germania bond lengths were Ge-O $1.70 \pm 0.05 \text{ \AA}$ and Ge-Ge $3.15 \pm 0.05 \text{ \AA}$ and a Ge-O-Ge bond angle of 125° to 152° . These values for the germania network are close enough to those of silica to allow for the homogeneous mixing of the two. This is very important for the manufacture of optical fibres where the refractive index profile is achieved by germanium doping and inhomogeneities or phase precipitation would ruin the optical properties.

Alternative structures for silica glass have been proposed consisting of very small crystallites and some evidence for this has been presented based on electron microscopy of very thin fibres drawn in the microscope column [13]. The validity of this data is questioned, however, by Seward [14] who

argues that the magnitude of the effects due to polycrystallinity would have to be unreasonably large to produce visible contrast in the TEM. X-ray diffraction studies also show that such crystallites can be no larger than 10\AA in diameter, at which scale the concept of a crystal has little meaning.

2.4.1 Multicomponent Glasses

As mentioned in the preceding section, Germanium atoms can substitute for silicon atoms in the network. The same is true for aluminium and phosphorus atoms if charge compensating ions are present.

Commercial glasses generally contain network modifiers to reduce both the viscosity of the glass melt and the melting temperature. These are generally oxides of the alkali or alkaline earth metals, most commonly Na_2O , K_2O or CaO . The effect of these is to introduce non-bridging oxygens into the silica network. These are oxygen atoms bonded to a cation instead of to another SiO_4 tetrahedron and the effect is to reduce the degree of cross-linking and hence rigidity of the silicate lattice. The silicate lattice structure is not seriously disrupted until the silicon-cation ratio reaches 1:1, below which point three out of four oxygens are still bridging. Most commercial glasses are soda-lime-silicate glasses made from Na_2O , CaO and SiO_2 in a 1:1:6 ratio.

Recent neutron scattering studies [15] have indicated that the distribution of cations in such glass mixtures is not, in fact, random but possesses considerable order over the

nanometre range.

2.4.2 Diffusion in Glasses

a) Ionic Diffusion

As in most other situations diffusion of ions in glass is governed by Fick's equation:-

$$J = \frac{D\partial C}{\partial x} \dots\dots\dots 2.2$$

where J is the flux of diffusing species per unit area at x, D is the diffusion coefficient and $\partial c/\partial x$ is the local concentration gradient of that species.

The most important factor governing diffusion is the diffusion coefficient, the value of which varies with diffusing species, matrix and temperature.

Measurement of diffusion coefficients in glasses can be done by use of radioactive tracers or by chemical analysis, but in the case of glasses and ionic conducting species it is more convenient to use electrical conductivity techniques.

The conductivity, σ , is given by Einstein's equation:-

$$\sigma = \frac{Z^2 F^2 D C}{RT} \dots\dots\dots 2.3$$

where Z is the charge of the conducting species, F is the Faraday constant (the product of the electronic charge and Avagadro's number), D is the diffusion coefficient, C the concentration, R the gas constant and T the temperature. The derivation of the equation relies on the equivalence of the electrical and diffusive mobilities and so is only as accurate as that assumption for the situation being investigated.

According to Doremus [16] diffusion in glasses cannot be based on the treatment of the glass as a viscous liquid as such an approach predicts too low a diffusion coefficient for the diffusion of cations such as potassium and sodium. As the cations also diffuse much more readily than the lattice elements diffusion in silicate glasses is better explained by the same processes as occur in ionic crystals.

In ionic crystals diffusion occurs by a defect mechanism and so the temperature dependence of the diffusion coefficient is described by an Arrhenius equation of the form:-

$$D \propto p \exp(-\Delta E/RT)$$

where ΔE is the activation energy for the diffusion process. p , the pre-exponential term is a constant equal to the number of interstitial sites available to each diffusing species.

This equation works well over small temperature ranges but it is found that above the glass transition temperature the apparent activation energy decreases. For sodium in vitreous silica, for example, the activation energy is found to be 146kJ/mol below 280°C and 100kJ/mol above 600°C [17].

Working on this basis a number of workers have measured the activation energies for diffusion of a number of species in a variety of glass matrices. Doremus [16] contains a summary of these results. It is found that the activation energy for the diffusion of sodium in a binary sodium silicate glass increases with decreasing sodium concentration which can be interpreted as being due to increased sodium mobility in an undisturbed silicate lattice.

The addition of higher-valent metal oxides also decreases ionic mobility. The largest effect is found for barium, with decreasing effects with lead, strontium and calcium. Addition of alumina to the mix increases the mobility of monovalent cations such as sodium, potassium and lithium but reduces the mobility of rare earths such as erbium [18].

The addition of another alkali to a glass already containing one alkali causes a sharp drop in the electrical conductivity of the glass. This is due to a decrease in the ionic mobility of each ion in the presence of another. The difference in conductivity between a glass containing only sodium and one containing equal amounts of sodium and potassium can be as much as two orders of magnitude.

Frischat [19] measured diffusion coefficients for calcium and aluminium in silicate glasses. He found that the diffusion coefficient of calcium was a factor of 400 less than that for sodium and that that for aluminium was eight orders of magnitude lower.

When a cation diffuses in a dielectric such as glass an electrical field is set up by the charge imbalance caused by that movement. This field builds up until it is of sufficient magnitude to prevent any further diffusion. If two glasses of different composition are placed in contact it is possible for this charge imbalance to be offset by the diffusion of a like charged species in the opposite direction. If the two diffusing species have different diffusion coefficients then two effects will occur; the faster moving species will set up

an electric field, which will slow down its rate of diffusion and at the same time this field will accelerate the diffusion of the slower moving ion in the other direction. Both species, therefore, will diffuse with a common diffusion coefficient somewhere between those of the two ions separately. To bring about this field a certain imbalance in the diffusion of the two species must occur, but this will be negligible compared to the total number of ions involved.

Therefore,

$$D_{\text{interdiffusion}} = \frac{D_a D_b}{N_a D_a + N_b D_b} \dots\dots (2.4)$$

where N_i is the mole fraction of the diffusing species i and D_i is its diffusion coefficient as measured by electrical conductivity methods.

b) Mathematics of Diffusion in Cylindrical Geometries

If Fick's equation (2.2) is formulated in terms of a three dimensional cylindrical geometry and written in terms of the time variation of the concentration at a point (r, θ, z) [20] the result is that :-

$$\frac{\partial C}{\partial t} = \frac{1}{r} \left\{ \frac{\partial}{\partial r} \left[r D \frac{\partial C}{\partial r} \right] + \frac{\partial}{\partial \theta} \left[\frac{D \partial C}{r \partial \theta} \right] + \frac{\partial}{\partial z} \left[r D \frac{\partial C}{\partial z} \right] \right\} \dots\dots (2.5)$$

where D is the diffusion coefficient and C the concentration.

In an optical fibre the geometry is such that the concentration gradient is only in the radial direction, so that the above expression can be simplified to :-

$$\frac{\partial C}{\partial t} = \frac{1}{r} \left\{ \frac{\partial}{\partial r} \left[r D \frac{\partial C}{\partial r} \right] \right\} \dots\dots (2.6)$$

This expression can be solved for an infinitely long cylinder of substance diffusing into a surrounding medium.

The solution to the equation is:-

$$C = \frac{C_0}{2Dt} e^{-r^2/4Dt} \int_0^a e^{-r'^2/4Dt} I_0\left(\frac{rr'}{2Dt}\right) r' dr' \dots\dots (2.7)$$

where C_0 is the uniform initial concentration in an area of radius a and I_0 is the modified Bessel function of the first kind of order zero.

This equation must be solved numerically at all points other than $r=0$, the core centre in the case of an optical fibre where it simplifies to :-

$$C = C_0(1 - e^{-a^2/4Dt}) \dots\dots (2.8)$$

Molecular Diffusion; Fining

An important stage in the production of bulk glass is the elimination of bubbles from the melt. This process is called fining.

Bubble elimination can occur either by the bubbles rising to the surface or by their dissolution into the melt.

For a typical glass melt the rate of rise for a 0.1mm diameter bubble is about 10cm/day, too slow to eliminate them in a normal situation. Small bubbles, therefore, must be eliminated by dissolution. Arsenic oxide is a common fining agent and works by reacting with oxygen dissolved in the glass, reducing the concentration of oxygen in the glass and so favouring the dissolution of oxygen out of the bubbles. It has been postulated that the reduction in oxygen concentration

favours the decomposition of carbon dioxide (a likely bubble former due to the prevalence of carbonates in the glass precursors) into carbon monoxide and oxygen. The carbon monoxide is a smaller molecule than carbon dioxide and should diffuse more readily. Fining is discussed in more detail than is necessary here in Doremus [16].

2.5 Optical Properties of Glasses

2.5.1 Dispersion

It can be seen in Figure 1 that there are a number of possible ray paths (Maxwell's equations show a finite number) all with differing optical path lengths and hence differing ray transit times. This results in dispersion - a well defined input pulse will be distorted as different components travel at different speeds relative to the fibre axis. This problem can be overcome in two ways. The first way is by the use of graded index fibres which have a refractive index profile similar to that shown in the diagram. Such a fibre still has a number of possible ray paths, but as the index is lower towards the edges of the fibre the speed of light is higher and it can be arranged that all modes have the same optical path length and hence no waveguide dispersion.

The second way to eliminate modal dispersion is to make the fibre core so small that only one mode can propagate, around $5\mu\text{m}$ is usual. This is the technique used in most long distance telecommunications systems. Most of the fibres investigated in this project were monomode fibres as the high resolution of the technique is more suited to their dimensions.

Another form of dispersion, material dispersion, is due to the frequency dependence of the refractive index of the fibre material. Any wavetrain of finite length consists of a number of different frequency components, which may travel at different speeds. In silica glass the material dispersion is zero around $1.3\mu\text{m}$, which, fortunately, coincides with the low intrinsic loss windows for silica at 1.3 and $1.5\mu\text{m}$.

It is possible to manipulate the waveguide dispersion by varying the waveguide design. As the material and waveguide dispersions are antagonistic this makes it possible to shift the zero dispersion wavelength of the fibre [21].

2.5.2 Absorption and Scattering Losses

The main barrier to the adoption of glass as a light transmission medium was its high optical absorption. To overcome this difficulty novel glass preparation techniques have been developed but attenuation is still one of the limiting factors in fibre design.

Absorption phenomena are characterised by the absorption coefficient α so that [22]:-

$$I_{\text{transmitted}} = I_{\text{initial}} \exp(-\alpha x) \dots \dots \dots 2.9$$

where x is the distance along the fibre and I refers to light intensity.

Absorption phenomena are customarily divided into two groups, intrinsic absorption and extrinsic absorption. Intrinsic absorption is, as the name suggests, intrinsic to the fibre material and is unavoidable. Extrinsic absorption is

due to other factors which can, to varying extents, be removed by judicious selection of manufacturing technology.

2.5.2.1 Intrinsic Loss Mechanisms

Intrinsic loss mechanisms include absorption phenomena due to electronic transitions and lattice vibrations and scattering phenomena due to Rayleigh scattering, Raman scattering and turbidity.

Intrinsic Absorption

i) Electronic transitions

Electronic transitions in atomic oxygen have absorption bands in the ultra violet and infrared.

The ultra violet absorption band has its tail in the 1-3 μ m region, close to the wavelengths used in infrared optical fibre systems.

The absorption coefficient for electronic transitions is given by the expression:-

$$\alpha = \nu_0 \exp(E - E_g) / E_0 \dots \dots \dots 2.10$$

where E is the photon energy ($h\nu$), E_g is the energy gap for the transition and E_0 is a constant.

ii) Lattice Vibrations

These are due to the excitement by the incident electromagnetic field of vibrational modes in molecules with a dipole moment. Si-O is strongly infra-red active and has a strong absorption at 9.0 μ m. This absorption band is what causes the increase in attenuation in silica based fibres above about 1.65 μ m.

Intrinsic Scattering

Intrinsic scattering processes include Rayleigh scattering, Raman scattering and Brillouin scattering.

Scattering in optical fibres leads to the coupling of light power into unbound modes and hence to the attenuation of the signal. Scattering therefore has the effect of a loss mechanism.

i) Rayleigh Scattering

Rayleigh scattering is the process by which light is scattered by inhomogeneities which are small relative to with the wavelength of the incident light.

The angular distribution of the scattered light is given by the equation [22]

$$I(\theta) = \frac{(1+\cos^2\theta)}{x^2} \cdot \frac{8\pi^4 r^6}{\lambda^4} \left| \frac{N^2-1}{N^2+1} \right|^2 I_0 \dots\dots\dots 2.11$$

where $I(\theta)$ is the scattered intensity at angle θ and distance x from a scattering particle of radius r with a substrate/particle refractive index ratio of N and incident intensity I_0 .

Any light scattered through an angle greater than the critical angle for the fibre will be lost.

From the above equation it can be seen that the total scattering loss is governed by the proportionality:-

$$\alpha \propto \frac{r^6}{\lambda^4} \left| \frac{N^2-1}{N^2+1} \right|^2 \dots\dots\dots 2.12$$

This indicates that one of the aims of fibre manufacture must be to minimise both the size of imperfections and the

refractive index difference between the core glass and any imperfections that might be present.

It can also be seen that the absorption has a λ^4 dependency which favours operation at long wavelengths, ie in the infra-red.

It has been found that some defect centres may be induced during the drawing process [23].

ii) Turbidity

When a glass melt is cooled below the glass transition temperature some of the turbulence of the melt is frozen in. This manifests itself as turbidity, random variations in density and refractive index on a scale such as to cause Rayleigh scattering. To minimise this the glass should be cooled as slowly as possible, a requirement at odds with the dynamics of fibre drawing where the hardening of the melt as the fibre is formed is one of the factors governing fibre size.

2.5.2.2 Extrinsic Absorption

Extrinsic absorption includes all attenuation factors which are due to factors unconnected with the fibre material.

i) Impurity Absorption

Impurity absorption is due to impurities introduced during fibre manufacture, the most important being transition metal ions (Figure 3) and water (Figure 4). It is found that it is necessary to reduce heavy metal impurities to less than 1ppt (10^{12}) in order to achieve very low loss fibre. Water has a very unfortunate absorption band at $1.4\mu\text{m}$ (The wavelength of

zero dispersion in silica) due to the first overtone of the O-H fundamental frequency at $2.8\mu\text{m}$. This means that all the gasses used in MCVD fabrication must be carefully dried first.

It has also been found that molecular hydrogen can diffuse into fibres after they have been drawn leading to the formation of O-H groups [24]. A variety of hermetic coatings have been tried in an attempt to minimise this effect which could be a problem in subaquatic cables [7].

To a good approximation impurity absorption follows the same equation as atomic lattice absorption.

ii) Scattering Due to Structural Imperfections

Structural imperfections lead to largely wavelength independent losses. Typical causes are boundary irregularity between core and cladding glasses, pores in the core and microbending in the fibre due to cabling. Microbending and small scattering centres may exhibit some wavelength dependency.

Boundary irregularity can be due to the manner in which the fibre is drawn [23] or due to physical and chemical differences between the two glasses. Differences in viscosity and T_g play an important role in determining the interface properties. Variation in core diameter can lead to considerable losses and so it is usual to have microprocessor monitoring of fibre thickness during the drawing process. Dianov [25] and Vasile'ev [26] have both studied the fibre drawing process in order to explain these thickness

variations.

2.5.3 Summary of Fibre Attenuation Mechanisms

The total loss can be formulated as a sum of five terms.

i) Electronic transitions $\approx C \exp(D/\lambda)$

ii) Lattice vibrations $\approx E(\lambda)$

iii) Impurity absorption $\approx F(\lambda)$

iv) Rayleigh scattering $\approx A/\lambda^4$

v) Structural imperfections $\approx B$

In silica glasses at around $1.3\mu\text{m}$ this simplifies to;

$$\alpha = (A/\lambda^4) + B \dots\dots 2.13$$

where A and B are constants obtainable experimentally.

The relative effects of the loss mechanisms are summed up in Figure 5.

2.6 Specialised Optical Fibres

In certain circumstances optical fibres deviate from the properties described above in order to capitalise on other properties of fibres. Examples include Raman fibres, Erbium doped fibres and Semiconductor doped fibres.

2.6.1 Raman Fibres

Raman fibres have cores of diameter 1-2 microns doped with high concentrations of GeO_2 . This core size is smaller than is usual in telecommunications fibre and is intended to increase the power density in the fibre core. Such fibres are designed to exploit the phenomenon of stimulated Raman scattering (SRS) in such devices as fibre Raman lasers [27,28]. The high level of germanium doping serves to

increase the Raman gain coefficient of the fibre as germania has a higher Raman gain coefficient than silica.

Stimulated Raman scattering (SRS) is one of a number of non-linear optical phenomena only seen at extremely high power densities before the advent of optical fibres. Non-linear optical phenomena are due to second, third and fourth terms in the governing equations of electromagnetic optics. The coefficients of these terms are very small and so the phenomena are normally only manifest at very high powers such as those produced by megawatt lasers. In optical fibres, however, the combination of high power density due to the tight confinement and interaction distances in the order of kilometres is sufficient to cause these phenomena at milliwatt powers. [29]

Raman scattering is due to the scattering of incident photons by interactions with high frequency optical phonons. SRS is generally undesirable in communications fibres but is potentially useful in fibre based devices such as lasers and amplifiers.

The effect of SRS is to create sidebands at lower and higher frequencies separated from the pump frequency by one Stokes shift. At high temperatures the two side bands are of equal intensity, and classically at absolute zero both sidebands disappear. In practice the lower (Anti-Stokes) will always appear as the incident pump can always scatter to produce a phonon and a Stokes photon.

A quantitative analysis of Stimulated Raman Scattering can be found in Stolen [30].

The Raman gain may be limited by chromatic dispersion. This causes the two pulses, Stokes and Pump, to separate as they are at different wavelengths.

Forwards SRS can never have more energy than the pump. This is not true for reverse SRS as it is constantly encountering fresh pump energy.[31]

2.6.2 Erbium Doped Fibres

In silica, erbium ions form a three level lasing system with a transition at $1.5\mu\text{m}$. This is one of the low loss windows used in optical fibre systems with silica fibres and makes erbium doped silica a very attractive material from which to manufacture fibre lasers. Unfortunately the solubility of erbium in silica is extremely low and even at relatively low concentrations the erbium ions cluster together and inhibit lasing [32]. Arai et al [18] have shown that the solubility of rare earths in silica can be increased by the use of either phosphorus or aluminium as a co-dopant and have prepared glasses containing up to 0.3 mol% Neodymium.

To increase the efficiency of the fibre lasers and amplifiers it is useful to confine the limited amount of erbium in the fibre to the centre region of the core where the majority of the intensity of the pump power is greatest thereby aiding inversion of the three level system [33]. It has been found that the Erbium is linked to the aluminium [34], and, as aluminium is largely immobile in a silica matrix, erbium confinement can be achieved by fabricating fibres in which the co-dopant is confined to this

central region.

Arai [18] proposes that the poor solubility of rare-earths in silica is due to the high co-ordination number of the cations, requiring a large number of non-bridging oxygens. As the concentration of non-bridging oxygens in pure silica is extremely low it is more energetically favourable for the cations to cluster together in an obscure co-ordination. Evidence for this unusual co-ordination is the peculiar absorption spectrum shown in the same paper. Aluminium and phosphorus added to the glass can act as network modifiers and increase the concentration of non-bridging oxygen, so increasing the solubility of the rare-earth.

As it is energetically more favourable for the rare-earth ions to co-ordinate with the alumina rich network than with other rare earth ions they are confined to that region.

2.6.3 Semiconductor Doped Fibres

In this study cores of semiconductor doped fibres are made of a commercially available filter glass coloured by small amounts of cadmium sulpho-selenide. This is a glass which, after heat treatment, forms small semiconducting microcrystallites 10-100Å in diameter [35] distributed through the glass matrix. These crystallites interact with light passing through the glass via zero-dimensional quantum confinement phenomena [36,37]. Light with photon energies in excess of the semiconductor bandgap is absorbed whereas light with lower energies passes through the glass. Incident photons produce electron-hole pairs in the microcrystallites. As the

de-Broglie wavelength of these pairs is in the order of the crystallite diameter the behaviour is highly non-linear. The most common use for these glasses is in very sharp cut-off optical filters [38] but recently interest has been focused on their potential as all-optical switches [39]. The very high optical nonlinearities of these glasses [40] also make them suitable hosts for a variety of phenomena from 4-wave mixing [41] through to optical phase conjugation [42] and stimulated Brillouin scattering [43,44].

The phenomenon of interest with respect to all-optical switching is the optical Kerr effect [30]. This effect relies on the fact that light passing through a material effects the refractive index of the material. At high optical power densities in bulk materials this leads to self focusing of the light beam [45]. In an optical fibre this self focusing effect is negligible in comparison to the lightguiding properties of the fibre structure but the refractive index variation can lead to phase shifts over long fibre lengths which can have important consequences.

All-optical switching relies on the fact that a polarised pump beam passing through a fibre can cause an optically controlled birefringence. (This means that the refractive index depends on the polarisation of the light being refracted).

In the optical Kerr effect the birefringence induced by an intense polarised pump is probed by a weaker signal at a different frequency polarised at 45° to the

birefringence. A polariser is set to eliminate the probe light in the absence of the pump. In the presence of the pump beam the induced birefringence of the fibre waveguide results in a rotation of the plane of polarisation of the probe beam and so allows its transmission through the polariser [46].

The response time of this switching technique is in the subnanosecond range [39].

Mechanics of Cd(S,Se) Crystallisation

The size of the crystallites in Cd(S,Se) doped glass is very important in determining the optical behaviour of the glass [47,48,49] and is readily varied by heat treatment.

According to Fuyu and Parker [49] the literature does not contain any detailed analyses of the early stages of nucleation and growth of these particles.

The important process from the point of view of crystallite size is a coarsening phenomenon described by Lifshitz and Slezov [50].

They showed that after a time t , with average initial particle size R_0 :-

$$R(t)^3 - R_0^3 = 8\gamma C_e D V_m t / 9RT \dots\dots\dots 2.14$$

where $R(t)$ is the average particle size at time t , $D = D_0 \exp(-\Delta E/kt)$ is the diffusion coefficient, γ is a coefficient describing a critical particle size, R is the gas constant and T is temperature.

It has also been found [51] that the chemical potential of oxygen in the melt is important when making such glass. If the

potential is too high (or low) then selenium (or cadmium) is lost by evaporation. The addition of zinc to the melt acts as a potential buffer and circumvents this problem.

The size distribution of the crystallites is critical in determining the position and sharpness of the optical cut-off. In optical switching situations it is important to have as sharp a cut-off as possible which requires a very narrow particle size distribution. To achieve this narrow distribution the fibre core must be as homogeneous with respect to chemical composition and heat treatment as possible.

2.7 Manufacture of Optical Fibres

Optical fibres are manufactured by a fibre drawing process in which a preform rod of high purity glass is fed into a zone furnace. This melts the end of the preform and the fibre is drawn from this softened region.

2.7.1 Preform Production

The first stage in the manufacture of an optical fibre is the preparation of the preform. A preform is typically about 1m long and 30mm in diameter. Many kilometres of fibre may be drawn from such a preform.

The refractive index profile of the fibre depends on that of the preform, and so any preform manufacturing technique must have the capacity to incorporate a radial refractive index difference. In optical fibres this refractive index difference between the core and the cladding is controlled by the addition of dopants to the glass. In the case of silica

fibres the core refractive index is generally raised by doping with germanium.

One of the simplest ways to make a preform for a step index fibre is the rod and tube method. With this method a rod of core glass is placed inside a tube of cladding glass and the two are drawn together into a fibre. This was the technique used for the fabrication of the semiconductor doped glass fibres used in this investigation, the cores of which were of a commercially available semiconductor doped glasses. This technique is only suitable for the manufacture of step index fibres. It can use most glasses provided the core and cladding materials are compatible and it is cheap but does not achieve the same level of glass purity as the vapour phase processes.

Modified Chemical Vapour Deposition, The MCVD Process

The MCVD process is a refinement of the "Soot" and Outside Vapour Deposition (OVD) processes [52] in which glass is made by the decomposition of gaseous precursors. The precursor gases used are generally chlorides of the glass formers, SiCl_4 , as the main component and GeCl_4 as a dopant to raise the refractive index. POCl_3 is used to provide phosphorus doping. This has the effect of lowering the sintering temperature of the glass by 200°C and thus avoids the problem of the substrate tube softening and distorting. The addition of phosphorus has the side-effect of raising the refractive index of the glass which is undesirable in the cladding layers. It has, however, been found [53] that the addition of fluorine doping can counteract

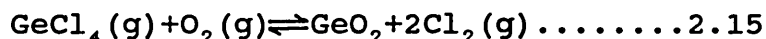
this effect. Fluorine is added by using a fluorinated hydrocarbon as one of the precursor gases.

In the OVD process the precursor gases undergo hydrolysis in an oxy-hydrogen flame which is played onto a mandrel. This produces a soot of fine glassy particles which are deposited on the mandrel to be later sintered into a solid glass preform. A similar process, Vapour Axial Deposition (VAD) is used to make fibres by some factories [7].

In the MCVD process oxygen and the precursor gases are fed down a substrate tube held between synchronously rotating chucks in a glassworking lathe. An external gas burner travelling axially along the substrate tube provides the heat for a high temperature oxidation reaction. (See Figure 6) This produces small particles ($<0.3\mu\text{m}$ in diameter) of extremely pure glass. These particles are formed by the Brownian coagulation of even smaller particles. Walker et. al. [54] investigated the deposition of these particles in the tube and concluded that they are driven towards the walls by thermophoresis. In this process small particles in a gas are driven down a temperature gradient due to the differences in the average kinetic energies of the gas molecules impinging on them. In the centre of the substrate tube the temperature gradient is purely axial and so particles formed in the centre regions are not deposited. This lowers the deposition efficiency of the process and also causes a finite taper to form in the deposited layers at the entry end of the tube as the hot zone can travel no further than the end of the tube and particles formed at this point are deposited some way

downstream.

The efficiency of the process is also limited by the reaction kinetics of the oxidation process. Whereas the phosphorus and silica are almost entirely oxidised, the Germanium oxidation equilibrium



is unfavourable at the temperatures at which the process is carried out and is made more so by the high concentration of chlorine from the other reactions shifting it to the left. There is also a tendency for the GeO_2 to decompose to GeO at higher temperatures. (This is covered in more detail in [7]).

The rate of particle growth and the final size of the particles depends strongly on the glass viscosity, and this is another respect in which phosphorus doping is advantageous.

The particulates so produced, when deposited downstream of the burner are sintered into a glassy layer by the burner as it passes down the tube to the site of their deposition [55,56,57]. The Preform is thus built up over many layers, the precise chemical composition of each layer being controlled by the proportions of precursor gases fed into the tube. It is thus possible to exercise a great deal of control over the refractive index profile, an example of this being the fabrication of Bragg fibres with alternating layers of high and low index [58].

2.7.2 Fibre Drawing

The next stage of the fibre manufacturing process is the drawing of the preform into fibre. This is accomplished by the use of a fibre drawing tower (See Figure 7). The preform is held in a furnace at the top of the tower. As the softening temperature of the glass can be as high as 2000°C the furnace is usually either a graphite or zirconia induction furnace, although oxy-hydrogen torches or lasers may also be used. The heat softens the tip of the preform and a thin filament can be drawn off to form the fibre. The neck down process is entirely due to the influences of the surface tension and viscosity of the glass and the drawing tension. No dies or other mechanical forming mechanisms are used. The mechanism of fibre drawing has been shown to be one of quasi-one-dimensional extensional flow by Geyling and Homsey [59] who prepared preforms with a grid of coloured glass in a diametric plane. These were drawn and quenched to visualise the flow in the neck-down region. Paek and Runk [60] showed that the shape of the neck down region depended on the drawing rate and heat flux distribution in the furnace.

To optimise fibre performance it is usual to control the fibre diameter to a tolerance of around 1%, to achieve this a non-contacting fibre diameter monitor is placed below the furnace. This is connected to a microprocessor control circuit which can vary the temperature and draw tension accordingly.

To protect the pristine surface of the as-drawn fibres it is usual to coat the fibres with a sheath as part of the drawing process.

The fibre is finally wound onto a drum at the bottom of the drawing tower.

2.8 Overview of Electron Microscopy

2.8.1 Electron Beam/Specimen Interactions

Much of this section is covered in more detail in Goodhew [61].

When the electron beam interacts with the sample there are many possible outcomes. The incident electrons may pass straight through the sample or be deflected through large or small angles. The interactions may result in the emission of the same or different electrons or the emission of x-ray or visible photons. All these processes have differing probabilities of occurring which are usually described in terms of interaction cross sections.

The interaction cross section for a scattering mechanism is the area apparently presented by a substrate atom to the electron beam. It follows that the probability of an interaction of a given type within a layer of sample of thickness dx with N atoms per unit volume is $N\sigma dx$ where σ is the cross section.

Alternatively the interaction can be described in terms of a mean free path, ie the average distance an electron travels between each interaction of that type. In the case of a thin specimen as used in the TEM the mean free path is more than the specimen thickness and most electrons pass right through without interacting at all.

Elastic Scattering

Elastic scattering is due to the interaction of the electron beam with the Coulombic fields of the atoms in the specimen. In this process only the direction of the electron is changed, little or no energy is lost.

Elastic scattering is described by the Rutherford scattering model

$$Q(>\theta_0) = 1.62 \times 10^{-20} \frac{Z^2}{E^2} \cot^2 \left[\frac{\theta_0}{2} \right] \frac{\text{events}}{e^-(\text{atom}/\text{cm}^2)} \dots\dots\dots 2.16$$

where $Q(>\theta_0)$ is the interaction cross section for scattering into an angle greater than θ_0 , Z is the atomic number of the sample and E the electron energy (keV).

The above equation shows that the scattering cross section has a strong atomic number dependence, an important factor in TEM image formation. The equation also shows that scattering through small angles is more likely than through large ones, i.e. the elastically scattered electron distribution is heavily forward peaked.

Elastic scattering was an important factor in this investigation as it is the cause of beam spread and limits the resolution of x-ray analysis.

The beam-spread in a thin film based on a single Compton scattering event per electron is given by the Goldstein Equation [62]:-

$$b = K \frac{Z}{E_0} \left[\frac{\rho}{A} \right]^{1/2} t^{3/2} \text{ nanometres} \dots\dots\dots 2.17$$

where E_0 is the electron beam energy, ρ is the density of the sample in g/cm^3 and K is a constant:-

$$0.2 \text{ KeV.cm}^{-3/2} \cdot \text{nm}^{3/2} \cdot \text{g}^{-1/2}.$$

This expression is fairly accurate up to a specimen thickness of $2\mu\text{m}$ at a beam energy of 40keV [63] although above this thickness inelastic scattering must be taken into consideration. For fuller accuracy plural electron scattering should also be considered [62] but it was considered that, due to the wide variation in sample thicknesses, the above equation would be sufficiently accurate for this investigation.

Inelastic Scattering

In inelastic scattering the incident electron loses some or all of its energy. This energy can be dissipated in a number of ways:-

Primary Processes

i) Bremsstrahlung (Braking) Radiation

The Bremsstrahlung effect describes the emission of electromagnetic radiation by accelerated charged particles. As incident electrons interact with the specimen atoms they are accelerated and so emit x-rays. The energy of the emitted x-ray photon is a factor only of the geometry of the interaction and thus the Bremsstrahlung radiation contains no compositional information, quite the reverse in fact as the background radiation detected can hide the small peaks of elements present in low concentrations.

The intensity distribution of this background is given by

$$I_{\text{cm}} \propto Z(E_0 - E)/E \dots \dots 2.18$$

where I_{cm} is the intensity of the continuum at an energy E . E_0 correspond to the energy of the incident electrons and Z

is the average atomic number of the sample at the point where the beam impinges.

ii) Plasmon Scattering

Plasmons are waves in the conduction electrons in metals or the bonding electrons in non-metals. The incident electrons lose 5-30eV and the interaction cross section is large, making plasmon scattering one of the most important processes in electron/specimen interactions. Plasmon scattering, however, has no analytical value as the energy losses are not characteristic of any sample properties.

iii) Phonon Scattering

Electrons can excite phonons in the sample. These are quanta of vibrational energy in a solid. The incident electron beam loses about 1eV of energy in such a process and the effect is to heat the sample. The amount of energy transferred is not very large and the cross section is small, but all electrons that remain in the sample are likely to excite phonons eventually, probably after other interactions. The angle through which the electrons are deflected is also quite large, around 10° .

iv) Atomic Excitations

It is possible for the incident electron to excite an atom in the sample.

If the interaction is with an outer shell electron the energy loss and deflection are small. The cross section for this process is smaller than for either of the two processes outlined above and the effect is not of any use for

microscopy.

Another possibility, with an even smaller cross section is that the incident electron will ionise the sample atom by removing an inner shell electron. The amount of energy involved is large (hundreds to tens of thousands of electron volts). The cross section for this process falls with incident beam energy and also with atomic number, as the energy transfer required for the process rises with atomic number.

The importance of this process lies not in the process itself but in the secondary processes occurring when such excited atoms relax.

v) Characteristic X-rays

Excited atoms relax by outer shell electrons losing energy to occupy the vacant lower energy state. The energy lost is in the form of a photon, and in the case of a transfer to a K or L shell the energy involved is such to involve an x-ray photon. These x-ray photons have energies characteristic of the excited atom and are the basis of x-ray analysis which will be discussed in a later section.

If the ionised electron comes from one of the outer shells then the amount of energy is reduced, in which case the emitted photon will fall in the optical range. This is the basis of an analytical technique called cathodoluminescence.

vi) Electrons

The most important, from a microscopical viewpoint, of the classes of electrons emitted by substrate atoms are the

secondary electrons. This term describes all emitted electrons with relatively low kinetic energy (<50eV). These could be primary electrons which have suffered many scattering processes and have reached the surface with a few electron volts remaining but are more likely to be electrons from substrate atoms which have picked up some energy from the incident electron beam quite close to the sample surface. The ratio of emitted secondary electrons to incident electrons is high, as much as 1:1, and so secondary electrons are abundant and useful for imaging.

It is possible for a primary electron to be scattered through a large angle, either elastically or inelastically, and to re-emerge from the top surface of the material. The probability is high that such electrons will have a large part of their initial energy remaining.

The electron backscattering coefficient is a strong function of the atomic number. Goodhew [61] quotes Heinrich as giving the relationship as:-

$$\eta = -0.254 + 0.016 Z + 1.86 \times 10^{-4} Z^2 + 8.3 \times 10^{-7} Z^3$$

The backscattered electron intensity can therefore be used to detect changes in sample composition as long as such changes are accompanied by a corresponding change in average sample atomic number.

The interaction volumes for the main processes of interest are shown in Figure 8. It can be seen that for a bulk sample the interaction volume for backscattered electrons is smaller than that for X-rays, but for a thin film the resolutions are

very similar.

2.8.2 Specimen Coating

As the electrons impinge on the sample there is a tendency, if the sample is non-conducting, for a negative charge to build up on the sample. This leads either to deflection of the electron beam or to "flaring" of the image in the secondary electron imaging (SEI) mode where certain areas of the sample appear much brighter than others. To avoid this problem it is usual to coat non-conducting samples with a conducting layer. In SEI it is usual to coat the samples with gold or platinum as these have a high secondary electron coefficient. If absorption of electrons is a problem as is the case in TEM, or analysis is to be performed and the characteristic x-rays of the coating metal would be inconvenient it is usual to use a thin film of evaporated carbon from a carbon arc.

2.8.3 Imaging Modes in the TEM

2.8.3.1 Conventional Transmission Electron Microscopy

Conventional TEM (CTEM), in which the magnified image is viewed on a phosphorescent screen at the base of the microscope column is almost a direct analogy with light microscopy except that instead of the electrons being absorbed by the specimen, as is the case with light, they are scattered outside the field of capture of the objective lens. In conventional TEM the contrast of the image is varied by inserting apertures into the beam path in order to vary the effective field of capture.

As described above, the elastic scattering cross section

has a high atomic number dependence. In the case of an optical fibre the core region has a very different chemical composition to the rest of the fibre and it is generally possible to make use of this contrast to locate the cores prior to analysis.

Seward [14] showed that to achieve minimum detectable resolution on the photographic plate (5%) required a density variation of 0.1 g cm^{-3} for an object $0.1 \mu\text{m}$ thick.

In addition interference effects in the scattered electrons lead to phase contrast. For phase contrast to be detectable an internal potential variation of ≈ 1 volt is required. (The internal potential of silica is around 10 volts).

2.8.3.2 Scanning Transmission Electron Microscopy, STEM

If the electron beam is focused to a point on the surface of the sample and the intensity of the transmitted beam is measured by a detector then that intensity is a measure of the electron transparency of the sample at that point. This is the basis of the technique of Scanning Transmission Electron Microscopy.

To obtain an image from STEM the electron beam is moved across the surface of the sample in a raster scan. In synchronisation with this another electron beam in a cathode ray tube performs a raster scan of the phosphor screen of the tube. The intensity of the beam in the cathode ray tube is modulated by the intensity of the transmitted electron beam in the microscope column. This produces an image on the screen, the magnification of which is the difference in size between

the scanned area on the sample and that on the screen. This imaging technique is optically equivalent to CTEM, but as the image signal is electrical it lends itself to amplification and other forms of manipulation. STEM was used almost exclusively by this project as the same scanning mechanism was used to direct the electron beam during x-ray analysis, it was thus possible to analyse selected features seen on the STEM viewing screen.

The ultimate resolution of the STEM is governed by the size of the electron probe, a combination of the initial focused spot and the beam spread as the electrons travel through the specimen.

2.8.3.3. Scanning Electron Microscopy

This is the term used to describe an imaging technique using secondary electrons, although more rigorously it should be termed secondary electron imaging (SEI), to differentiate it from backscattered electron imaging, available in dedicated SEMs. The mechanism is exactly as described in the section above with the exception that the screen brightness is modulated by the intensity of secondary electrons emitted by the sample. This technique was also available on the microscope used in the investigation and was used at low magnifications to locate the fibre samples in the holder before switching to STEM.

2.9 X-Ray Analysis

As described earlier, when an excited atom relaxes it releases the excess energy in the form of a photon. If the energy difference between the vacant electron energy state and that from which the electron filling it originates is large enough, then the photon emitted is an x-ray. The energies of the electron states depend on the charge of the nucleus and the arrangement of the other electrons in the atom, so the energies of the emitted photons are characteristic of the emitting atoms. This allows for the determination of two sample characteristics. Firstly, the peaks in the x-ray spectrum enable the microscopist to identify the elements that are present and, secondly, the relative intensities of the peaks allow for the quantitative analysis of the proportions of each element present in the sample.

For the atom to emit an x-ray photon the vacant energy state must lie in the K bands for elements lithium to potassium, in the K or L bands for calcium to barium and in the K,L or M bands for elements lanthanum onwards. In this labelling convention the K shell refers to the two innermost electron energy levels, the L shell to the 8 energy levels outside this and the M shell to the 18 energy levels outside these. In the alternative, chemical, nomenclature the K electrons are known as the 1s, L electrons as 2s and 2p and the M electrons as the 3s,3p and 3d electrons.

It can be seen that as the number of electrons in the atom increase the number of possible electron transitions increases as well. In the case of Zinc, for instance, with thirty

electrons there are 900 combinations. Fortunately for x-ray analysis only a few of these transitions are possible, and of these few even fewer have a large enough energy difference to emit x-rays. Zinc for instance has only 5 detectable x-ray peaks.

2.9.1 Energy Dispersive X-Ray Analysis

When an x-ray photon enters a semiconductor such as silicon it creates electron-hole pairs. As the potential energy of each pair is 3.8eV and the energy of the x-ray photon is in the order of several keV a large number of such pairs are created. The precise number of pairs is a measure of the incident photon energy to quite a high resolution. If a voltage is applied across the silicon then the electron-hole pairs will allow a current to flow, the magnitude of the current being proportional to the number of pairs created and hence also proportional to the incident photon energy.

In practice the resistivity of pure silicon is too low, and the current flow induced by the electron-hole pairs is masked by the much higher steady state current. To avoid this problem the x-ray detector is made as a p-i-n diode, reverse biased with the active detector of the i region sandwiched between the much thinner p and n regions. The silicon is cooled to 77K (liquid nitrogen) to further decrease the conductivity. The cooling also decreases any noise due to thermal effects and prevents diffusion of the lithium dopant used to generate the diode structure. The voltage is applied through a coating of gold on the front and back surfaces of the detector. The

coating on the front surface is made as thin as possible to minimise x-ray absorption. The detector is protected behind a beryllium window to prevent contamination of the detector or degradation of detector vacuum. This window has the undesirable effect of blocking the low energy electrons from light elements, and if one is fitted, as was the case for the detector used in this project, it is impossible to detect the presence of elements lighter than sodium. The window does, however, have the advantage of preventing secondary electrons entering the detector. Figure 9 shows the arrangement of a typical solid state detector.

There is presently a trend towards windowless detectors or detectors with an ultra-thin Mylar window. These both allow analysis of lighter elements up to boron. The ultra thin window retains the ability to stop electrons but is not strong enough to withstand a pressure differential between the column and the detector. Such installations therefore require a shutter arrangement to maintain detector vacuum if the microscope column is vented to air.

The current flow is transient, lasting less than a microsecond and is usually referred to as a pulse, these pulses are amplified by an FET transistor mounted close to the detector and also cooled to reduce electrical noise and then transmitted, via a pulse processing unit, to a multi-channel analyser (MCA). This MCA increments the value of the channel corresponding to the particular x-ray energy and hence over a period of time a histogram of the emitted x-ray spectrum is

built up.

The x-ray photons are actually detected as a series of increments in the voltage across the FET rather than as pulses and so it is necessary to periodically reset the FET by flooding it with photons from an LED. Whilst this is occurring the detector cannot detect incoming photons. This period is referred to as the dead time. At high count rates the frequency at which the FET is reset is correspondingly higher and so therefore is the dead-time. At very high dead-times the energy resolution of the detector is degraded, and so there is a maximum useful count rate with the solid state energy dispersive detector.

The advantages of this system are that it is very easy to collect a spectrum and qualitatively analyse it. This is further facilitated by the software generally included in the analyser package.

The disadvantages of the technique are that the energy resolution is fairly poor. The best modern detectors have an energy resolution of 130eV, the one used on the JEOL 100CX had a resolution of 152eV when new. Therefore it is sometimes hard to distinguish closely spaced peaks. A side effect of this peak width problem is that the height of the resulting peak is reduced. A narrow analysis window thus contains fewer of the characteristic x-rays, whereas a wider one will include more background counts. This peak spreading therefore reduces the signal to noise ratio and so may make it difficult to resolve elements with low abundances.

Also with this type of detector a number of spurious events

may be detected. These artefacts include the following.

1) Silicon escape peaks. An incoming x-ray can ionise a silicon atom by removing a K shell electron and hence lose 1.74keV. The reduced energy photon thus appears in a false peak 1.74keV further down the spectrum unless the resulting Silicon $K\alpha$ peak is rapidly processed by the detector and analysed as the same event.

2) Silicon fluorescence peak. If the $SiK\alpha$ photon mentioned above is not given out immediately then it can appear as a spurious silicon event on the spectrum.

3) Sum peaks. These are caused when two photons enter the detector at the same time and are thus analysed as one event with the sum of their energies.

Problems also arise from the scattering of electrons into the detector. The effects of this can range from spurious silicon x-ray detection through to the detector ceasing to work for several hours. The cause of this freezing is not fully understood.[64]

2.9.2 Wavelength Dispersive Spectrometry

An alternative technique exists for the measurement of x-ray energy. This is called wavelength dispersive spectrometry (WDS), to distinguish it from the above technique which is called energy dispersive spectrometry (EDS). This is purely a naming convention to distinguish between the two methods, energy and wavelength are, of course, equivalent.

In the WDS method the emitted photons are diffracted through a crystal. Different wavelengths are diffracted

through different angles and the wavelength is selected by varying the position of a slit. The selected x-rays are then detected by a gas proportional counter. This kind of counter is used because it can cope with much higher count rates than a silicon detector and is not required to analyse the photon energy.

The disadvantages of the crystal spectrometer are that it is difficult to use; being a serial device it can only look at one energy at a time so collecting a full spectrum is time consuming. This problem is alleviated to some extent by the relatively high count rate available from the counter.

The collection angle of the WDS system is very small, far less than that of an EDS system in which the detector can be placed very near to the specimen. This, coupled with the fact that most photons are selected out and not detected, reduces the count rate enormously, increasing the time required to collect data even at a single energy.

It is very important that the analysed area of the sample, the crystal and the detector are kept in precisely the correct geometry; this necessitates a time-consuming alignment procedure for the sample prior to analysis.

The advantages of the system, however, sometimes outweigh these disadvantages.

The main advantage is the increased spectral resolution of the WDS system and the commensurately increased peak to background ratio. The peak width, and hence detection limit of the WDS system is almost two orders of magnitude better than

that of the EDS system so that peak overlaps are rarely a problem.

The WDS detector is also far more sensitive to light elements and can detect x-rays as soft as Beryllium, atomic number 4.

2.9.3 Quantitative Analysis

In principle it should be quite straightforward to move from the identification of the elements present in a sample to the determination of their relative abundances. In practice it is not quite that simple as different elements have different cross sections and hence x-ray yields for a given number of incident electrons. This is quite easily allowed for by measuring the x-ray yield with a sample of known composition and comparing that with the x-ray yield for the unknown sample under precisely the same analysis conditions. The concentration of the element in the sample is then given by;

$$C_{\text{spec}} = (N_{\text{spec}}/N_{\text{std}}) \times C_{\text{std}} = k \times C_{\text{std}} \dots \dots \dots 2.19$$

In bulk samples the situation is further complicated by three factors: Atomic number effects vary the distance into the sample that the electrons penetrate and also the number of interactions each electron initiates before losing too much energy to generate x-rays. X-ray absorption effects reduce the number of x-ray photons emitted relative to those which are generated. Fluorescence effects lead to the enhancement of some peaks at the expense of others. These are corrected for by the ZAF procedure in which the concentration of the element in the

sample is given by

$$C_{\text{spec}} = k \times Z \times A \times F \dots\dots\dots 2.20$$

where Z, A and F refer to the corrections for each of the important factors. There is a strong interdependence between these effects and so the values of Z, A and F are normally arrived at iteratively from semi-arbitrary initial values.

Matters are much simplified in the case of thin film samples as the sample thickness is less than the mean free path for most of these processes. As the project under consideration here was concerned almost entirely with thin samples the ZAF correction will not be described in any more detail.

For samples thin enough to ignore these effects;

$$\frac{C_a}{C_b} \cdot \frac{N_a}{N_b} = k_{ab} \dots\dots\dots 2.21$$

where N_a and N_b are the measured characteristic x-ray intensities and C_a and C_b are the weight fractions of any two elements in the sample. k_{ab} is dependent on many factors and it is usual to determine it experimentally. To avoid the necessity of determining the correlation constant for every pair of elements it is possible to determine it from the ratios of two values from a common element, ie $k_{ac} = k_{ab}/k_{bc}$. Usually the common element is silicon and the standards are minerals or alloys of known composition.

The thickness of specimen for which the above approximation is valid depends on the nature of the sample, but is normally 50-100nm. In the case of thicker samples it

may be necessary to use an absorption correction.

2.9.4 Detection Limits

Because the spectrum is built up from a large number of discrete measurements it is governed by the Poisson distribution. This means that the uncertainty in the number of events detected is equal to the square root of that number. Figure 10 shows a section of an hypothetical spectrum. N_p is the number of counts detected in a window of width W_p centred on the peak and N_b is the number of counts detected in a window of width W_b adjacent to the peak to measure the background radiation. Alternatively the analysis program on the analyser will perform a linear interpolation between the two edges of the window and use this in a background subtraction. In this case the Gross Integral refers to the total counts in the window and the Net Integral to the number of counts above the interpolated line. In this case N_p is the net integral and N_b is the difference between the net and gross integrals. This automatic background subtraction routine was not available for processing of the ratemeter output and so for the linescans background subtraction had to be performed using the adjacent window technique.

In the case where background subtraction is performed using an adjacent window the number of characteristic counts in the peak window is thus given by :-

$$P = N_p - \frac{W_p N_b}{W_b}$$

and the standard deviation in this measurement σ is given

by [64]:-

$$\sigma = \left| N_p + \left[\frac{W_p}{W_b} \right] 2N_b \right|^{1/2} \dots\dots (2.22)$$

It is generally accepted that a peak is visible if it is more than three standard deviations above the background, ie if $P > 3\sigma$.

From the above expression it can be seen that the higher the total number of counts, the lower the detection limit. The only practical way to increase the number of counts is to increase the counting time as there is a maximum count rate at which a detector can operate. Exceeding this limit degrades the resolution and broadens the peaks (Section 2.9.1)

The maximum practicable counting time is in the region of 1000 seconds as after this time beam instabilities and sample drift become a problem [61]. Another problem with protracted counting periods is the peaks of the more abundant elements going off scale which entails the loss of 65535 counts from one of the peaks. For such an analysing period Goodhew [61] quotes 0.1% as a typical detection limit for the EDS system, with the WDS system being an order of magnitude better as the WDS detector can work at higher count rates.

2.10 Ion Beam Thinning

Ion beam thinning was an important part of the experimental procedure and the mechanics of the process were important in shaping many aspects of the sample preparation technique.

The process by which ion beam thinning occurs is atomic sputtering. Ions with energies in the 3-6 keV region only

penetrate a few nanometers into the sample and the deposition of their energy leads to the ejection of sample atoms from the surface.

The rate at which the sample is eroded is dependent on a number of factors.

1) Angle of incidence of the atoms. The sputtering rate has a maximum between ten and thirty degrees.[65] It falls off rapidly to zero at small glancing angles where the bombarding atoms are reflected and reduces more slowly to a minimum value at normal incidence. In commercial ion beam thinners the beam-specimen angle can be varied, in the case of that used in this investigation it could be varied between 0-90°. However at angles below 8° the path from the gun to the sample became occluded by the specimen holder.

2) Incident beam energy. The sputtering yield (number of atoms displaced per incident ion) increases with beam energy up to about 10kV. At this point the effect of the increased energy is manifest by deeper beam penetration. This leads both to an increase in damage depth and a decrease in sputtering yield as the energy is deposited too far from the surface for atoms to be ejected.

3) Relative masses of the target and sputtering atoms. The sputtering rate is higher for more massive incident ions. The incident ion must also be unreactive and available as an atomic gas, criteria best fulfilled by the noble gases. Argon is generally used as it is the heaviest of the noble gases available at a reasonable price. In some situations it is advantageous to use a reactive ion and in these cases Iodine

is used.

4) The sputtering yield varies with the composition of the sample. There is a variation of two orders of magnitude for the elements alone and the sputtering rates of compounds differ from those of their constituents. Kanaya [66] gives the following expression for the maximum sputtering yield for the elements

$$S_{\max} = 6.5 \times 10^{-11} N \pi a^2 / \epsilon_t \dots \dots \dots 2.23$$

where N is the number of atoms per unit volume, ϵ_t is an energy term proportional to the sublimation energy of the element and a is the screened radius of the atom given by

$$a = 0.8853 a_H (Z_1^{2/3} + Z_2^{2/3})^{-1/2}$$

where a_H is the Bohr radius of hydrogen and Z_1 and Z_2 are the masses of the projectile and target respectively. This function has a low value for tantalum and hence tantalum is generally used for the sample holders in ion beam thinners

This dependence of the sputtering rate on the composition of the sample can cause problems in samples in which the composition is not constant, such as those containing different phases or having inclusions. The process attacks some phases or crystallographic orientations preferentially and produces surface relief and thickness variations. These problems can be alleviated to some extent by rotating the sample and using the smallest possible beam angle [67]. This has the effect of constantly changing the beam direction and so, on average, the areas which have been preferentially eroded will be protected by those which have not.

Even in homogeneous samples the ion beam can create a surface structure consisting of ripples and indentations. The best way to reduce this effect is to reduce the amount of ion beam thinning performed on the sample by preparing the thinnest possible samples by mechanical means. As ion-beam thinning is a very slow process (less than 1 micron per hour) this also leads to a considerable time saving.

Another possible artefact of the thinning process is bubbles of gaseous argon formed in the sample [65], these are only formed at high beam energies and so are easily avoided.

At high beam energies or currents specimen heating may also prove a problem. Barker [67] measured the temperature rise in a glass sample as 127°C. This is not a problem for most samples but is sufficient to melt epoxy resins such as the Araldite used to mount the samples in this investigation. This effect can be reduced by reducing the beam current, at the expense of an increased thinning time.

Chapter 3 Experimental Procedure

In this section the reasons for the development of the experimental technique will be described. The major part of the project was concerned with developing a specimen preparation technique and the various stages of this development will be enucleated in detail.

The acquisition of experimental data required both the modification of existing equipment and the development of new equipment and procedures; these will also be described.

3 Experimental Procedure

As previously stated, the aim of the project was to determine the elemental distributions in the cores of optical fibres by use of electron probe x-ray analysis.

The cores of the optical fibres under investigation varied between $2\mu\text{m}$ and $25\mu\text{m}$. The analytical resolution of x-ray analysis in a bulk sample is around 2 microns, barely adequate for the largest cores, and far too low for the smaller ones.

There are two ways of improving the resolution of such an analytical technique, by either reducing the electron energy or the specimen thickness. The first of these techniques will improve the resolution slightly at the expense of x-ray counts, and hence reduces the signal/noise ratio and elemental detection limits.

The second technique, reduction of the sample thickness also reduces the count-rate, but for a much larger increase in spatial resolution.

The beam-spread in a thin film is given by the Goldstein Equation [62]:-

$$b = K \frac{Z}{E_0} \left[\frac{\rho}{A} \right]^{1/2} t^{3/2} \text{ nm} \dots\dots(2.17)$$

where E_0 is the electron beam energy, ρ is the density of the sample in g/cm^3 and K is a constant given by

$$K=0.2 \text{ KeV.cm}^{-3/2}.\text{nm}^{3/2}.\text{g}^{-1/2}.$$

This beam spread is plotted as a function of sample thickness for a silica sample in figure 12. As can be seen from the graph, a very worthwhile increase in resolution can be expected from the use of a thin film in place of the bulk sample. The equation also shows that the resolution increases with increasing beam energy, the reverse of the case with a bulk sample.

In the case of the fibre samples a typical thickness measured by the contamination spot method [68] would be 400 nm, leading to a beam spread of approximately 100 nm. With a typical 40 nm spot size the expected resolution would be in the region of 100nm, an order of magnitude better than with a bulk sample.

TEM, therefore, will give an increase in analytical resolution sufficient to make up for the increased difficulty in sample preparation.

3.1 Sample Preparation

The first stage of the project was therefore to develop a technique for the production of thin sections of optical fibres. With a typical fibre diameter of $100\mu\text{m}$ this effectively required the fabrication of glass cylinders $100\mu\text{m}$

in diameter and 200nm thick.

As the development of this experimental technique constituted an unusually large proportion of the whole project, its derivation will be described in detail.

An examination of the literature failed to find any reference to the preparation of optical fibres for TEM. Papers were, however, consulted on the preparation of carbon fibres for TEM. These relied on setting the fibres in epoxy resin and then sectioning by ultramicrotomy [69] or machining and sectioning followed by ion beam thinning [70]. It was considered unlikely that an ultramicrotome would successfully section glass fibres without them shattering; such problems were encountered even with the much smaller, less brittle carbon fibres. The latter technique relied on the use of a diamond wheel to section the fibre/resin composite into 100 μ m discs. As no such diamond wheel was available it was decided to combine the technique of mounting the fibres in a resin matrix with a technique used by an earlier investigator [71] for the preparation of samples of bulk glass.

3.1.1 Initial Technique

A length of fibre was stripped of its polymer sheath using varnish remover. This fibre was then cut into sections approximately 30mm long, packed tightly in a length of brass tube 3mm in diameter and vacuum impregnated with Araldite CY1303 low viscosity epoxy resin. The tube was then sectioned into 1mm thick slices and the slices were ground down to approximately 200 μ m thick. A number of the discs so formed

were attached to a square glass slide with beeswax and ground down as thinly as possible on a Kent polishing wheel with a 6 μ m ceramic pad. This polishing technique had been used by other researchers for bulk glass samples using dental wax. In the case of these composite samples the lower melting point of beeswax was advantageous as the samples would buckle and break at temperatures above 100°C.

A number of discs were thinned simultaneously in an attempt to keep them parallel.

The discs so formed were melted free of the slide, cleaned in alcohol and then ion beam thinned until a hole appeared in the middle, whereupon they were examined under the microscope.

3.1.2 Development of the Experimental Technique

This initial technique had a number of inadequacies, these are described below and the steps taken to eliminate them explained.

1) Excessive fibre usage. With the initial technique it was necessary to strip and cut into short lengths up to five metres of fibre. As this was done by hand with a scalpel it was a very tedious process. It was also wasteful of fibre as only a few of the 200 or so fibre lengths were electron transparent, the rest of the fibres only filled up the space between these and the brass tube.

The samples were also very fragile and prone to incomplete permeation of the resin, so that holes would frequently appear between fibres during the polishing process or whole fibre sections fall out. It is undesirable for samples undergoing

ion beam thinning to have holes in them as there is a tendency for the thinning process to preferentially attack the edges and so reduce the size of the thinned area.

These problems were overcome by using a tube with a far smaller hole in the centre. The original brass tube had a hole 2.5 mm in diameter, this was reduced to 0.38mm in the later technique, leading to both a reduction in total fibre usage to around 200mm and an increase in sample strength. It was also a far more straightforward process to set the fibres in the tube as all that was necessary was to dip the fibres in the epoxy resin and then place them in the tube with tweezers. The diameter of the hole was chosen such that seven fibres of average diameter could be packed in neatly to leave a minimum of the less ion beam resistant resin exposed to the ion beam.

2) Control of the polishing process was hard to achieve. The samples would tear, fall off or polish away entirely on one edge before being thin enough to ion beam machine within a reasonable time.

The root of this problem was the attempt to get the whole sample, fibres, brass and araldite to a sufficiently small thickness to ion beam thin. The solution was to thin the whole sample to around 75 μ m and then thin only the central area to 15 μ m with a dimple grinder. This machine uses a 15mm diameter diamond wheel to grind away the sample which is held on a rotating stub. The machine is graduated in microns and it would seem to give reproducible results at this scale.

The samples were still too delicate to grind down to 75 μ m

unsupported in a grinding block. One solution would have been to leave the samples thicker and grind a deeper dimple, but it was found that, at the low angles required to get suitably smooth samples, the ion beam could not reach the bottom of such a deep dimple. To circumvent this problem another grinding block was made with a hole large enough to take a dimple grinding stub. The samples were thinned to $200\mu\text{m}$, attached to the dimpling stub and then further thinned to $75\mu\text{m}$ using this block.

3) The samples when formed were very sensitive to heating, tending to buckle when being melted free of the slide. They also tended to absorb alcohol when being cleaned, which caused swelling and buckling.

The switch to thicker, stronger samples solved these problems to some extent but alcohol still had a deleterious effect on the epoxy, as did heating.

To avoid using alcohol, and to reduce the amount of heating required, a low melting point wax soluble in turpentine was obtained. This wax was stronger than the beeswax used in the earlier attempt to limit sample heating but had a similar melting point of 70°C . Turpentine was found to have no effect on the araldite. This, coupled with the increased strength of the samples, meant that samples could now be cleaned with a turpentine soaked cotton bud. As specimen cleanliness is a great aid to even ion beam thinning this was a useful step in itself.

The move to dimple grinding, however, brought with it its own problem. The dimpling stubs supplied were glass or

stainless steel rods 3/8" long and 3/8" in diameter. These took a long time to cool down when the sample was affixed to the stub and, more importantly, took a long time to heat up when the dimpled (and therefore more heat sensitive) sample was removed. This subjected the sample to excessive heat which was found to weaken the Araldite and in some cases led to fibres dropping out.

To circumvent this problem the special dimpling stub shown in figure 13 was made. It has a small detachable top section, with a much reduced thermal mass. This shortens the time taken for the wax to melt from around thirty seconds with the original stubs to around 3 seconds.

4) The ion beam thinning process tended to sputter the resin preferentially to the fibres. This caused the fibre pieces to fall out before reaching electron transparency.

In one of the carbon fibre preparation references [70] Goodhew suggests mixing carbon black with the epoxy resin to reduce its sputtering rate. It was decided to try this and some carbon black was obtained from a plastics filler supplier. Also supplied was some titanium dioxide powder specially treated to mix readily with polymers, a common filler and colouring agent in commercial plastics.

Both of these materials were tried as additives to the specimen setting resin. It was found that a larger proportion of titanium dioxide than carbon black could be mixed in with the resin, that titanium dioxide increased the viscosity of the resin less than the carbon and that it was easier to mix.

The titanium dioxide was also found to be the more effective in reducing the sputtering rate and was cleaner to use. The only potential problem with the titanium dioxide was contamination of the sample and hence the production of spurious x-rays. This would not be a problem with the carbon as carbon x-rays are too soft to be detected with a solid state detector. In practice no titanium peaks were ever detected. Because of these advantages titanium dioxide was used exclusively throughout the remainder of the project.

5) There was no adequate way to determine the thickness of the samples, mainly due to sample fragility. This made it difficult to estimate the required ion beam thinning time.

With the stronger samples made using the sample holder tubes with the reduced hole size it became possible to use a dial indicator. This was, however, occasionally inaccurate and a more reliable thickness measurement was eventually achieved using a digital micrometer. This was graduated in microns and achieved excellent repeatability.

These modifications eventually led to the evolution of a refined technique with a much increased reliability.

Eventually the only unreliable part of the process was ion beam thinning, largely due to an unreliable ion beam thinner.

3.1.3 Final Technique

1) A 0.38mm hole was drilled down the centre of a piece of 3mm brass rod 2.5 cm long. The length of the rod was governed by the length of the drills available in this diameter.

Temaxol cutting compound was found invaluable as without it the

drills would friction weld themselves to the brass rod and break. It was also necessary to frequently lift the drill from the hole to clear swarf as the flutes of the drill were only 4mm long. To facilitate the repeated re-entry of the drill into the hole the tops of the brass rods were countersunk. This also held a useful pool of resin during fibre insertion.

2) The Araldite was mixed with 50% by weight Titanium Dioxide powder. This proportion was found to give the right balance between increased resin viscosity and reduced sputtering rate.

3) The tube was cut into 1mm discs with a Silicon Carbide saw and the disc ground down to 200-300 μ m thickness using a roughing block, (Figure 14) and 600 grade silicon carbide paper. This disc was polished on one side to a 1 μ m diamond finish. It was found that a good sample finish before ion beam thinning improved the constancy of sample thickness after thinning.

4) The thickness of this sample was then measured with a digital micrometer and fastened, polished side down, to a specially made grinding stub using a low melting point wax.

5) The grinding stub was reassembled and the total thickness of stub, wax and sample measured. This enabled the specimen thickness to be calculated without removing it from the stub and took into account the variable wax thickness from sample to sample.

The grinding stub was then placed in a holder similar to the roughing block in Figure 14 (but with a larger bore) and

the sample ground to a thickness of $75\mu\text{m}$. The fact that the sample was attached to the grinding stub provided sufficient support to allow this grinding to be done on 600 grade Silicon Carbide paper. The disc was then polished, labelled (using a sharp scribe and a binocular microscope) and remeasured.

6) The area of the sample containing the fibres was ground to a thickness of $15\mu\text{m}$ using a Gatan Dimple Grinder into which the grinding stub fitted directly. This process produced a relatively sturdy sample $75\mu\text{m}$ thick with a thin area in the middle, facilitating specimen handling and ensuring that the correct area of the sample was ion beam thinned. The combination of relatively rugged sample and turpentine-soluble wax meant that the sample could be cleaned with a turpentine soaked cotton bud.

7) The sample was thinned for around 17 hours at a beam angle of 8.5° and a specimen current of $25\mu\text{A}$ at 5kV.

The precise duration of the ion beam thinning process varied with a number of factors, many of them unpredictable. The main problem was caused by the ion beam thinner cutting out at some unknown time during an overnight run. In this situation it was hard to judge how much more thinning was required.

The speed of the thinning process was also dependent on the state of wear of the cathodes, small holes in the cathodes resulted in much higher thinning rates, better vacuum and a greater tendency to trip the cut-out. Larger holes led to a much slower thinning rate and in extremis the rate of

metal deposition from other parts of the thinner seemed to exceed the sample sputtering rate. With larger holes in the cathode, however, the thinning process was much more stable.

Towards the end of this investigation the problem of the ion beam thinner cutting out was traced to tracking across the gun insulators. New insulators were made and were found to cure the problem but to need replacing approximately monthly.

It was found that carbon coating before microscopy was not necessary due to the thinness of the samples and the close proximity of the fibre sections to the brass holder.

The sample preparation procedure is shown in diagrammatic form in figure 15.

3.1.4 Preparation of Bulk Samples of Preform.

In addition to the main work an investigation was carried out to investigate whether the concentration profile of germanium changed at any stage during the fibre drawing process. To this end the short length of preform left after the drawing of one of the Erbium Doped fibres was obtained. This section tapered in diameter from 13mm to 200 μ m. In addition a sample of the corresponding fibre was also obtained.

This preform section was cut into slices using a diamond wire saw and polished.

The preform sections were large enough for the analytical resolution of SEM with bulk samples to be adequate, so there was no need for the samples to be thinned.

As the larger sections of the preform were too large to fit

into the TEM bulk specimen holder it was necessary to remove the core region of each section using a diamond core drill.

The diameter of the preform section, from which each core was taken, was measured with a digital micrometer for later normalisation.

3.2 Examination of Samples

Fibre examination in the electron microscope consisted of two aspects, imaging and analysis. Of the two, analysis was by far the more important, imaging being of use only to find the fibre cores and to measure sample thickness.

The instrument used for the project was a JEOL 100CX; a 100KeV Transmission Electron Microscope fitted with a scanning facility which allowed use of Scanning Transmission Electron Microscopy (STEM) and Secondary Electron Microscopy (SEM).

For analysis the microscope was fitted with an "EDAX" x-ray detector connected to a Link Systems multi-channel analyser and processor. Also added during the course of the investigation were a Scan Rotate module and an analogue-digital converter linking the processor to a microcomputer.

3.2.1 Concentration Profile Acquisition

Before a concentration profile could be acquired of a fibre core it was first necessary to locate the core in the fibre sample. This was often fairly difficult as the cores were very low contrast objects easily obscured by thickness variations or other artefacts. Cores were located visually by the use of STEM. In this situation the facility with STEM to alter the

contrast and brightness of the image gave the technique a marked advantage over conventional TEM. In some cases the cores had to be located by the use of x-ray mapping using the Digimap utility on the analyser. This utility produces a false colour image of the field of view of the microscope, the intensity of the colour being proportional to the x-ray intensity of the chosen window at that point.

Once the core was located the analyser was activated and a spectrum was acquired. The peaks were identified and windows drawn for those of interest. The analyser was fitted with a digital ratemeter which measured the x-ray intensity in a selected window. Initially the ratemeter output was recorded on photographic film as a linescan superimposed on a micrograph of the core being examined. This proved inadequate in situations where more than one element had to be quantified as all the linescans were white. The linescans produced in this way were also of limited usefulness as they had no axes and the baseline varied from one scan to another. It was decided that if the data could be transferred to a computer rather than to a photograph it would be much easier to correlate and manipulate.

The x-ray analyser had a utility in the "Digimap" program to create a linescan from a Digimap image, but this had a resolution of only 128x128. To acquire such a linescan required the acquisition of a digimap, to get the equivalent of a 500 second linescan would therefore take 500 times 128 seconds, about 17 hours!

It was discovered that the ratemeter output was transferred

to the microscope via a connector at the back of the analyser as an analogue voltage between 0 and 2.5 volts. It was decided, therefore to divert this output to a microcomputer and store it on disc for later analysis.

To enable this voltage to be recorded by the microcomputer (an Opus PCIII) it was necessary to convert it to digital form. In order to achieve this the author built an Analogue to Digital converter circuit based around a TLC548 8 bit A/D converter chip. For ease of connection to the computer (then in another room) it was decided to use the RS232 serial format. The chip used in the circuit was found to output the data in a Most Significant Bit First format, the reverse of the RS232 convention and a section of code had to be inserted into the data receiving program to carry out a bit-reversal. The converter, being 8-bit, converted the analogue values into numerical values between 0 and 255 at a sampling rate of four per second. Each value recorded by the computer program on the disc was an average of four of these readings taken with the microscope linescan on the slowest, 500 second, scan. The effective data resolution with this method was, therefore, 500x1024.

The data was received, recorded, analysed and plotted by specially written software. The programs and a circuit diagram for the Analogue/Digital converter are included in appendices 1,2 and 3 respectively.

A scan rotate module was fitted to the microscope for reasons explained in the discussion sections. The effect was

to remove a limit on analytical resolution and also to increase the consistency of the linescan magnifications.

3.3 Evaluation of the Experimental Technique

To evaluate the experimental technique it was necessary to measure both the electron beam spot size and the specimen thickness. In order to perform these measurements accurately and to ensure the accuracy of later results it was necessary to calibrate the microscope magnification.

3.3.1 Calibration of Microscope Magnifications

As some of the experimental data for the project were measured from micrographs it was important to find how accurate the magnification printed on the micrograph by the microscope was. For the preform-draw down data it was also very important to discover how self-consistent the magnifications were on a magnification range of 100x to 10,000x.

To facilitate these measurements a cross grating sample supplied by Poloran was used. This was a carbon replica taken from an accurately scored grating with 2160 lines/mm, or a line spacing of 463nm. This spacing was ideal for calibrating the 10,000x magnification but of less use at lower magnifications of interest, 100, 200 and 300x, as the grating was not resolved at these magnifications. To circumvent this problem a micrograph was taken in which both the grating and a whole sample grid hole could be seen. This procedure allowed an accurate measure of the grid hole diameter and thus these holes could be used for calibration of

the lower magnifications.

It was found that at magnifications of 200x and 300x the size and orientation of the image on the screen varied extensively with focus. The difference between the size of the image at maximum defocus on both sides differed by a factor of about eight. In principle, if the sample surface is at the Eucentric point (the centre of rotation of the sample holder) then the focus setting, and hence the magnification, should be the same for all samples. Nevertheless some doubt must remain about the reliability of the stated magnifications in this range. At 100x magnification and below the focusing is by a different mechanism and so does not alter the image size.

3.3.2 Determination of Effective Spot Size

The spot size was measured by depositing a carbon film onto a glass slide previously coated in soap. Onto this carbon film a platinum film was shadowed through some copper sample grids. The deposited films were then scored into 3mm squares and the slides soaked in water to allow the squares to float off

The carbon squares with platinised sections were then picked up on copper sample grids and analysed in the microscope.

The aim of the foregoing procedure was to produce a series of sharp concentration edges over which the electron beam could be scanned, the distance the electron beam scans between maximum and minimum platinum x-ray counts being taken as a measure of the beam diameter.

3.3.3 Determination of Specimen Thickness

The thickness of a number of samples was determined by the contamination spot method [68].

In the electron microscope the electron beam causes localised heating of the sample and, if preventative measures are not taken, this leads to cracking of backstreamed diffusion pump oil and the deposition of carbon on the top and bottom surfaces of the sample. If the beam is kept stationary in one place for long enough, two cones of carbon are built up on the sample surfaces. If the sample is then tilted these two spots can be seen to separate. The distance between the two spots on the viewing screen is:-

$$d = M t \sin\phi \dots\dots(3.2)$$

where d is the separation, M is the magnification, t is the sample thickness and ϕ is the tilt angle.

Specimen contamination is normally prevented by the use of a liquid nitrogen cold trap so under standard analysis conditions specimen thickness measurement was not possible. For this reason the thicknesses of only a few samples were measured.

3.3.4 Determination of Effectiveness of Scan Rotate Module

To find out to what extent the scan rotate module had fulfilled expectations in respect to improved analytical spatial resolution, two linescans of the same fibre core were acquired at 90° and 0° to the original scan direction.

Chapter 4

Experimental Results

4.1 Evaluation of the Experimental Technique

4.1.1 Calibration of Microscope Magnification

Figure 16 is a micrograph of a grid hole in a calibration sample consisting of a carbon replica of a cross grating scored at 2160 lines/mm. The spacing between each line is therefore 463nm. There are 162 lines across a diameter parallel to one of the grating directions, hence the grid hole is 75 μ m in diameter.

Figure 17 is a micrograph of the calibration specimen at a magnification of 10,000x. In order to have a meaningful comparison of the microscope magnifications it is necessary to decide what size the micrographs should be enlarged to during printing. These micrographs have been printed so that they are 108mm long. The grating on these micrographs is at an angle of 45° to the micrograph horizontal, which is the direction in which it is important that the scan be calibrated. It is thus necessary to work in square diagonals, which are 463 $\sqrt{2}$ long. In the figure there are 15 square diagonals in a distance of 98mm, which equates to a magnification of 9979x. This is within 0.2% of the notional magnification, which is adequate for this investigation. Calculating the magnification in the vertical plane gives a value of 8800x, a sign of serious image distortion.

Figure 18 is a micrograph of the calibration specimen at the smallest magnification of interest, 100x. The average diameter of each grid hole measured along the micrograph

horizontal (which corresponds to the linescan direction) is 6.0mm, which equates to a magnification of $6.0\text{mm}/75\mu\text{m} = 80\text{x}$

Figure 19 shows the same sample holes at 200x magnification. In this case the average hole size is 15mm on the micrograph, an effective magnification of exactly 200x.

Figure 20 is the same sample area at 300x magnification, the holes are now 22mm in diameter, which is an effective magnification of 293x

4.1.2 Determination of Effective Electron Probe Size

Figure 21 is an X-ray linescan of a platinised carbon film as described in section 3.3.1. The spatial extent of the edge is 35nm.

Figure 22 is a micrograph of the area of the sample where the linescan shown in figure 21 was performed. (Magnification 150,000x, imaging mode STEM)

Figure 23 shows a pair of contamination spots on a sample of fibre type 9695.01.01 at a tilt angle of 20° and a magnification of 100,000x (imaging mode STEM). The spots were formed in the manner described in section 3.3.2 and [68].

The contamination spots are separated by a distance of 30mm with the sample tilted at 30° . The magnification is 100,000x. If this magnification is assumed to be as accurate as 10,000x then from equation (3.2)

$$t = d/(m \sin \phi)$$

where in this case:-

$$t = 30 \times 10^{-3} / (100,000 \sin 20^\circ) = 900\text{nm}$$

Figure 24 shows a similar pair of spots on a sample of

5111.01 fibre at a magnification of 200,000 and a tilt of 30°. In this case the separation is 40mm, giving a sample thickness of:-

$$t = 40 \times 10^{-3} / (200,000 \sin 30^\circ) = 400 \text{nm}$$

4.1.3 Limits of Detectability

Table 1 lists the calculated minimum detectable concentrations for the main elements analysed for during the course of this investigation. The data are calculated from the actual analyses of a number of fibres and are based on a 500 second analysis period.

Table 2 lists the minimum time required for the peaks of each of the main elements found in the fibres analysed to rise to a height three standard deviations above the background. Silicon has been neglected in the majority of the results as its ubiquitous presence was of little interest with respect to the investigation.

These times are calculated from actual data and are based on the highest concentration of that element found in any of the fibres.

4.1.4 Effects Due to Scan Direction

Figure 26 shows two linescans performed on the same fibre core under identical conditions but in orthogonal directions in order to demonstrate the effect of the scan rotate module.

In the case of the unrotated scan the edge width is 20% of the total core diameter. In the one rotated through 90° in order to bring the scan parallel with the tilt angle it is 7%

of the diameter.

4.2 Raman Fibres

Table 3 contains a summary of the fibres investigated during the course of this investigation. In the table: Raman indicates a germanium doped fibre intended for use in Raman gain devices, Erbium indicates an erbium doped fibre and SC Doped indicates a semiconductor doped fibre. The 9695.01.01 was a standard monomode telecommunications fibre, with a lower germanium content than the Raman fibres.

Figure 27 is an x-ray linescan for germanium performed on a sample of fibre type 5111.01. This is a fibre with a $2.3\mu\text{m}$ core doped with 25 wt% Germanium. The vertical scale is arbitrary and proportional to the intensity of x-rays with the characteristic energy of germanium entering the detector as the beam traversed the sample. The horizontal scale corresponds to the beam position and the scale is indicated by the micron bar in the top left hand corner.

Figure 28 is the refractive index profile for the preform from which both fibre type 5111.01 and 5111.06 were drawn.

Figure 29 is the germanium concentration linescan for the core region of fibre type 5111.06. This was drawn from the same preform as the preceding fibre 5111.01. It was, however, drawn at a lower speed (73 m/min instead of 152 m/min) and is thus of a larger diameter.

Figure 30 is the backscattered electron intensity profile of a bulk sample of the core region of fibre type 5111.06. This intensity is proportional to the atomic number of the

sample and thus, in this case, to the germanium concentration.

Figure 31 shows the germanium concentration profile for fibre type 9695.01.01.

Figure 32 is the preform refractive index profile for fibre type 9695.01.01.

Figure 33 is a micrograph of the uncoated side of an ion beam thinned sample of fibre type 9695.01.01 (magnification 1000x, imaging mode SEI).

4.3 Erbium Doped Fibres

Figure 34 shows a typical X-ray spectrum from an erbium doped fibre sample. Clearly visible are the peaks for erbium, silicon and germanium. The slight hump to the right hand side of the silicon peak at around 3.4keV is a silicon Sum peak. The copper peak is due to excitation of the sample holder and microscope structure by backscattered electrons and the slight zinc peak is due to the same mechanism exciting the brass sample holder. Aluminium would be expected to be present but due to the low concentration of this element the resulting small peak is masked by the low energy end of the silicon peak and the germanium L peak.

Figures 35,36 and 37 show x-ray linescans for fibre types 3023.02, 3023.03 and 3023.04 respectively. In order to separate effects due to differences in specimen thickness and density from those due to the variation in erbium concentration a background linescan was acquired from a window drawn adjacent to the erbium peak. These two linescans are reproduced at the bottom of the figure as raw data, though

some of the detail will have been lost due to the line pattern used to distinguish the different traces. In each case the peak erbium count was around 40 counts per second and the background around 10-15 counts per second.

Also reproduced in each figure is the Germanium concentration profile showing the central depletion zone and a processed plot showing erbium peak-minus-background, expanded and smoothed.

Tables 4, 5 and 6 show the results of semi-quantitative analysis of the cores of the above fibres.

Tables 7 and 8 show the results of spot analyses of the core centres of the erbium doped fibres 3126.01.02 and 3126.02.02 respectively. In the case of table 8 a gross integral column is included. This allows calculation of the standard deviation. In this case it is 104 counts, more than the erbium peak of 80 counts.

If the ratio of erbium background to total silicon and germanium counts is assumed constant it is possible to estimate the standard deviation in the analysis of erbium in the 3126.01.02 fibre. In this case the standard deviation is 101 counts, almost twice the net peak integral.

Table 9 shows the results of a spot analysis of fibre type 3124.01.

4.4 Semiconductor Doped Fibres

Figure 38 is a micrograph of the core of a semiconductor doped fibre. This clearly shows the pronounced ovality often associated with the rod in tube method of fibre manufacture.

Table 10 shows the results of x-ray analysis of a sample of bulk core glass type Schott RG630 as used in the manufacture of the 2073 series of semiconductor doped fibres.

Table 11 contains the results of a chemical analysis carried out at British Telecom Research Labs.

Table 12 shows the results of an x-ray analysis of a sample of type Hoya 640 glass used in the cores of the 2074 series of semiconductor doped fibres. Table 13 shows the results of a chemical analysis carried out at BTRL.

Table 14 lists the results of a chemical analysis of the glass used to form the cladding of the semiconductor doped glasses.

Figure 39 shows spectra from the core and cladding regions of a 2073.01 fibre sample. The peaks have been identified as have the areas where peaks might have been expected but were not detected.

Figure 40 illustrates the x-ray linescans for the elements zinc, sodium and potassium for fibre type 2073.01. These elements were obviously at very different concentrations so the linescans have been normalised to the same vertical extent to facilitate comparison of the profiles.

Figure 41 shows the linescans for the remainder of the elements detected in fibre type 2073.01, namely calcium, aluminium, arsenic and selenium.

Table 15 lists the results of an x-ray analysis of the core of fibre type 2073.01.

Figure 42 shows the linescans for zinc, potassium and sodium in fibre type 2073.02, whilst figure 43 shows those

for calcium, aluminium, arsenic and selenium.

Figure 44 is of the linescans for zinc, potassium and sodium in fibre type 2073.03 and figure 45 shows the linescans for calcium, aluminium, arsenic and selenium in the same fibre.

Table 16 contains the results of an x-ray analysis of the core of fibre type 2073.03.

Table 17 lists the results of an analysis of the cladding layers of fibre type 2074.03

Table 18 shows the result of an analysis of a sample of pure zinc.

Figure 46 demonstrates the effect of subtracting the correct proportion of the zinc L_{α} signal from the measured sodium profile in an attempt to obtain a reliable sodium concentration profile.

Figure 47 shows the measured zinc, potassium and sodium profiles in the very large core area of fibre type 2074.01.

Figure 48 is a comparison of the spectral region adjacent to the sodium K_{α} peak as detected by the wavelength and energy dispersive detectors.

Figure 49 shows the concentration profiles for sodium, potassium and zinc for fibre type 2074.01. In this case the sodium profile was measured by use of the wavelength dispersive detection system and the potassium and zinc profiles are as measured using the TEM and energy dispersive system.

Figure 50 shows the Zinc profiles for the three different

samples of fibre type 2075.04; the as drawn fibre, a fibre heat treated at 530°C for 18 hours and one treated at 550°C for 8 hours. As the core size and shape variable due to the limitations of the rod-in-tube manufacturing method the effective magnifications of the linescans have been altered by the software to normalise the core regions to the same diameter. These adjustments to the magnification have been repeated in figures 51 and 52.

Figure 51 is a plot of the measured calcium concentration profiles for the three fibres. The magnifications have been normalised according to the ratios of the cores as delimited by the zinc concentration. The zinc concentration profile for the as drawn fibre has also been reproduced for comparison of diameter.

Figure 52 shows the selenium concentration profile for the three fibre samples, again with normalised magnifications and with the as drawn fibre zinc concentration for comparison.

Figure 53 shows the potassium concentration in the two heat treated fibres along with the potassium and zinc profiles from the as drawn fibre. The heat treated fibre potassium profiles are raw data except for a two point smoothing operation. The as drawn fibre potassium profile has undergone a background subtraction which explains its lower magnitude. The background window was set up so as to include a proportion of the calcium peak shoulders similar in size to that extrapolated to be included in the potassium window. The background subtraction, then, should subtract the effects of both the background radiation and, to some extent, the contribution in the

potassium window of the calcium characteristic radiation.

Figure 54 shows zinc and potassium profiles for the entire fibre sample heat treated at 550°C for 8 hours. The zinc rich region at the left hand side is a part of the brass tube in which the fibres were set.

Tables 19,20 and 21 show the results of x-ray spot analyses of the three fibre cores of the treated and as drawn 2075.04 fibre.

4.5 Investigation of Fibre Draw-Down Region

Figure 55 shows a number of germanium profiles from the preform draw down region and for the fibre normalised to the same diameter to facilitate the comparison of the shape of the profiles.

Figure 56 shows the germanium concentration profiles for a large section of preform rod code number 3115 and a sample of the fibre pulled from the preform, code number 3115.01. The two scales have been normalised to account for the ratios of the outside diameters of the two samples and also to allow for the inaccuracies of the microscope magnifications.

Chapter 5

Discussion

5.1 Evaluation of the Experimental Technique

As the primary aim of the project was to develop a technique to facilitate the preparation of optical fibre samples for TEM to increase the resolution of x-ray analysis, the first part of this discussion will be concerned with the effectiveness of the technique in satisfying this aim.

5.1.1 Calibration of Microscope Magnifications

On each micrograph a magnification is printed by the microscope. This magnification actually refers to the magnification of the image on the microscope viewing screen rather than the final print as this can be reproduced on any size of paper.

Of more importance than the absolute calibration of the magnification, from the point of view of the investigation of the preform draw-down region, was a knowledge of the self consistency of these magnifications in the 100x to 10,000x range.

The way in which the relevant data were acquired was covered in section 3.3.3.

Figure 16 is a micrograph of a grid hole with the cross grating resolved in order to correlate the size of the grid holes with the grating squares. It shows that the diameter of the grid hole to the left of the central hole in the calibration standard is $75\mu\text{m}$.

This micrograph also shows that the field of view is

somewhat distorted, with the circular grid hole appearing to have 10% ovality.

Figure 17, the grating at 10,000x, also shows this ovality, with 15 crossings in 98mm in the horizontal direction and 15 crossings in the vertical direction in 84mm. In this case the distortion is 15%.

Such a distortion would be expected with a tilted sample, indeed the scan rotate module has a device to correct for this effect. However these micrographs were taken at zero tilt so distortion of the image in the micrographs would appear to be a fault with the microscope. The distortion could be corrected for with the tilting correction function of the scan rotate module if required.

These micrographs were all taken with the scan rotated through 90° to ensure consistency with the x-ray linescans. The reasons for this rotation will be covered in section 5.1.4.

Measuring appropriate features in the horizontal (x-ray scan) direction on the micrographs shows that the true magnifications, if the negatives are printed at such a size that their lengths are 108mm from the edge of the image to the bottom of the identification numbers, are:- 9979x at 10,000x, 293x at 300x, 200x at 200x and 80x at 100x.

As mentioned in section 3.3.1, some doubt must remain about the reproducibility of the results for the notional 200x and 300x magnifications.

In the case of the x-ray linescans there is a further possible cause of error. The 500 second linescan of the microscope actually takes 532 seconds whereas the 500 data

points are output by the A/D converter in 447 seconds. This disparity has been allowed for in the plotting software (assuming that all higher magnifications are as close to their real values as the 10,000x one) and so the micron bars on the plots can be considered to be fairly well calibrated.

5.1.2 Determination of Effective Electron Probe Size

The effective size of the electron probe depends on both the size of the focused spot on the sample surface and on the subsequent beam spread inside the sample. The degree of beam spread in the sample depends on sample composition and is also a strong function of sample thickness.

Electron Beam Spot Size

Using the technique outlined in section 3.3.1 the electron beam spot size was measured at 35nm. This is an estimate of the maximum size of the spot under the beam conditions used. In this case the actual spot size may well be smaller as there was significant contamination build up on the sample during the course of the measurement. This contamination can be clearly seen in Figure 22.

For most measurements the beam size was larger than that used in the preceding measurement as most fibre cores were sufficiently large for the ultimate in resolution not to be required. In most cases a larger spot size and hence higher count rate and better signal to noise ratio were preferred.

Measurement of Specimen Thickness

Specimen thickness was measured using the contamination spot method [68]. Only a few measurements were taken as the microscope conditions necessary for high resolution analysis preclude the formation of contamination spots. Later attempts at increasing the body of thickness data have met with little success as a recent microscope refurbishment seems to have improved the vacuum to the extent that contamination spots can no longer be formed. With a sample of fibre type 9695.01.01 the thickness was measured as 900nm. In the case of a sample of 5111.01 fibre it was measured as 400nm.

It is possible when examining samples to get a qualitative feel for the sample thickness from the amount of contrast required on the STEM unit controls to resolve the details of the fibre structure. Based on this experience it is possible to say that the 9695.01.01 fibre was unusually thick, that the 5111.01 fibre was about average and a number of more short-lived samples were considerably thinner.

Beam Spread

Using the above values for the sample thickness it is possible to calculate the beam spread in the sample using the Goldstein equation (2.17) [62].

$$b = K \frac{Z}{E_0} \left[\frac{\rho}{A} \right]^{1/2} t^{2/3} \text{ nm}$$

where K is a constant of magnitude 0.2, E_0 is in keV and ρ is in g/cm².

For silica, using stoichiometrically averaged values for Z and A gives a beam spread of 50nm in a 400nm thick sample.

If this value is added to the initial spot size the effective electron probe size is found to be approximately 85nm.

5.1.3 Limits of Detectability

In section 2.9.4 it was shown that to be confidently detected the x-ray peak should be three standard deviations above the background ([64] and equation 2.22).

Using the data in the x-ray spot analysis tables, where both the gross and net integrals have been recorded, it is possible to calculate the standard deviation in the background counts. Multiplying this value by three gives the value of the net integral required to be 98.6% certain of the presence of the element. Using the ratio of this minimum integral to the actual integral allows an estimate to be made of both the minimum detectable concentration and the analysis time required to detect the element in the concentration actually present in the fibre samples. These values are tabulated in tables 1 and 2 respectively.

In the case of Erbium the minimum detectable concentration is around 0.02%.

In table 1 it can be seen that the minimum detectable concentration varies from element to element. One reason for this variation is the shape of the background continuum, visible in figures 33 and 39. It can be seen that the intensity of the background is higher in the region of Silicon (2200-2500 keV) than in the region of the spectrum where the arsenic peak is situated. This explains the difference between

the minimum detectable concentrations (MDCs) of these two elements.

Another factor in the high MDC of Silicon in this case is due to the way in which the net integral is calculated from the gross integral. The calculation uses a linear interpolation between the tops of the two outermost channels of the window. As the Aluminium and Sodium peaks lie in the shoulders of the silicon peak and the windows are not allowed to overlap the lowest energy channel of the silicon window is quite high up the flank of the peak and so the calculation yields a higher background value and hence a higher standard deviation.

The MDCs of Potassium and Calcium are higher for a similar reason; the valley between their respective peaks is at a higher level than the background continuum due to their slight overlap and the presence of the potassium $K\beta$ peak. A linear interpolation therefore detects a larger background contribution to the peaks and hence a larger standard deviation is calculated. In this case, however, the effect is real; it can be considered that the background to each peak contains a contribution from the characteristic emissions of the other.

In the same way the zinc background is increased at one side with a contribution from the copper peak due to stray electrons interacting with various parts of the sample holder and microscope column. This explains the slightly higher MDC of zinc.

These results were calculated from the data in table 17.

These data were collected at a higher count rate than most other spectra, as can be seen from the high silicon integral compared to that in table 16, despite the much shorter analysis time. The reason for this was that it was felt that the analysis conditions used for the acquisition of the data in table 17 were closest to those used in the majority of the linescans, where some analytical energy resolution was sacrificed in order to improve the counting statistics.

The analysis in table 17 was terminated by the overflow of the central silicon channel. It therefore represents an analysis where the maximum number of x-ray photons have been analysed. Had the analysis continued any longer the silicon integral would have become incorrect due to the overflowing channels resetting to zero. The data in table 1 therefore show the MDCs for the elements in this glass attainable whilst still maintaining accuracy of analysis. In situations where it was necessary merely to identify the elements present the analysis could, of course, be continued past this point.

The following table, table 2, shows the minimum analysis periods required to identify the presence of a number of elements at the concentrations in which they were actually present in fibre samples. The reason for this exercise was to determine which elements it could reasonably be expected to acquire useful concentration linescans from.

As the electron beam scans across the sample it effectively makes 500, 1 second duration spot analyses. Written into the plotting software was a routine to group together these separate analyses to effectively provide a smaller number of

analyses of longer duration. One unfortunate effect of this process is of course a degradation of the spatial resolution of the linescan.

In order for the software to be able to cope it was necessary to maintain the total number of data points. To achieve this the actual mechanism of this grouping routine took the form of a rolling smoothing routine. The program would sample the first x points and average them out, setting the middle value equal to the average. It would then move along only one data point and repeat the process. This is statistically equivalent to an x point averaging routine, but with a smooth interpolation between the reduced number of data points that would thus be created.

One problem with the linescan acquisition procedure used is that it is only a single channel device. It was therefore necessary to perform all linescans sequentially, even those measuring the background. For this reason background subtraction was a rather imprecise procedure with the x-ray linescan data as there was no guarantee that the sample had not moved slightly between the two analyses. As background radiation intensity varies strongly with sample thickness and surface relief it was possible for these variations to mask variation in the characteristic x-ray intensity.

Notwithstanding these limitations the linescans show that it was possible to analyse for arsenic, with a peak concentration of only 1%.

5.1.4 Effects of the Scan Rotate Module

It was found quite early on in the project that the direction of scan of the electron beam in linescan mode was at right angles to the tilt axis of the sample. It had been assumed that left → right on the screen corresponded to left → right on the sample, whereas in actual fact up → down on the screen corresponded to left → right on the sample. This was perceived to be disadvantageous in three respects.

i) As the electron beam scans across the tilted sample the distance between the electron beam source and the sample will vary if the scan is perpendicular to the tilt. In the case of the samples with the larger cores the scanned area was sometimes as large as $40\mu\text{m}$. At 30° tilt this would entail the beam/specimen distance varying by as much as $20\mu\text{m}$. In the TEM the working distance in the scanning modes is much shorter than in a dedicated SEM, around 200mm. If the largest of the condenser apertures were to be used the beam convergence angle would be in the region of 2×10^{-3} rad. This means that over a $10\mu\text{m}$ vertical range the spot size will vary by 20nm, not a very large effect, but one which can be avoided.

ii) As the beam scans across the tilted sample it interacts obliquely with the edge of the core material, as shown in figure 25. The effect of this is to increase the spatial extent over which the beam interacts with the core material by a distance $(t \sin \phi)$ where t is the sample thickness and ϕ the sample tilt. In a typical sample 400nm thick at 30° tilt this equates to 200nm. With a theoretical resolution of around 100nm for such a sample this is a marked reduction in

performance.

iii) Because the sample is viewed obliquely it appears foreshortened in the direction perpendicular to the tilt. If this is also the linescan direction then the actual magnification of the linescan depends on the tilt angle. The normal procedure was to examine each sample at the smallest tilt angle consistent with an adequate x-ray count rate. As the specimen is tilted the effective thickness of glass in the direction of the electron beam increases with increased tilt angle. Minimising the tilt angle therefore reduces the effective specimen thickness and hence improves both analytical and imaging resolution. As the structure of the fibre is all in the radial direction it is also beneficial to have the electron beam propagating as nearly parallel to the fibre axis as possible.

One possible drawback of this attempt to minimise the tilt angle is that the tilt angle used varied from sample to sample depending on the geometry of each situation. If the linescan direction was to remain perpendicular to the tilt axis then this would entail normalising the magnification of each sample to allow for the variations in the foreshortening effect.

All of the effects described above can be obviated by rotating the scan direction through 90° in order to bring it parallel with the tilt axis. To allow this a scan rotate module was fitted to the microscope.

The improvements that this fitment brought about are

clearly shown in figure 26, the edges of the core are resolved three times as sharply and the central depletion zone is 30% deeper when the scan is rotated.

5.1.5 Evaluation of the Experimental Technique, Conclusions

Combining the effects of the beam spread and spot size results shows that it should be possible to resolve detail down to 100nm using a thin film in the TEM.

It is difficult to substantiate this value for the actual samples as none of them contained detail on that scale. The sharpest feature on any of the fibres was the edge of the $2\mu\text{m}$ core of the 5111.01 fibre. This edge has a width of 9% of the core diameter on the refractive index profile of the preform, so it should be resolved as a 200nm feature in the core (assuming the refractive index profile measuring device to be accurate). On the x-ray linescan (Figure 27) it is resolved as a 195nm feature. It can therefore be concluded that the X-ray analytical technique described herein would appear to have a spatial resolution adequate for all the fibres examined.

The technique has also been shown to be capable of detecting constituents in concentrations as low as 0.02% by spot analyses and to acquire concentration linescans for any elements present with a concentration of at least 1%.

At this low concentration the data should be grouped into 10 second bins for statistical validity, leading to a degradation of spatial resolution. In the case of the smallest of the semiconductor doped fibre cores, $2\mu\text{m}$ in diameter, even if it was required to fit the whole core onto one linescan the

point to point spatial resolution of the analysis with an effective 50 data points would still be 100nm.

The technique can therefore be expected to resolve down to 100 nm and 1wt%.

5.2 Raman Fibres

The Raman fibres were chosen as the first fibres to be investigated as it was thought that the high level of germanium doping in the cores would be easy to detect and analyse. It was felt that the variation in core diameter would also prove a good test of the analytical resolution.

Some Raman fibres had also been investigated at British Telecom Research Labs by backscattered electron imaging of bulk polished samples and it was thought that a comparison of the techniques would be a useful cross-reference.

Figure 27 is the x-ray linescan for germanium in the core of fibre type 5111.01 and figure 28 the refractive index profile of the preform from which both this fibre and 5111.06 were drawn.

The refractive index was measured at BTRL using a technique in which a light beam is scanned across the preform in an index matched oil bath. The preform axis, the beam propagation direction and the beam scan direction are all perpendicular with this technique. The preform refractive index profile is computed from the light transfer function.

The shapes of the preform refractive index profile and the germanium concentration profile are in good agreement. (Attention should perhaps be drawn to the difference in scale,

the fibre is three orders of magnitude smaller.)

The dip in the centre of the germanium concentration profile is a feature of nearly all fibres made by MCVD. It is due to the decomposition of germania during the high temperature collapse phase of preform manufacture in turn due to the unfavourable $\text{Ge} \rightleftharpoons \text{GeO}_2$ equilibrium [7]. This effect can be reduced by etching away the depleted layers before final collapse. In practice, however, the depletion seems to have little effect on the waveguiding properties of the fibre. The ratio of the dip as resolved by the x-ray technique to that measured in the refractive index profile is a good qualitative measure of the resolution of the analysis.

Comparing figure 29, the germanium concentration profile for a sample of fibre type 5111.06 with figure 30, the backscattered electron intensity plot for a bulk sample of the fibre performed by BTRL, it can be seen that both the x-ray and backscattered electron techniques obtain profiles in good agreement with the refractive index profile of the preform.

As described in section 2.8.1 backscattered electrons have a smaller interaction volume than x-rays in a bulk sample. It can be seen in figure 24, however, that the resolution is not as good as the x-ray technique when the latter is performed on a thin film. A further disadvantage of the backscattered electron technique is that the contrast depends only on specimen density/atomic number, and so cannot distinguish between more than two elements. It is also of little value if the dopants are only present at low levels or are close in atomic number to the host material so that they do not affect

the backscattering coefficient.

The backscattered electron technique does, however, have the advantage of a much simpler specimen preparation procedure and is therefore much faster. As such it would probably be preferred in situations where the above problems can be neglected.

Figures 31 and 32 show the germanium concentration profile and preform refractive index profile respectively for fibre type 9695.01.01.

Once again the shapes of the two profiles are in good agreement. The core of this fibre is both bigger at $10\mu\text{m}$ and has a considerably lower level of germanium doping, only 5 mole%.

The undulations visible in the cladding layers on the refractive index profile are due to the phosphorus doping used to lower the sintering temperature of the glass [53]. This phosphorus was at too low a concentration to be detected by the technique, especially as the small phosphorus peak would have been almost entirely obfuscated by the tails of the adjacent silicon peak.

The phosphorus doped cladding layers did cause one phenomenon. Figure 33 is a micrograph of the uncoated side of a sample of 9695.01.01 using SEI. The micrograph shows most of the fibre, with the mounting resin visible in the top and bottom left hand corners. The dark circle in the centre corresponds to the fibre core and the dark streaks to the left of the core are carbon contamination.

The first assumption was that the light rings were some form of charging or self lensing effect as they have the appearance of a diffraction pattern. To investigate this possibility several micrographs were taken at different accelerating voltages. These showed that the pattern did not change with potential or electron wavelength and so it was determined that the pattern was a feature of the sample.

Close inspection of the refractive index profile shows a peak in the refractive index of the cladding layers corresponding to each of the brighter rings. As SEI is sensitive to surface topography it was decided that the varying chemical composition of the glass had led to preferential etching in the ion beam thinner and hence to a set of raised rings.

The effect was not noticed on any other samples and may be very sensitive to the precise ion beam thinning conditions.

In conclusion, these results would seem to justify the assumption of the fibre manufacturers that the refractive index profile of the preform does not change as it is drawn into fibre.

5.3 Erbium Doped Fibres

The aim in examining the erbium doped fibres was to investigate the effectiveness of attempts to confine erbium in the central core region.

During the collapse phase of preform manufacture volatile species tend to be lost. This effect has already been discussed in the case of germanium depletion in the centre of

the Raman fibres. Erbium is also a volatile species, but as described in [18] there is a degree of interaction between erbium and the non-bridging oxygen in alumina. Alumina has a very low vapour pressure even at the temperatures required to collapse a preform tube nor does it form a volatile suboxide (unlike germanium) and it was therefore hoped that this interaction would inhibit the depletion of erbium in the core centre.

The first erbium doped fibres to be investigated were fibre types 3023.02, 3023.03 and 3023.04. All these fibres were drawn from the same preform, but at differing temperatures (2125°C, 2155°C and 2160°C respectively) and correspondingly different drawing rates (28,47 and 85 m/min respectively) to give core diameters in a 1:0.83:0.6 ratio.

Initial linescans for erbium and aluminium in these fibres were encouraging, showing two very similar peaks for both aluminium and erbium in the core centre. Microscopical examination of the fibre cores, however, showed that in many cases the core centres appeared darker than the rest of the core. It was considered that this could be caused by two effects. If the aluminium doped silica had a lower sputtering rate than the undoped silica then differential sputtering in the ion beam thinner would lead to a thickness variation which would in turn lead to an increase in background count in the centre of the core. Alternatively, if the aluminium doping levels were high enough, the higher density of alumina compared to silica would also lead to an increase in overall

counts in the core centre. (The densities of silica and alumina are 2.2 and 3.8 g/cm³ respectively).

In addition to the preceding problems, the aluminium peak lies on the shoulder of the silicon peak. The germanium depletion in the centre of the core is matched by a corresponding increase in silicon concentration. This leads to an increase in silicon counts in the core centre and in turn to an increase in the count rate in the aluminium window. This was considered to be the main reason for the shape of the first aluminium linescans. No aluminium peak is visible on the spectrum reproduced in figure 34 whereas the erbium peak is clearly identifiable.

In the case of the erbium linescans it was possible to draw a background window adjacent to the peak window and perform a background subtraction as all the extraneous counts in the erbium window were due to the Bremsstrahlung background. Due to the gradient of the spectrum adjacent to the aluminium peak it was not possible to draw a suitable background window and so no definitive aluminium profiles could be acquired.

Figures 35, 36 and 37 show the results of linescan acquisition and background subtraction for fibre types 3023.02, 3023.03 and 3023.04. These fibres were doped with around 1wt% erbium. This is an unusually high concentration, 0.1% is more normal in fibres intended for actual applications in order to avoid ion-ion interaction effects.

It can be seen in the linescans at the bottom of the figure that the erbium count rate is convincingly higher than the background count rate in the centre of all three fibre cores.

These results show that erbium loss from the core centre during the preform collapse phase has been successfully avoided in these fibres.

This conclusion is supported by tables 4,5 and 6 which show the results of semi-quantitative analysis of the central core regions. In all but the smallest core the erbium concentration is at least as high as expected. The technique for deposition of erbium in the core is rather imprecise, depending on the desiccation of an erbium salt solution in an incompletely sintered preform [33] and so variations in erbium concentration might be expected. This might explain the low concentration of erbium measured in the 3023.02 fibre.

It is difficult to say what concentration of erbium should be detected in the cores. Analysis of the whole core region showed an average concentration of 0.5 wt% (Private communication, BTRL), but the actual peak concentrations may well be four times this.

Three other types of erbium doped fibre were supplied, but with a reduced expectation of successful analysis due to much lower levels of erbium and aluminium doping.

Fibres 3126.01.02 and 3126.02.02 both had core centres doped with 0.1 wt% aluminium and a few hundred parts per million erbium, the levels were too low for the sponsoring establishment to perform a chemical analysis). Sample 3124.01 had no aluminium at all, and it was hoped that it might be possible to show that the erbium had not been confined to the core in this case.

It was not possible to obtain meaningful linescans for these fibres for any elements other than germanium.

It was also difficult to obtain convincing spot analyses of the core regions of these fibre samples. The erbium concentrations were so low that insufficient counts were collected before channel overflow occurred in the silicon peak.

It can be seen in tables 7 and 8 that in the case of the aluminium doped fibres there may be some indication of a very small amount of erbium. Table 8 includes a gross integral column and from this it is possible to calculate the standard deviation in the background. In both cases the size of the erbium peak, if it exists, is in the order of one standard deviation. The normal criterion for proof of the presence of an element is that the peak integral should exceed the gross integral by three standard deviations, a criterion clearly not satisfied by these data.

However, in the cases of both these fibre samples the results were repeated three times, and each time a peak in the order of one standard deviation was detected. This would tend to support the conclusion that some small concentration of erbium was being detected.

In the case of the fibre not doped with aluminium, 3124.01, no counts at all were detected in the erbium window on any of three successive analyses, one of which is shown in table 9.

The analysis of erbium in these fibres involves working at the very limit of the detector resolution and also at the limit of experimental statistics.

In theory, for experimental data following a Poisson distribution the certainty of the validity of a result is 99.7% for a variation from background of three standard deviations. If the peak magnitude is only one standard deviation this certainty drops to 68%. The fact that the result was successfully repeated three times increases this confidence level somewhat. Nevertheless the best that can be said of these results is that they support, rather than prove, the notion that erbium depletion in the core region is prevented by the addition of aluminium as a co-dopant.

The large variation in apparent germanium concentration may be due to variation in the precise point in the germanium depleted core region where the analysis was performed.

5.4 Semiconductor doped fibres

Fibre types 2073, 2074 and 2075 are all semiconductor doped fibres manufactured by the rod in tube method (section 2.7.1) from commercially available coloured filter glasses. In the case of these fibres the core glasses were Schott RG 630, Hoya H640 and Hoya H720 respectively. In the case of these glass designations Schott and Hoya refer to the glass manufacturer and the subsequent number to the nominal wavelength of the absorption edge. This method tends to produce a core with a pronounced ovality (See figure 38) which complicates the comparison of analyses of similar fibres as the core diameter varies with scan direction and from fibre to fibre. To minimise this problem the scans were done in

the direction of minimum core diameter.

The first of this class of fibres to be investigated were fibres 2073.01, 2073.02 and 2073.03. These were all pulled from the same preform, the first two at 1150°C and 2073.03 at 1200°C. Chemical analyses of the compositions of the core and cladding glasses were provided by the collaborating establishment and these are shown in tables 11,13 and 14.

The qualitative differences between the compositions of the core and cladding glasses can be seen in the relevant spectra reproduced as figure 39.

Reproduced in tables 10 and 12 are the corresponding x-ray analyses performed on thin film samples of the bulk glasses from which the fibre cores were manufactured. The reason for using thin films in this case was to cut down on the degree of x-ray absorption and so preserve consistency between the bulk and fibre samples.

The differences apparent between the results from the two methods of analysis are due to the presence in the samples of elements not detected by the x-ray analyser. In the case of these glass samples around two thirds of the atoms present in the sample are oxygen which are simply not detected. The effect of this is to increase the apparent concentrations of the elements which are detected to three times their true level. If the co-ordination of all the elements present are known it is possible to calculate the true concentrations of the elements from stoichiometry. In the case of these data the calculation has been performed in reverse to remove the effect of oxygen from the chemical analyses and thus to

compile an apparent concentration column in the chemical analysis tables. Comparing these analyses with the measured concentration profiles in figures 40-45 it can be seen that most of the elements are distributed according to the compositions of the component glasses. The core and cladding regions are clearly delimited with no apparent diffusion occurring between the two zones.

The selenium profile shows that this semiconducting species is retained in the core during fibre drawing. The sulphur peak was too small to allow the acquisition of successful linescans, partly due to the high level of the background radiation in this region. The cadmium $L\alpha$ and $L\beta$ peaks were overlapped by the calcium and potassium peaks whilst the higher order L peaks would have been too small to detect anyway. The cadmium K lines lie above 20KeV which was outside the range of the detector.

Arsenic did not feature in the original chemical analyses but its presence is not unexpected. Arsenic oxide is a commonly used fining agent.

Closer examination of the profiles brings to light certain peculiarities with the potassium and sodium profiles. From the analyses the potassium concentration profile would be expected to peak in the core region, whereas in the measured profiles it is largely flat.

Even more surprising is the shape of the sodium profile, which should dip in the middle, but in these profiles shows a distinct peak.

The most likely explanation for this anomalous result for the sodium profile was considered to be an overlap between the sodium $K\alpha$ line at 1.04keV and the zinc $L\alpha$ line at 1.10keV.

The first attempt to deconvolve the two peaks involved measuring the ratio between the $K\alpha$ and $L\alpha$ peaks for a sample of pure zinc. A fraction of the zinc K signal corresponding to the zinc L signal was then subtracted from the measured sodium profile. The ratios of total counts of the zinc K and L peaks were measured as 88:1 including the background, or 125:1 for the characteristic radiation alone.

It can be seen in figure 46 that this technique was not entirely successful. A more positive technique was required and so it was decided to attempt to use a detector with a higher resolution in order to separate the two peaks.

In addition to the TEM, a JEOL JXA 840A electron probe microanalyser was available. This is basically an SEM equipped with a more advanced EDS detector than the TEM and also a wavelength dispersive spectrometer. Being an SEM the microprobe has a much poorer spatial resolution of analysis than the TEM and so a fibre with a core much larger than the $2\mu\text{m}$ of the 2073 series fibres was required. To this end a sample of fibre type 2074.01 was obtained, this being a fibre with a $25\mu\text{m}$ core manufactured from a similar glass to the preceding 2073 series fibres. In the case of the 2074.01 fibre the core was actually manufactured from Hoya H640 glass (tables 12 and 13).

Analysis of this fibre in the TEM showed that the sodium profile was again the inverse of that expected (Figure 47),

and so the fibre was expected to be a good large scale analogue of the earlier fibres.

This fibre also showed a clear potassium diffusion profile, which suggests an explanation for the failure to detect potassium in the smaller fibre cores. In the larger fibre the potassium can be seen to have diffused a distance in the order of $20\mu\text{m}$ (assuming that the zinc has not diffused). In the case where the fibre core is itself in the order of this size the potassium concentration in the increased volume is not markedly diminished.

If the potassium in the smaller cored fibres had a similar mobility then the lack of potassium in those linescans is explained. The ratio of the core area to the diffused area is in the region of 100:1. As there is no diffusion in the axial direction (the geometry of the fibre is such that there is no axial concentration gradient) then the initial concentration of potassium will be reduced a hundredfold. The initial potassium concentration was 28wt% so such a reduction would leave a potassium concentration of $<0.3\text{ wt}\%$ if the cladding glass contained no potassium. This is below the detectability threshold for concentration linescans although it is high enough for spot analyses. In fact the cladding glass contains an apparent concentration of 3% potassium and so it would be expected that the level of potassium would equilibrate to around the 3% level throughout the fibre. This idea is supported by the x-ray analysis data in tables 15, 16 and 17. There is a possibility that the potassium and sodium mobilities

might vary between the different fibres due to variations in core glass composition.

The Energy dispersive detector in the microprobe proved unable to resolve the zinc and sodium peaks and so the wavelength dispersive system was used. The difference in the resolution of the two techniques can be clearly seen in figure 48. The sodium concentration profiles measured using both techniques are reproduced in figure 49. It is clear that the profiles are markedly different with the sodium profile measured by WDS being in much closer agreement to that which would be expected from the compositions of the constituent glasses.

It would be expected that the sodium and potassium would have roughly similar mobilities in silica because in this situation the requirement of conservation of charge neutrality means that the two ions will have to diffuse at the same rate [16].

If the sodium ions, with a higher mobility, diffuse into the core more rapidly than the potassium ions diffuse out of the core a negative charge will build up in the cladding layer, opposing the diffusion of the sodium and enhancing that of the potassium. Therefore both species can be expected to have a common diffusion coefficient intermediate between that normally associated with each species separately in pure silica.

The sodium and potassium profiles would therefore be expected to be a mirror image of each other and figure 49 shows that this is indeed the case.

It can be seen from these results that the spectral resolution of the wavelength dispersive system is far better than that of the energy dispersive system. In the context of this investigation, however, it had several drawbacks.

The main disadvantage of the system was that the disk operating system used by the Link AN10000 analyser on the electron microprobe is incompatible with MS-DOS, the disk operating system used on the vast majority of microcomputers, including those used to acquire the data, process the data and eventually plot it. The only way to transfer the data from one system to the other was to copy the spectrum files one at a time onto separate disks. These disks were then converted to be MS-DOS readable using the "Chkdisk" utility which converts all the disk blocks into separate files. These files then had to be checked one by one (all 120 of them) to find out which one contained the data, the empty files deleted and the required data reformatted to be compatible with the plotting software. It is fortunate that the AN10000 only stores 128 data points so that all the data can be stored in one 256 byte disk block.

It would have been possible to examine thin film samples in the SEM but it was much easier to locate the fibre cores using TEM than SEM.

Having shown that the sodium concentration mirrored the potassium concentration as expected, and that considerable co-diffusion of potassium and sodium was occurring it was decided in light of the difficulties associated with

acquisition of sodium profiles to concentrate on the potassium diffusion profiles and to assume that the sodium would continue to mirror this behaviour.

In order to further investigate diffusion, and to see if any further diffusion occurred during the heat treatment stages necessary to cause crystallite formation in the semiconductor doped cores some samples of fibre type 2075.04 were obtained. This fibre was chosen as it was available in three states of heat treatment and it was hoped that the large core size would offset the problems of a reduction in potassium concentration due to diffusion into a large volume.

The core glass used in these fibres was Hoya H720, similar in composition to the H630 used in the 2074 series fibres but with 6% more zinc and the addition of 2% barium.

Examination of the zinc profiles showed a variation in apparent core diameter as delimited by the concentration profile of this element. As previous samples had failed to show any evidence of zinc mobility it was assumed that this variation was due to the vagaries of core shape and diameter inherent in the rod-in-tube route to fibre manufacture. The magnifications of the profiles in figure 50 were therefore adjusted to normalise the apparent core diameters to the same size in all three plots. These magnification modifications were also applied to the profiles in figures 51 and 52 to allow for the investigation of any variations in mobility for the elements calcium and selenium from that of zinc.

Examination of figures 51 and 52 shows that the apparent

sizes of the cores as delimited by calcium and selenium are the same in all three fibre samples. This would seem to indicate that these elements are immobile in a silica matrix at temperatures up to the drawing temperature (1245°C) for short times, at a temperature of 550°C for eight hours and at a temperature of 530°C for eighteen hours. This is as would be expected from consideration of the diffusion coefficients of these elements [16]. Multivalent cations have diffusion coefficients orders of magnitudes lower than monovalent cations in a silicate matrix. Previous results have demonstrated that potassium can diffuse 20µm during fibre drawing so from consideration of the ratios of the diffusion coefficients of calcium and selenium these might be expected to move as much as 200nm, or one fiftieth of a core diameter.

Figure 53, however, shows that this immobility is not the case for potassium. The linescans show a gradient in the potassium concentration in the as drawn fibre peaking in the core region (marked by the zinc profile). This concentration profile is not seen in the heat treated fibres, which would seem to indicate that further diffusion of potassium is occurring during the heat treatment stages.

Figure 54 shows the potassium and zinc concentration profiles across the entire sample of the higher temperature heated glass. It can be readily seen that the potassium concentration shows no systematic variation across the fibre diameter and also that the potassium signal is fairly high above zero.

It can be inferred from the requirement that charge neutrality must be conserved that the sodium concentration must also become homogeneous during the heat treatment stage.

5.4.1 Interdiffusion Model for Potassium and Sodium

Doremus [16] gives an equation for the common diffusion coefficient of two interdiffusing species:-

$$D_{\text{interdiffusion}} = \frac{D_a D_b}{N_a D_a + N_b D_b} \dots\dots\dots (2.4)$$

Also in the same reference is a table which states that the ratio of the diffusion coefficients of sodium and potassium is 1:2. Using equation (2.4) and assuming both this ratio and an equal initial concentration of sodium and potassium (the initial concentrations measured by chemical analysis in tables 11,13 and 14 are similar for both potassium and sodium in the core and cladding glasses respectively) it can be calculated that the interdiffusion coefficient for sodium and potassium is two thirds that of the sodium.

Equation 2.8 gives the concentration in the centre of a diffusing cylinder as a function of time and diffusion coefficient. In the case of the heat treated and as drawn semiconductor fibres we know the initial concentration C_0 and the core composition C_1 after an unknown heat treatment during fibre drawing in the case of the as drawn fibre and also the core composition C_2 after two further heat treatments.

Reformulating equation 2.8 in terms of the treatment time

gives two simultaneous equations:-

$$t_1 = \frac{-a^2}{4D \ln(1-C_1/C_0)} \dots\dots\dots 5.1$$

and

$$t_2 = \frac{-a^2}{4D \ln(1-C_2/C_0)} \dots\dots\dots 5.2$$

where t_1 is the (unknown) heat treatment time of the as drawn fibre, t_2 is the heat treatment time of either of the treated fibres, C_0 is the initial core concentration, C_1 is the core concentration in the core of the as drawn fibre, C_2 that in the treated fibre and a is the core radius.

Subtracting 5.1 from 5.2 gives an expression for the diffusion coefficient in terms of the known concentrations in tables 10, 19, 20 and 21 and the heat treatment time (t_2-t_1).

ie:-

$$D = \frac{a^2}{4(t_2-t_1)} \cdot \frac{L_2-L_1}{L_1L_2} \dots\dots\dots 5.3$$

where $L_i = \ln(1-C_i/C_0)$

This procedure allows the approximate calculation of the minimum value of the diffusion coefficient required to have led to the reduction in core potassium observed between the as drawn and heat treated fibres.

For the fibre treated at 550°C for 8 hours using the data in tables 12, 19 and 20; $C_0=18\%$, $C_1=4.2\%$ and $C_2=0.2\%$ if a constant background level of 2% potassium is assumed.

Inserting these values into equation 5.3 gives a minimum value for the diffusion coefficient of $4.8 \times 10^{-14} \text{ m}^2\text{s}^{-1}$. This is about two orders of magnitude less than would be expected for the interdiffusion of sodium and potassium in a silicate glass.

The high proportions of other elements in the glass would be expected to change the diffusion coefficient. The mixed-ion effect alone is known to reduce the conductivity of glass by up to two orders of magnitude and calcium also reduces diffusion coefficients of monovalent cations. These results also show the minimum diffusion coefficient required to have reached the observed position. The values of C_2 especially are rather unsubstantiated and the fibres analysed may have been fully equilibrated within minutes of the start of the heat treatment. The equation used assumes an infinite medium which, in the context of the mobility of potassium, the fibre is not. The general background level of potassium is also a complication.

Of more interest than the measurement of diffusion coefficients during heat treatment would be some understanding of the diffusive processes prevalent during fibre drawing.

The time-temperature cycle during fibre drawing is represented by a complicated integral [25,26], as is the equation governing preform neck-down [59]. To provide a mathematical model of diffusion processes during fibre drawing it would be necessary to combine Ficks equation in a co-ordinate system shrinking according to one equation and with a time-temperature cycle governed by another. As all three of the equations usually require solution by numerical methods it seems unlikely that an analytical solution could be found to such an assembly and an empirical equation might be of considerable value.

The temperature/time regime during fibre drawing is in effect measured by the diffusion behaviour of the elements in the fibre. The temperature cycle is encoded into the effective value of the diffusion coefficient and the associated time cycle is encoded into the time term. It is impossible to deconvolve the two terms but their sum, Dt characterises their combined effect on the diffusion behaviour of the potassium.

Using equation 2.8:-

$$C = C_0 (1 - e^{-a^2/4Dt})$$

it can be shown that:-

$$Dt = \frac{-a^2}{4 \ln(1-C/C_0)} \dots\dots\dots (5.4)$$

Using this equation and data from the core glass analysis (Table 12) and the as drawn fibre core analysis (Table 19) gives a value for Dt of:-

$$Dt = 9.4 \times 10^{-11} \text{ m}^2$$

This value is an empirical measure of the time-temperature cycle during fibre drawing and if this value of Dt were to be multiplied by the ratio of the diffusion coefficients of potassium and another element it could be substituted back into the diffusion equations in order to estimate the diffusion behaviour of that element during fibre drawing, at least under the drawing conditions prevailing during the manufacture of this fibre.

5.5 Investigation of Preform Draw-Down Region

The data acquired in the earlier parts of the investigation seemed to indicate, as expected, that the shape of the germanium concentration profile remained unchanged during the

preform draw down stage. To further investigate this stage of fibre manufacture, and also to check that the ratio of core size to fibre size remained the same, a section of preform end from which fibre had been drawn was supplied, along with a section of the fibre. The fibre used was an erbium doped fibre 3115.01, but the investigation was limited to the germanium doping concentration profile.

To see if the germanium concentration profile varied at all during fibre drawing a number of profiles were acquired at a variety of magnifications. These are shown in figure 55. As can be seen the shape and gradient of the outer edge of the fibre does not seem to vary during the process, though in the smaller sections the depth of the central depletion region seems to be reduced. This latter effect is probably due to a resolution limitation as these profiles of the preform sections were acquired from bulk samples. In the case of the smallest sample the diameter of the sample was 2.7mm, indicating a core diameter of around $30\mu\text{m}$. The normally stated resolution of analysis in a bulk sample is around $2\mu\text{m}$, but this assumes a low electron energy around 20keV. These analyses were performed in the TEM at 100keV in order to have directly comparable results between the fibre and bulk x-ray data. This would be expected to increase the interaction volume and hence degrade the resolution of the analysis.

To investigate any change in effective core diameter with respect to fibre diameter the data in figure 56 were acquired.

Intermediate sections between the two shown were also

examined, but the scaling errors in the 200x and 300x magnifications precluded their use. Both curves have a very similar shape and are very close in size. As the scale of the preform section relies for its accuracy on a measurement taken from a micrograph of a feature 6mm long the experimental measurement errors are too large to interpret the slight size disparity as meaningful.

This reinforces the conclusion reached from examination of the Raman fibres that the preform refractive index profile persists unchanged into the fibre. It also indicates that the ratio of preform core diameter to overall diameter is the same as that of the fibre and fibre core. This means that fibre core diameters can be determined accurately from preform data and fibre diameter measurements.

Chapter 6

Conclusions

6.1 Experimental Procedure

- 1) The primary aim of the project was to develop an experimental technique for the preparation and analysis of optical fibres. A technique has been developed which will generate x-ray concentration linescans from fibre samples with a spatial resolution of better than 100nm for elements with peak concentrations above 1 wt%.

- 2) Using the technique it is possible to perform analyses of selected 100nm diameter areas of the sample and to analyse for elements present in concentrations down to 0.02 wt%.

6.2 Fibre Investigations

- 3) Investigation of germanium doped Raman fibres has shown that the refractive index profile built in during preform manufacture is transferred into the fibre without any distortion or diffusion.

- 4) Investigation of erbium doped fibres has shown that erbium volatility is reduced by doping with aluminium so that erbium deposited in fibre preforms remains in the glass during preform collapse.

- 5) Erbium has been detected in concentrations higher than can normally be achieved, supporting the theory that rare-earth solubility in a silica matrix is enhanced by aluminium doping.

- 6) Ionic diffusion of monovalent cations occurs in

multicomponent glass based semiconductor doped fibres during both the fibre drawing stage and subsequent heat treatment.

7) The effective value of the term Dt from the diffusion equations was determined as being $9.4 \times 10^{-11} \text{m}^2$ for the diffusion of potassium during fibre drawing. If the value of the diffusion coefficient of potassium in the host glass were known it would be possible to predict the diffusion behaviour of any other element for which the diffusion coefficient was known during a similar fibre drawing regime.

8) Investigation of the preform neck-down region has shown that the fibre core/diameter ratio and refractive index profile are constant throughout the fibre drawing process.

Chapter 7

Suggestions for Further Work

This project involved the development of a technique and the application of this technique to a variety of fibres which were readily available.

Further investigation of the material properties of fibres would require the fabrication of fibres especially for the project.

Further work is required on the interaction of erbium and aluminium. This would ideally involve the fabrication of a series of fibres with high levels of erbium doping and a systematically reducing aluminium concentration. This approach might lead to problems of erbium precipitation but the technique of sample preparation also facilitates the examination of samples by TEM which could provide a means of investigating this phenomenon. The present analysis method has too large an interaction volume to spot any graininess in the erbium distribution so an examination by TEM might prove to be useful in its own right.

More useful data could be gained from Surface Ion Mass Spectrometry of glasses containing erbium and aluminium in order to find out the precise nature of the interaction between the two elements.

In the case of the semiconductor doped fibres work needs to be done on measuring the diffusion coefficients of monovalent cations in glasses with the precise composition of those used for fibre fabrication. This data could probably be readily acquired through electrical conductivity measurements of bulk

glass samples.

Investigation of the diffusion profiles in a glass fibre manufactured by the rod and tube process from a simple binary sodium silicate glass cladding and binary potassium silicate glass core would give more accurate information regarding the interdiffusion of elements and also give a better idea of the time-temperature cycle during fibre drawing. Such a fibre would not suffer from the zinc-sodium peak overlap problem which hampered analysis of sodium profiles in the present investigation.

Less ambitiously, it would be useful to analyse the potassium profile on a sample of the 2075.04 fibre which had had a shorter heat treatment than that actually supplied. If a heat treated fibre was available which still showed a potassium peak in the middle it would be possible to get a more definite value for the interdiffusion coefficient.

Further work should also be done to see if the diffusion of sodium and potassium in these fibres is important. The optical properties of these fibres are controlled by the growth of microcrystallites of semiconducting material. As the fibres grow largely through a diffusion process it would be expected that the glass composition would be important from the point of view of the effect that this has on the diffusion coefficient. For optimum operation of the devices assembled using these fibres the crystallite size distribution should be narrow and this is unlikely to be the case if the growth conditions are different at the core edges due to diffusion.

To investigate this a number of samples of glass could be prepared with varying amounts of potassium and sodium. These samples, given identical heat treatments, would indicate their crystallite sizes by their optical transfer properties.

References

- [1] G Goubau, J R Christian "A new waveguide for mm waves" Proceedings of the Army Scientific Conference. US Military Academy West Point New York 291-303 1959
- [2] G Goubau, F Shwering, "On the guided propagation of electromagnetic wave beams" IRE Transcripts Antenna and Propagation, Vol AP-9 No 5 248-256 1961
- [3] D W Burreman "A lens or light waveguide using convectionally distorted thermal gradient in gases" Bell System Technical Journal Vol 43 1469-1475 1964
- [4] F P Kaparon et al "Radiation loss in glass optical waveguides" Applied Physics Letters Vol 17 423-425 1979
- [5] D B Keck P C Shultz, F Zimar "Attenuation of multimode glass optical waveguides" Applied Physics Letters Vol 21 No 5 215- 217 1972
- [6] W A Gambling "9th W E S Turner memorial lecture: Glass, light and the information revolution." Glass Technology Vol 27 no 6 pp179-187 1986
- [7] Tingye Li "Optical Fibre Communications, Volume 1; Fibre Fabrication" Academic Press Inc 1985
- [8] W H Zachariesen Journal of the American Ceramic Society Vol 54 p3841 1932
- [9] R L Mozzi, B E Warren Journal of Applied Crystallography Vol 2 p 164 1969
- [10] J F Stebbins "NMR Evidence for five-coordinated silicon in a silicate glass at atmospheric pressure" Nature Vol 351 20 June 1991 pp638-639
- [11] L V Woodcock, C A Angell, P Cheesman "Molecular dynamics studies of the vitreous state: Simple ionic systems and silica" Journal of Chemical Physics Vol 65 No 4 pp1565-77
- [12] J Zarzycki "Sur l'angle de la liaison Si-O-Si de la silice vitreuse et celui de la liason Ge-O-Ge de l'oxide de Germanium vitreux ou liquide" Verres et Refractaires Vol 11 p3 1962
- [13] J Zarzycki, R Mezard "A Direct Electron Microscopic study of the structure of glass" Physics and Chemistry of Glasses Vol3 No5 1962
- [14] T P Seward, D R Uhlmann, "On the existence of microstructure in fused silica" Proceedings of the Third International Conference on the Physics of Non-Crystalline Solids, Sheffield 1970. p327

- [15] P H Gaskell, M C Eckersley, A C Barnes, P Chieux "Medium range order in the cation distribution of a calcium silicate glass" Nature Vol 350 25 April 1991 pp 675-677
- [16] R H Doremus "Glass Science" Wiley and Sons 1973
- [17] A E Owen & R W Douglas, Journal of Glass Technology, Vol 43 p 159 1959
- [18] K Arai, H Namikawa, K Kumata, T Honda, Y Ishii, T Handa "Aluminium or Phosphorus, co-doping effects on the fluorescence and structural properties of neodymium-doped silica glass" Journal of Applied Physics Vol 59 No10 pp 3430-3436 1986
- [19] J Frischat, Journal of the American Ceramic Association, Vol 53 p625 1969
- [20] J Crank, The Mathematics of Diffusion, Oxford University Press 1956.
- [21] D M Cooper, S P Craig, B J Ainslie, C R Day "Dispersion shifted single mode fibres using multiple index structures" British Telecom Journal April 1985
- [22] T Katsuyama, H Matsumura, "Infrared Optical Fibres" Adam Hilger 1989
- [23] S F Carter, P W France "Drawing induced absorption loss in multicomponent glass fibres" Journal of Non Crystalline Solids Vol 58 pp47-55 1983
- [24] K J Beales, D M Cooper, J D Rush "Increased attenuation in optical fibres caused by hydrogen diffusion at room temperature" Electronics Letters Vol 19 No 22 pp917-919 1983
- [25] E M Dianov, V V Kashin, S M Perminov, V N Perminova, S Ya Rusanov, V K Syosev "Dynamics of the drawing zone of a lightguide blank for different drawing regimes with furnace and laser heating" Journal of Engineering Physics Vol 55 No 3 pp 1059-1065 1989
- [26] V N Vasil'ev, G N Dul'nev, V D Naumchik "Nonstationary processes in optical fibre formation. 1 Stability of the drawing process" Journal of Engineering Physics Vol 55 No 2 pp 918-924 1989
- [27] R H Stolen, Chinlon Lin "Fibre Raman Lasers" Handbook of Laser Science and Technology Section 2 pp 265-273
- [28] R J Mears, C Reekie, S B Poole, D N Payne "Low threshold tunable c.w. and q-switched fibre laser operating at 1.55 μm " Electronics Letters Vol 22 No 3 p159 1986

[29] D Cotter "Observation of stimulated Brillouin scattering in low loss optical fibre at 1.3 microns" Electronics Letters Vol 18 No 12 1983

[30] R H Stolen "Nonlinear properties of optical fibres" Optical fibre telecommunications Eds E S Millar A G Chynoweth Academic Press New York 1979 621.380414

[31] Yasuhiro Aoki "Properties of Fibre Raman amplifiers and their applicability to digital optical communication systems" Journal of Lightwave Technology Vol 6 No 7 1988

[32] B J Ainslie, S P Craig, S T Davey, B Wakefield "The fabrication, assessment and optical properties of high concentration Nd³⁺ and Er³⁺- doped Silica-based fibres" Materials letters, Vol 6 No 5 pp139-143 March 1988

[33] B J Ainslie, J R Armitage, S P Craig, B Wakefield "Fabrication and optimisation of the Erbium distribution in silica based doped fibres" 14th European Conference on Optical Communications (ECOC 88) Conf Publ No292 Brighton 1988 pp62-65 Vol 1

[34] B J Ainslie, S P Craig, S T Davey "The Fabrication and Optical Properties of Nd³⁺ in Silica-based optical fibres" Materials Letters, Vol 5 No 4 p143 March 1987

[35] S Wen, J Feng "A HREM Study of Cd(S,Se) glass colouration" Journal of non-crystalline solids Vol 80 pp190-194 1986

[36] D S Chemla, D A B Miller, "Mechanism for enhanced optical nonlinearity and bistability by combined dielectric-electronic confinement in semiconductor microcrystallites" Optics Letters Vol 11 No 8 p522 1986

[37] J Warnock, D D Awschalom "Picosecond studies of electron confinement in simple coloured glasses" Applied Physics letters Vol 48 No 6 p425 1986

[38] X Chen, Y Zhu, S Sheng "Optical absorption properties of glasses coloured with Cd(S,Se)" Journal of Non Crystalline Solids Vol 80 pp455-459 1986

[39] M Dagenais, W F Sharfin, "Picojoule Subnanosecond, all optical switching using bound excitons in CdS" Applied Physics letters Vol 46 No 3 p230 1985

[40] G R Olbright, N Peyghambrian "Interferometric measurement of the nonlinear index of refraction, n_2 , of Cd(S,Se) doped glass" Applied Physics letters Vol 48 No 18 pp1184-1186 1986

- [41] R K Jain, R C Lind "Degenerate four wave mixing in semiconductor doped glass" Journal of the optical Society of America Vol 73 No5 pp647 1983
- [42] P Roussignol, D Ricard, J Lukosic, C Flytansis "New results in optical phase conjugation in semiconductor doped glasses" Journal of the Optical Society of America B Vol 4 No 1 p143 1987
- [43] D Cotter "Stimulated Brillouin scattering in monomode optical fibre" Journal of Optical Communications Vol 4 No 1 pp10-19 1983
- [44] R W Tkach, A R Chraplysy, R M Devoisier "Spontaneous Brillouin scattering for single mode optical fibre characterisation" Electronics Letters Vol 22 No 19 p1011 1986
- [45] R Y Chiao, E Garmire, C H Townes "Self trapping of optical beams" Physical Review Letters Vol 13 p 479 1964
- [46] M A Dugay, J W Hansen "An ultrafast light gate" Applied Physics Letters" Vol 15, p 192 1969
- [47] R Rossetti et al "Excited Electronic states and optical spectra of ZnS and CdS crystallites in the 15-50 A Range: Evolution from molecular to bulk semiconducting properties" Journal of Chemical Physics Vol 82 No 1 p552 1985
- [48] A I Ekimov, A A Onuschenko "Size quantisation of the electron energy spectrum in microscopic semiconductor crystals" JETP Letters Vol 40 No 8 p1136 1984
- [49] Yan Fuyu, J M Parker "Quantum size effects in heat treated Cd(S,Se) doped glasses" Journal of Non-Crystalline Solids Vol 112, pp 277-281 1989
- [50] I M Lifshitz, VV Slezov "Kinetics of diffusive decomposition of supersaturated solid solutions" Soviet Physics JETP Vol 35(8) No2 pp331-339 1959
- [51] H J Tress "Ruby and related glasses from the standpoint of chemical potential of Oxygen in glass Part 3. Cd(S,Se)" Glass technology Vol 3 No 5 p176 1963
- [52] W G French, J B Mc Chesney, A D Pearson "Glass fibres for optical communications" Annual Review of Materials Science Vol 5 pp 373-394 1975
- [53] B J Ainslie, K J Beales, C R Day, J D Rush "The design and Fabrication of Monomode optical fibre" IEEE Journal of Quantum Electronics Vol QE-18 No 4 1982
- [54] K L Walker, F T Geyling, S R Nagel "Thermopheretic deposition of small particles in the Modified Chemical Vapour Deposition Process" Journal of the American Ceramic Society

[55] K L Walker, J W Harvey, F T Geyling, S R Nagel, "Consolidation of particulate layers in the fabrication of optical fibre preforms" Journal of the American Ceramic Society Vol 63 p96 1980

[56] W D Kingerey, M Berg "Study of the initial stages of sintering solids by viscous flow, evaporation-condensation and self diffusion." Journal of Applied Physics, Vol 26 No 10 p1205 1955

[57] M V Kozlova, V V Kornev, B G Luzhain "Electron microscopic studies of fibre optics preparations during their production" Inorganic Materials (USA) Trans Vol 19 No 2 pp290-294 1983

[58] N J Doran, K J Blow "Cylindrical Bragg fibres, a design and feasibility study for optical communications" Journal of Lightwave Technology Vol LT-1 No 4 p108 1983

[59] F T Geyling, G M Homsey "Extensional instabilities of the glass fibre drawing process" Glass Technology Vol 21 No2 p95 April 1980

[60] U C Paek, R B Runk "Physical behavior of the neck down region during furnace drawing of silica fibres" Journal of Applied Physics Vol 49 No8 pp 4417-4422 August 1978

[61] P J Goodhew, F J Humphries "Electron Microscopy and Analysis" Taylor and Francis 1988 ISBN 0-85066-414-4

[62] G Cliff, G W Lorrimer "Influence of plural electron scattering on X-ray spatial resolution in TEM Thin foil microanalysis" Proc "Quantitative microanalysis with high spatial resolution" Manchester 25-27 March 1981. Sponsored by the metals research committee and EMAG p47 Published by the Metals Society 1981

[63] T A Stephenson, M H Loretto, I P Jones "Beam spreading in thin foils" Proc "Quantitative microanalysis with high spatial resolution" Manchester 25-27 March 1981. Sponsored by the metals research committee and EMAG p53. Published by the Metals Society 1981

[64] Notes from "Analytical Electron Microscopy" a course at Surrey University 26-30 March 1990

[65] P J Goodhew "Thin film preparation for electron microscopy" Elsevier 1985

[66] K Kanaya, K Hojou, K Adachi, K Toki "Ion Bombardment of suitable targets for atomic shadowing for high resolution electron microscopy" Micron Vol 5 pp89-119 1974

[67] D J Barber "Thin films of non-metals made for electron microscopy by sputter etching" Journal of Materials Science Vol 5 pp 1-8 1970

[68] D A Rae, V D Scott, G Love "Errors in thin foil thickness measurements using the contamination spot method" Proc "Quantitative microanalysis with high spatial resolution" Manchester 25-27 March 1981. Sponsored by the metals research committee and EMAG. Published by the Metals Society 1981

[69] P J Goodhew "Preparation of carbon fibres for transmission electron microscopy" Journal of Physics E p392 Vol 4 1971

[70] P V Badami, J C Joiner, G A Jones "Structure of high modulus carbon fibres" Nature Vol 215 p387 1967

[71] M Castle, BSc final year project, Metallurgy and Microstructural Engineering, Sheffield City Polytechnic, 1987.

Table 1 Minimum Detectable Concentrations of Elements in Semiconductor Doped Glasses

Element	Minimum Concentration mol%
Sodium	0.04%
Aluminium	0.09%
Silicon	0.1%
Sulphur	0.05%
Potassium	0.07%
Calcium	0.08%
Zinc	0.08%
Arsenic	0.02%
Selenium	0.04%

Table 2. Minimum Analysis Periods Required to Detect Various Elements

Element	Concentration mol%	Analysis Period
Sodium	2%	5s
Aluminium	1.5%	11s
Sulphur	0.8%	106s
Potassium	5%	3s
Calcium	10%	1.75s
Zinc	30%	0.5s
Arsenic	1%	9s
Selenium	0.3%	28s
Erbium	0.3%	60s
Erbium	1.1%	11s
Germanium	6%	3s
Germanium	35%	1s

Table 3
Parameters of Fibres investigated

Fibre Code	Fibre Type	Draw Temp °C	Draw Speed m/min	Preform Diameter mm	Core Dia. µm	Fibre Dia. µm
5111.01	Raman	1970	152	23	2.2	101
5111.06	Raman	1965	73	"	4.2	152
9695.01.01	Raman				10	119
3126.01.02	Erbium	2000		25	3.5	120
3126.02.02	Erbium	2000		"	3.4	120
3124.01	Erbium	2000		"	3.5	120
3115.01	Erbium	2100		25	7.7	120
3023.02	Erbium	2160	85	27	4.4	79
3023.03	Erbium	2155	47	"	9.0	96
3023.04	Erbium	2120	28	27	14.5	121
2073.01	SC Dpd	1150		10	2.1	70
2073.02	SC Dpd	1150		"	2.0	68
2073.03	SC Dpd	1200		"	3.0	
2074.01	SC Dpd	1200			25	155
2075.04	SC Dpd	1245	38		10	148

Table 4 X-Ray Analysis of Fibre type 3023.02

Livetime 379 seconds				
Element	First Chann	Last Chann	Net Integral	Apparent Concentration mol%
Silicon	1440	1980	723272	91.29%
Erbium	6700	7160	2685	0.34%
Germanium	9840	10160	66351	8.37%

Table 5 X-Ray Analysis of Fibre type 3023.03

Livetime 100 seconds				
Element	First Chann	Last Chann	Net Integral	Apparent Concentration mol%
Silicon	1320	2020	138883	93.03%
Erbium	6680	7220	1643	1.10%
Germanium	9400	10180	8639	5.79%

Table 6 X-Ray Analysis of Fibre type 3023.04

Livetime 500 seconds				
Element	First Chann	Last Chann	Net Integral	Apparent Concentration mol%
Silicon	1440	1980	654759	89.25%
Erbium	6700	7160	7442	1.01%
Germanium	9540	10160	71403	9.73%

Table 7 X-Ray Analysis of Fibre type 3126.01.02

Livetime 892 seconds				
Element	First Chann	Last Chann	Net Integral	Apparent Concentration mol%
Silicon	1540	1900	242410	48.91%
Erbium	6860	7000	54	0.01%
Germanium	9600	10140	253204	51.08%

Table 8 X-Ray Analysis of Fibre type 3126.02.02

Livetime 500 seconds					
Element	First Chann	Last Chann	Gross Integral	Net Integral	Apparent Concentration mol%
Silicon	1440	1940	394289	337505	64.43%
Erbium	6780	7100	10917	80	0.02%
Germanium	9520	10240	205199	186218	35.55%

Table 9 X-Ray Analysis of Fibre type 3124.01

Livetime 531 seconds				
Element	First Chann	Last Chann	Net Integral	Apparent Concentration mol%
Silicon	1440	1980	143433	68.92%
Erbium	6780	7080	0	0.00%
Germanium	9540	10140	64693	31.08%

Livetime 500 seconds				
Element	First Chann	Last Chann	Net Integral	Apparent Concentration mol%
Sodium	900	1120	7526	2.95%
Aluminium	1380	1540	0	0.00%
Silicon	1580	1980	115070	45.11%
Potassium	3160	3460	72378	28.38%
Calcium	3540	3820	491	0.19%
Zinc	8300	9140	58916	23.10%
Arsenic	10340	10740	95	0.04%
Selenium	10980	11400	587	0.23%

Table 11 Chemical Analysis Of Schott RG630 Glass

Element	Concentration Mass percent	Apparent Concentration No Oxygen mol%
Silicon	22%	37%
Zinc	18%	31%
Potassium	17%	29%
Sodium	0.2%	0.34%
Cadmium	0.5-1%	1.7%
Sulphur	0.2%	0.34%
Selenium	0.2%	0.34%

Table 12 X-Ray Analysis of Hoya H640 Filter Glass

Livetime 449 seconds				
Element	First Chann	Last Chann	Net Integral	Apparent Concentration mol%
Sodium	900	1120	9322	0.88%
Aluminium	1380	1540	0	0.00%
Silicon	1580	1980	324472	30.80%
Potassium	3160	3460	212830	20.20%
Calcium	3540	3820	2734	0.26%
Zinc	8300	9140	499700	47.43%
Arsenic	10340	10740	0	0.00%
Selenium	10980	11400	4545	0.43%

Table 13 Chemical Analysis Of Hoya H640 Glass

Element	Concentration Mass percent	Apparent Concentration (No Oxygen) mol%
Silicon	27%	47%
Zinc	11.6%	20%
Potassium	15.7%	27%
Sodium	2.2%	3.8%
Cadmium	0.5-1%	1.7%
Sulphur	0.2%	0.34%
Selenium	0.2%	0.34%

Element	Concentration Mass percent	Apparent Concentration (No Oxygen) mol%
Silicon	32%	52%
Potassium	2%	3.2%
Sodium	21%	34%
Aluminium	2.6%	4.2%
Calcium	3.7%	6.0%
Barium	0.31%	0.5%

Table 15 X-ray Analysis of Fibre Type 2073.01 Core Glass

Livetime 500 seconds					
Element	First Chann	Last Chann	Gross Integral	Net Integral	Apparent Concentration mol%
Sodium	900	1120	10587	2187	0.80%
Aluminium	1380	1540	20354	0	0.00%
Silicon	1580	1980	247190	141823	52.16%
Sulphur	2220	2380	6284	61	0.02%
Potassium	3160	3460	30725	6245	2.30%
Calcium	3540	3820	40112	11237	4.13%
Zinc	8320	8860	145737	108889	40.05%
Arsenic	10340	10740	8290	688	0.25%
Selenium	10980	11400	7315	781	0.29%

Livetime 219 seconds					
Element	First Chann	Last Chann	Gross Integral	Net Integral	Apparent Concentration mol%
Sodium	900	1120	20327	9797	1.43%
Aluminium	1380	1540	18361	46	0.01%
Silicon	1580	1980	482766	419724	61.37%
Sulphur	2220	2380	11416	544	0.08%
Potassium	3160	3460	50083	21387	3.13%
Calcium	3540	3820	60345	30833	4.51%
Zinc	8320	8860	228606	198604	29.04%
Arsenic	10340	10740	13084	1062	0.16%
Selenium	10980	11400	11914	1948	0.28%

Table 17 X-Ray Analysis of Fibre type 2073.03 Cladding Glass

Livetime 185 seconds					
Element	First Chann	Last Chann	Gross Integral	Net Integral	Apparent Concentration mol%
Sodium	900	1120	23099	11237	1.96%
Aluminium	1380	1540	41913	8568	1.50%
Silicon	1580	1980	523125	450665	78.79%
Sulphur	2220	2380	9231	398	0.07%
Potassium	3160	3460	55917	29285	5.12%
Calcium	3540	3820	92499	58344	10.20%
Zinc	8320	8860	25278	7848	1.37%
Arsenic	10340	10740	14613	5625	0.98%
Selenium	10980	11400	7240	0	0.00%

Table 18 X-Ray Analysis of Pure Zinc

Livetime 322 seconds					
Element	First Chann	Last Chann	Gross Integral	Net Integral	Apparent Concentration
Zinc La	760	1220	9446	6254	--
Zinc Ka	8260	9000	838367	781994	--

Table 19 X-Ray Analysis of 2075.04 Untreated Fibre Core

Livetime 100 seconds				
Element	First Chann	Last Chann	Net Integral	Apparent Concentration mol%
Silicon	1240	2020	60576	33.66%
Potassium	3060	3440	3487	6.22%
Calcium	3500	3880	5366	2.07%
Barium	4260	4620	1240	1.34%
Zinc	8300	8920	79768	55.95%
Arsenic	10240	10680	299	0.23%
Selenium	10980	11400	994	0.77%

Livetime 100 seconds				
Element	First Chann	Last Chann	Net Integral	Apparent Concentration mol%
Silicon	1240	2020	60576	39.56%
Sulphur	2200	2500	210	0.14%
Potassium	3060	3440	3487	2.28%
Calcium	3500	3880	5366	3.50%
Barium	4260	4620	1240	0.81%
Zinc	8300	8920	79768	52.09%
Arsenic	10240	10680	299	0.98%
Selenium	10980	11400	994	0.65%

Table 21 X-Ray Analysis of 2075.04 Fibre Core Heat treated at 530°C for 18 hours

Livetime 100 seconds				
Element	First Chann	Last Chann	Net Integral	Apparent Concentration mol%
Silicon	1240	2020	60576	46.53%
Sulphur	2200	2500	210	0.22%
Potassium	3060	3440	3487	2.71%
Calcium	3500	3880	5366	3.87%
Barium	4260	4620	1240	0.65%
Zinc	8300	8920	79768	45.56%
Arsenic	10240	10680	299	0.00%
Selenium	10980	11400	994	0.46%

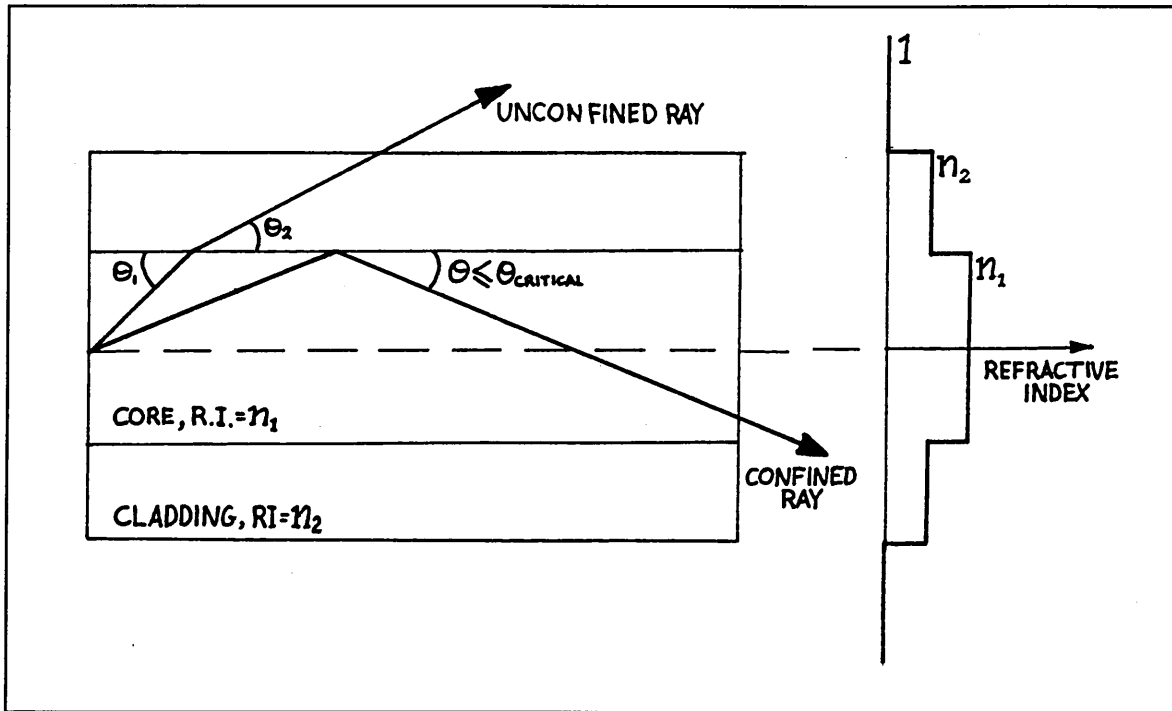


Figure 1. Schematic diagram of a typical multimode fibre.

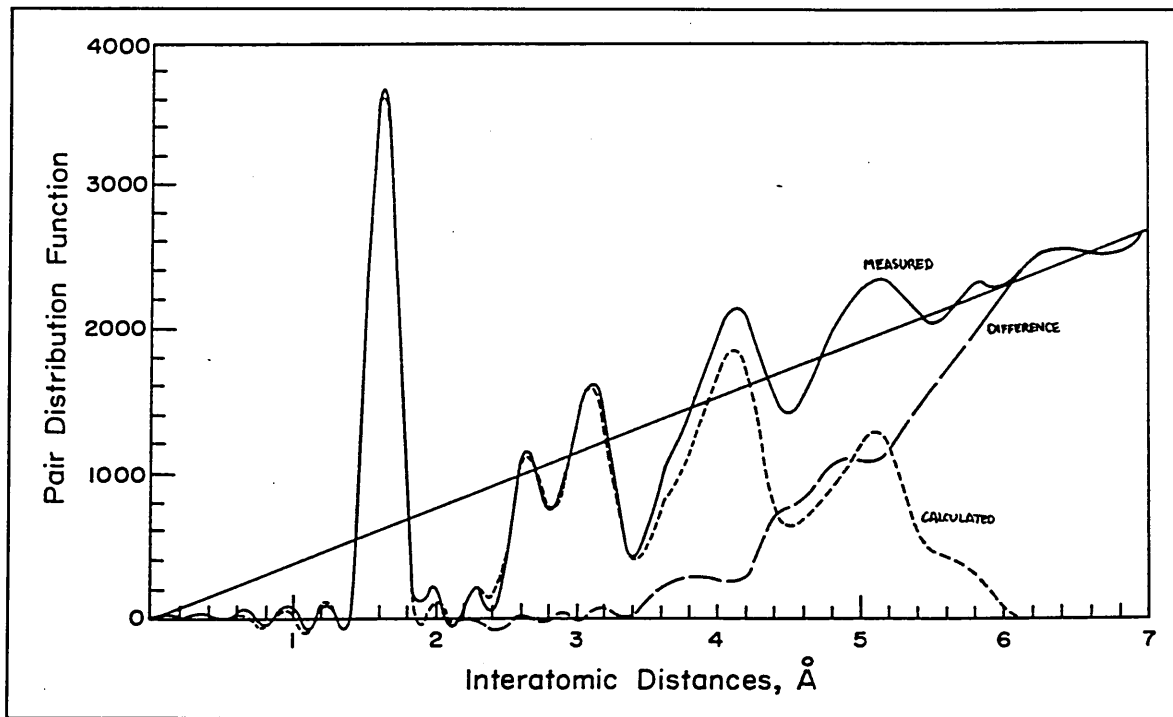


Figure 2. Pair distribution function for amorphous silica after Mozzi & Warren [9]

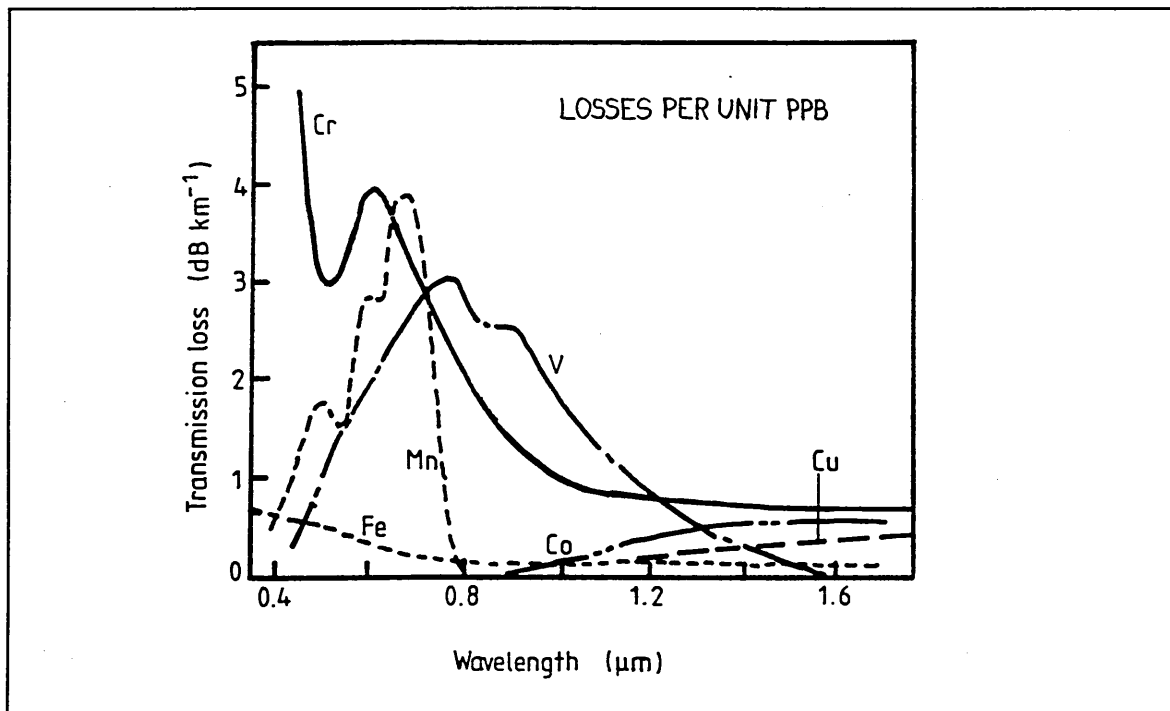


Figure 3. Absorption losses due to transition metal ions after Katsuyama & Matsumura [22]

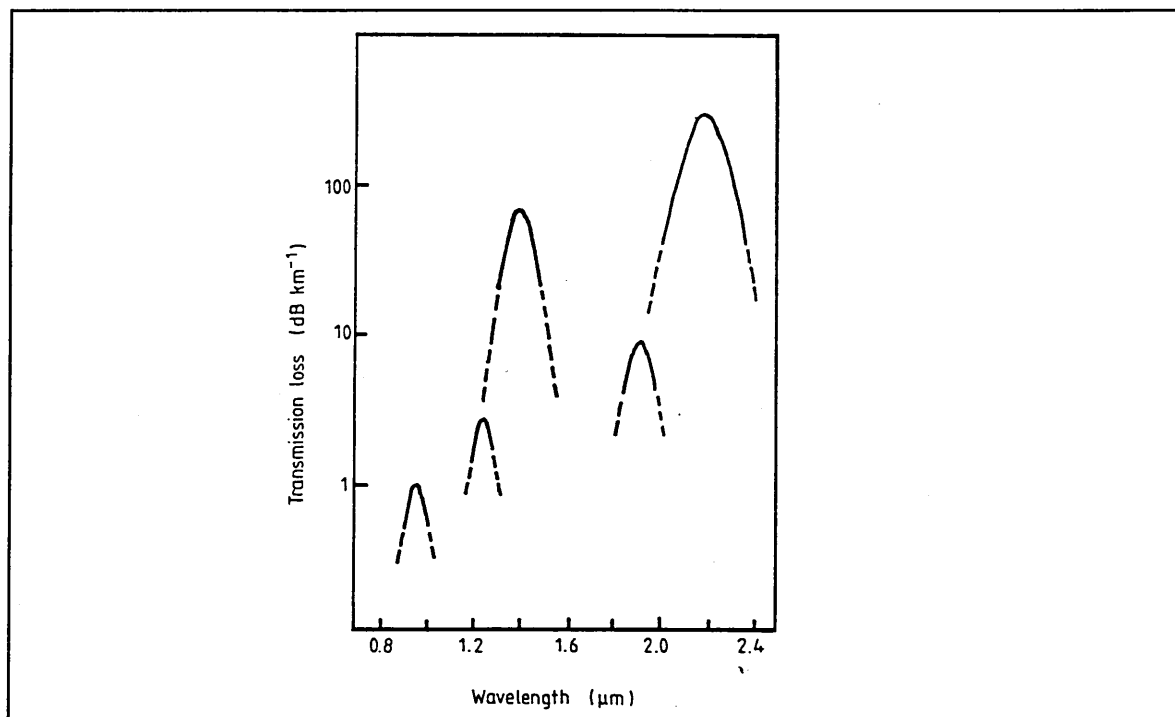


Figure 4. Absorption losses due to water. (After [22])

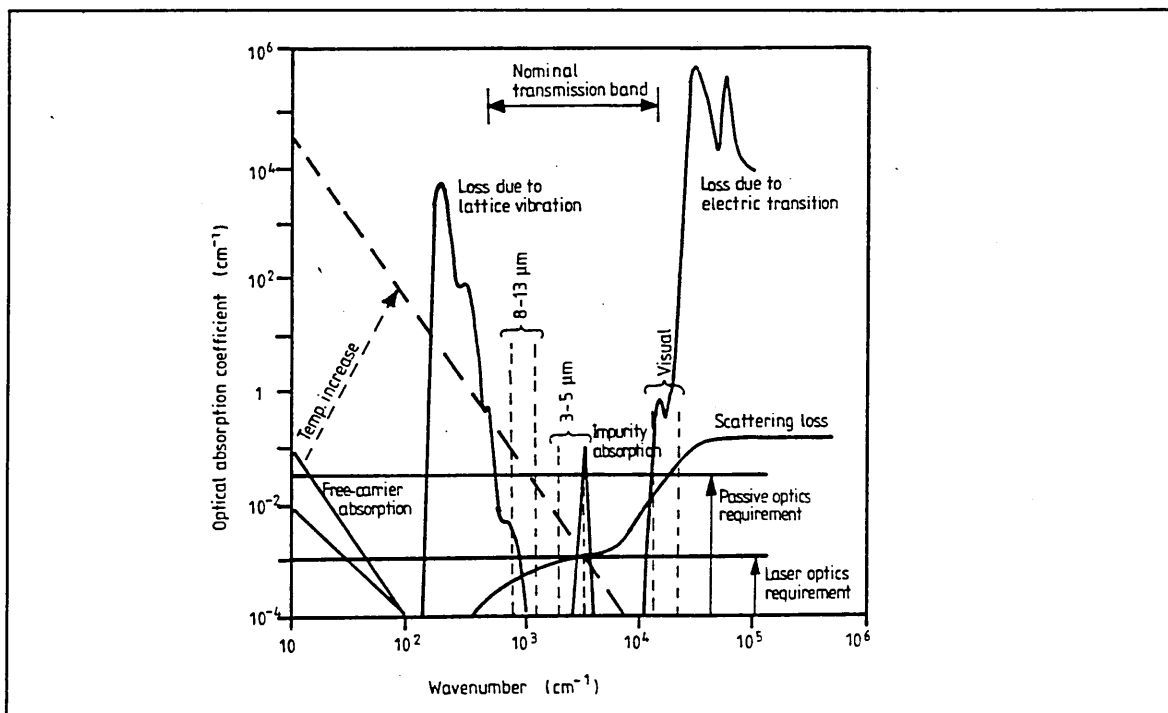


Figure 5. Total absorption losses in silica-based optical fibres, after [22]

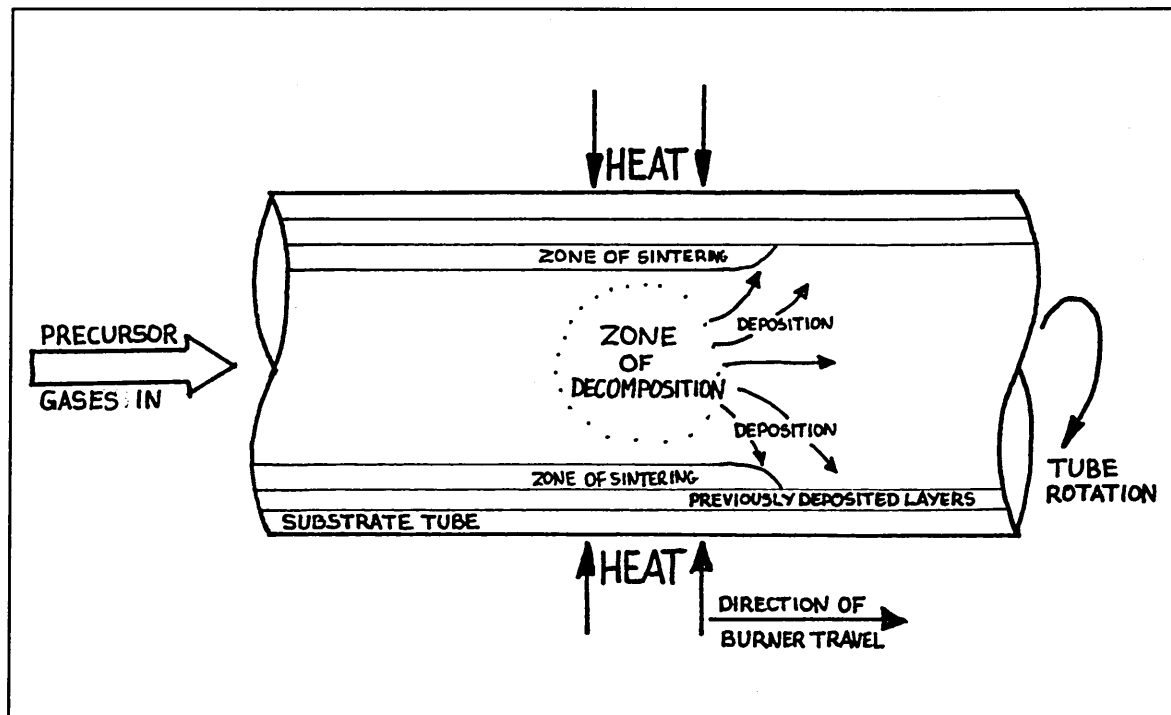


Figure 6. Schematic diagram of the Modified Chemical Vapour Deposition (MCVD) process.

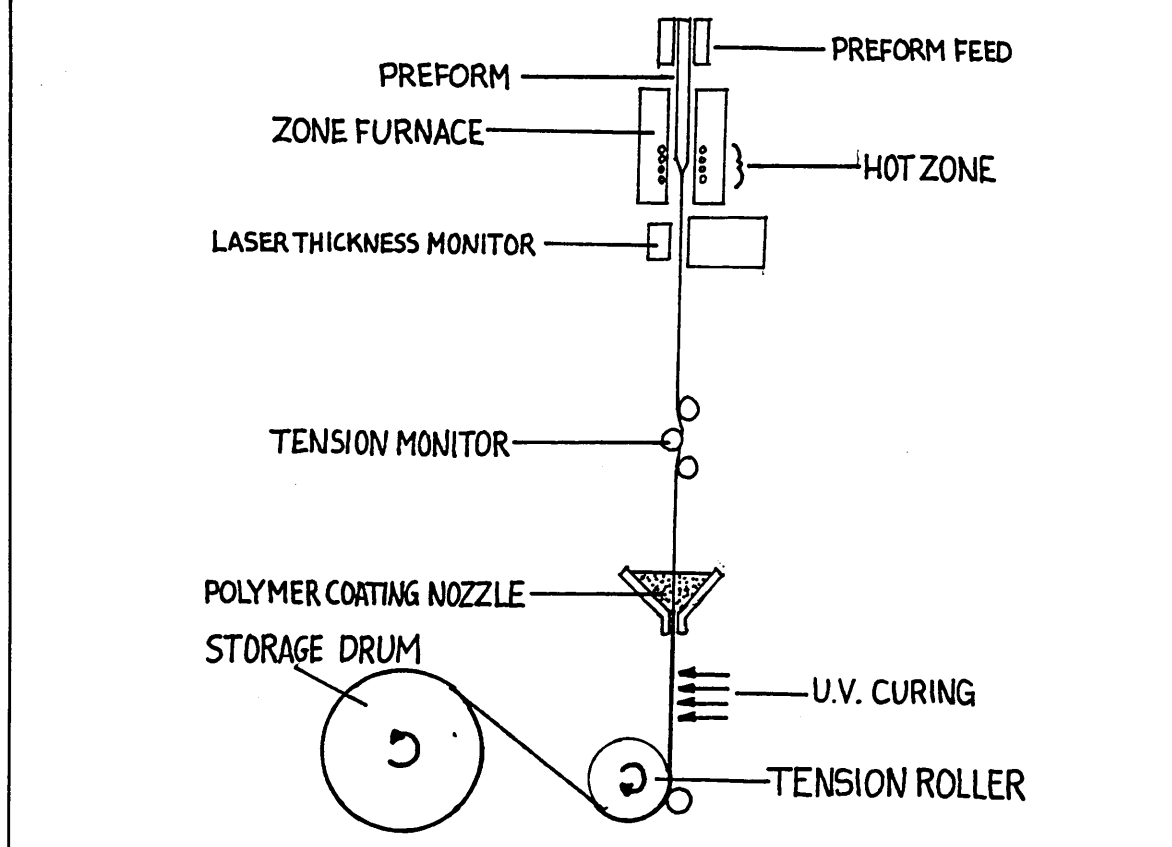


Figure 7. Schematic drawing of a fibre drawing column.

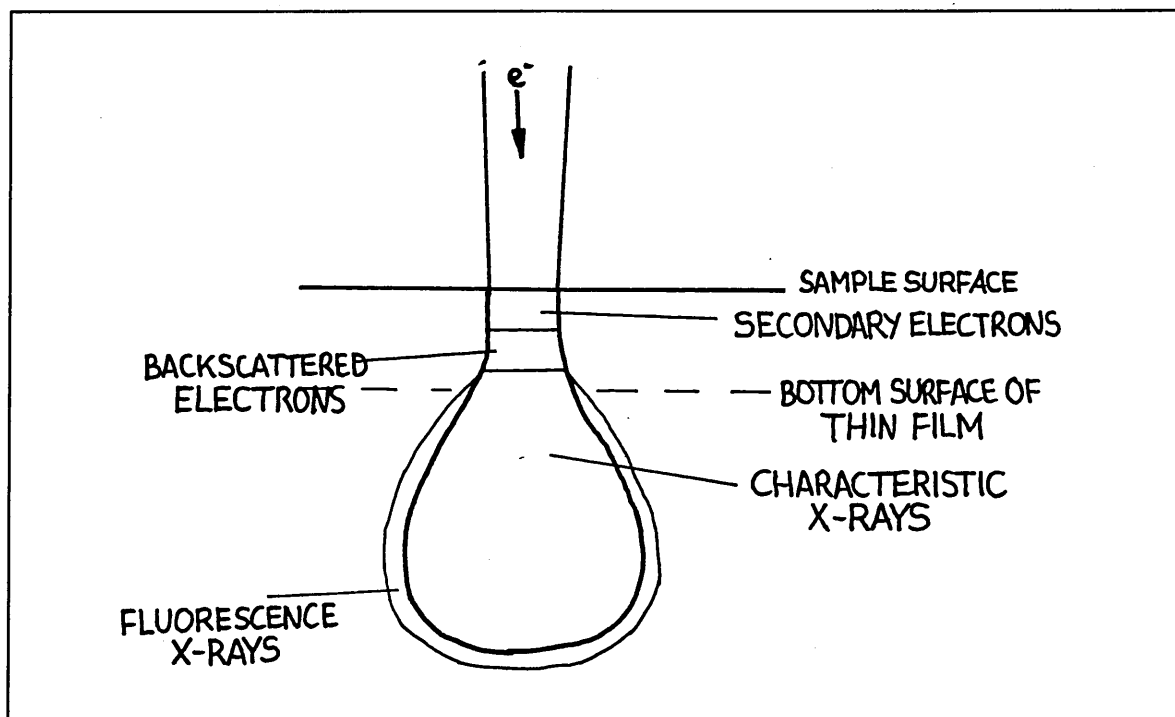


Figure 8. Interaction volumes for the most important processes in a bulk sample.

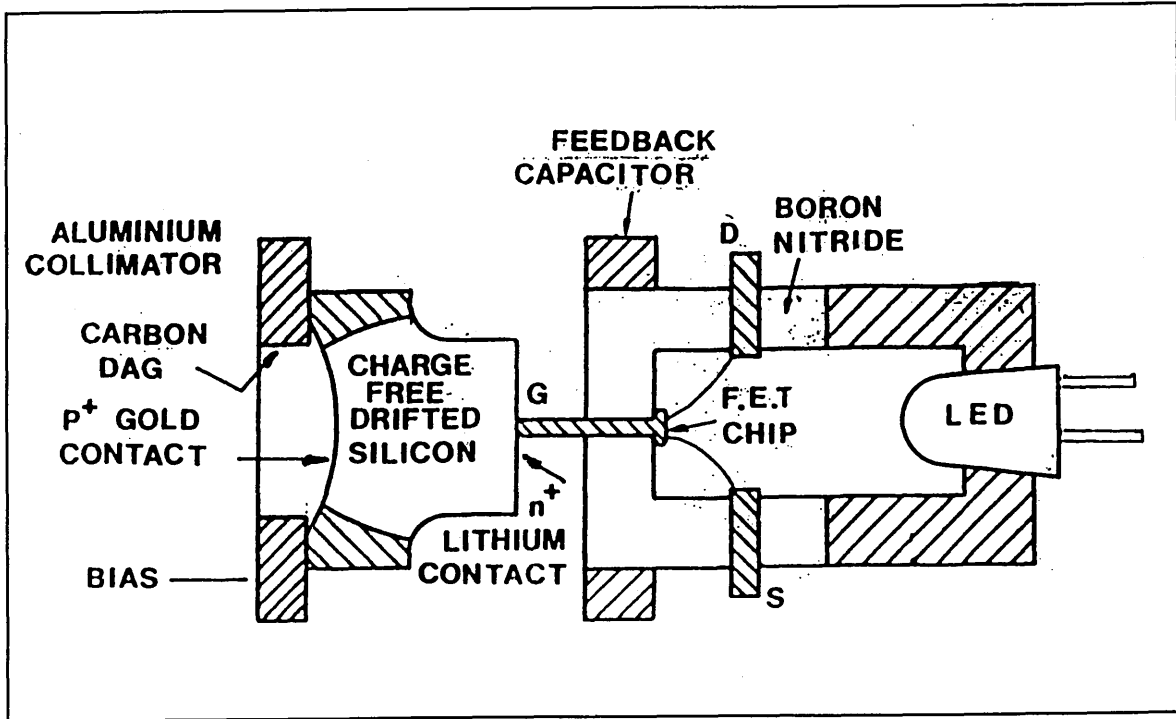


Figure 9. Schematic drawing of a solid-state X-ray detector.

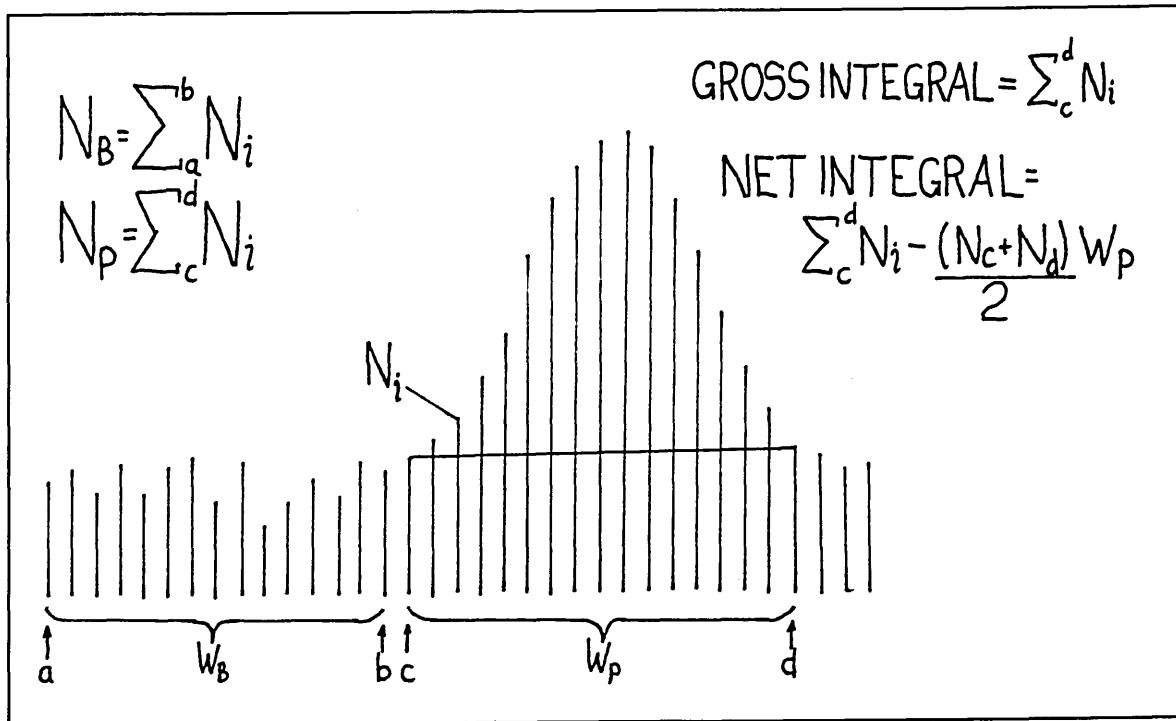


Figure 10. Section of hypothetical X-ray spectrum.

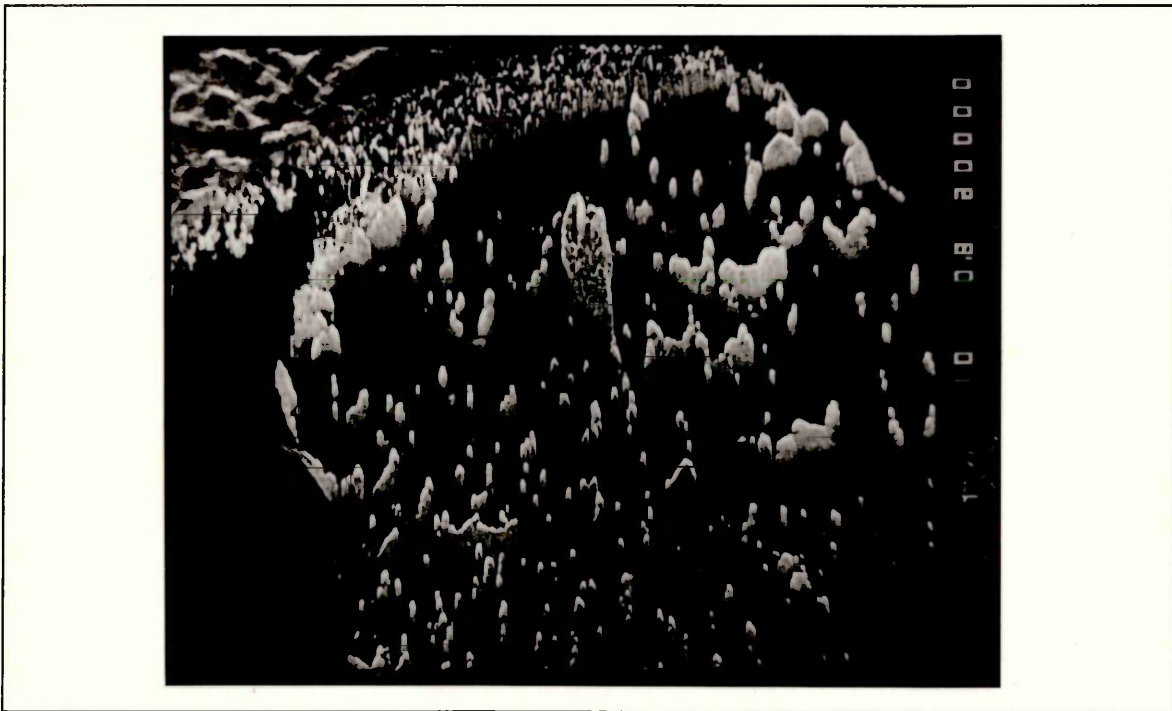


Figure 11. Micrograph of ion-beam damaged surface of an optical fibre sample due to lack of sample rotation.

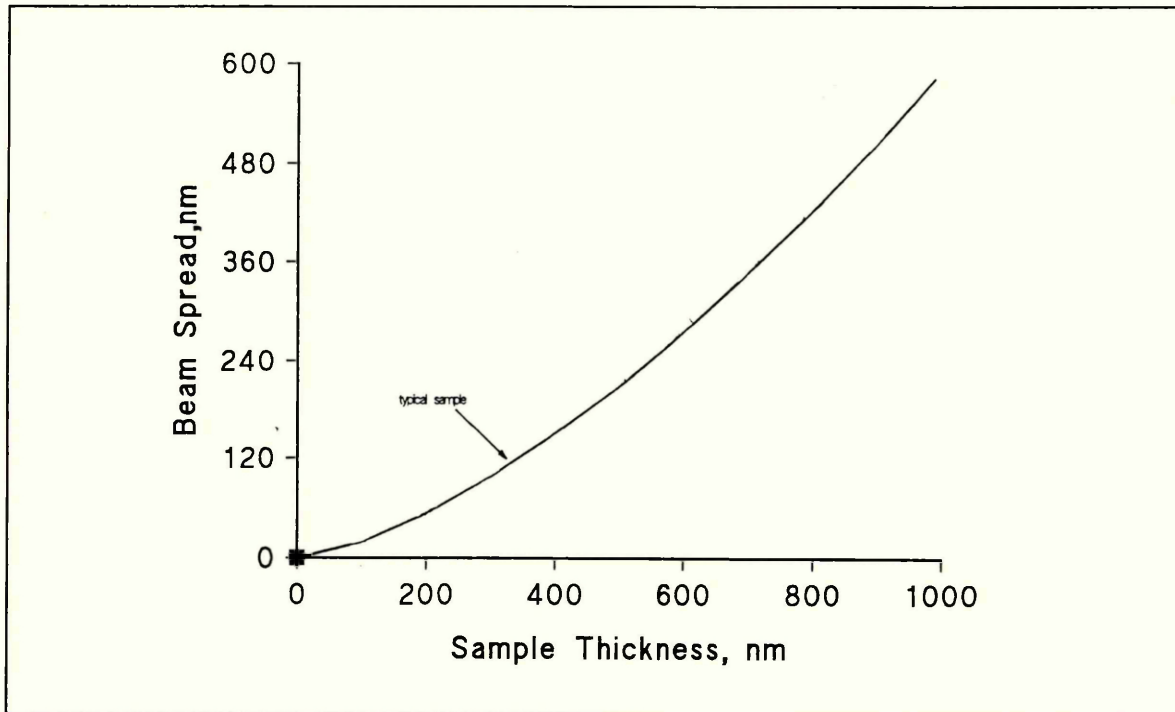


Figure 12. Graph of electron beam spread against sample thickness for silica glass.

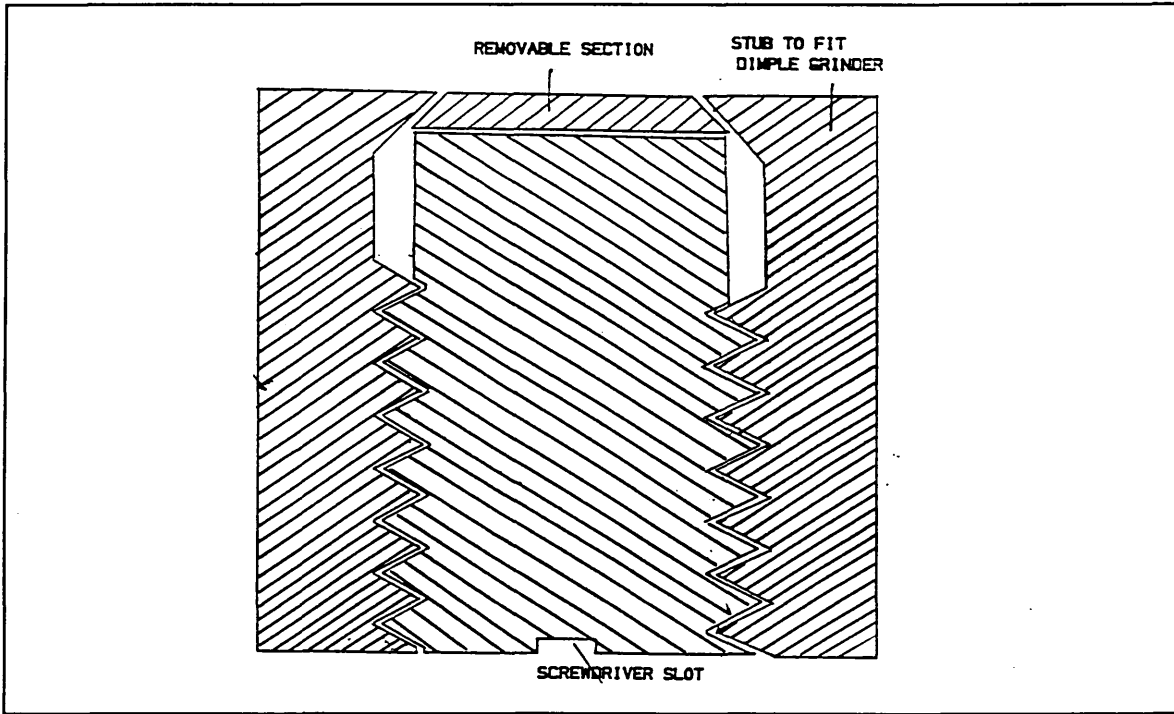


Figure 13. Dimpling stub manufactured for this project.

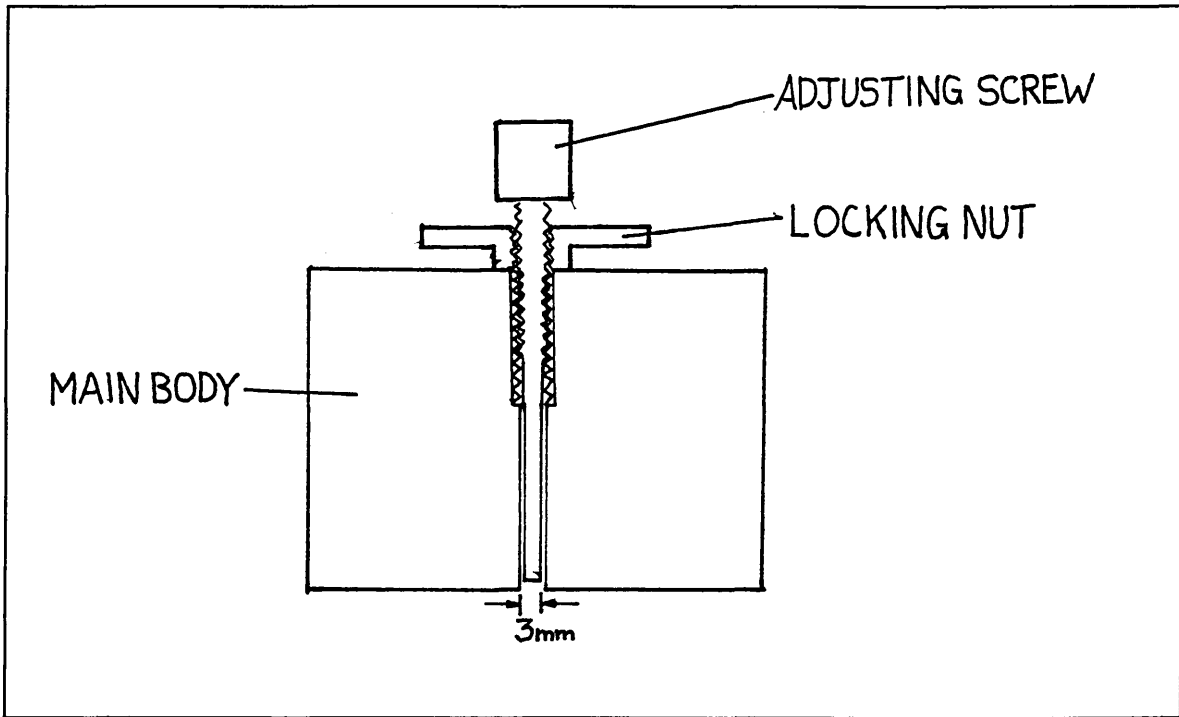


Figure 14. Roughing block for manually thinning samples.

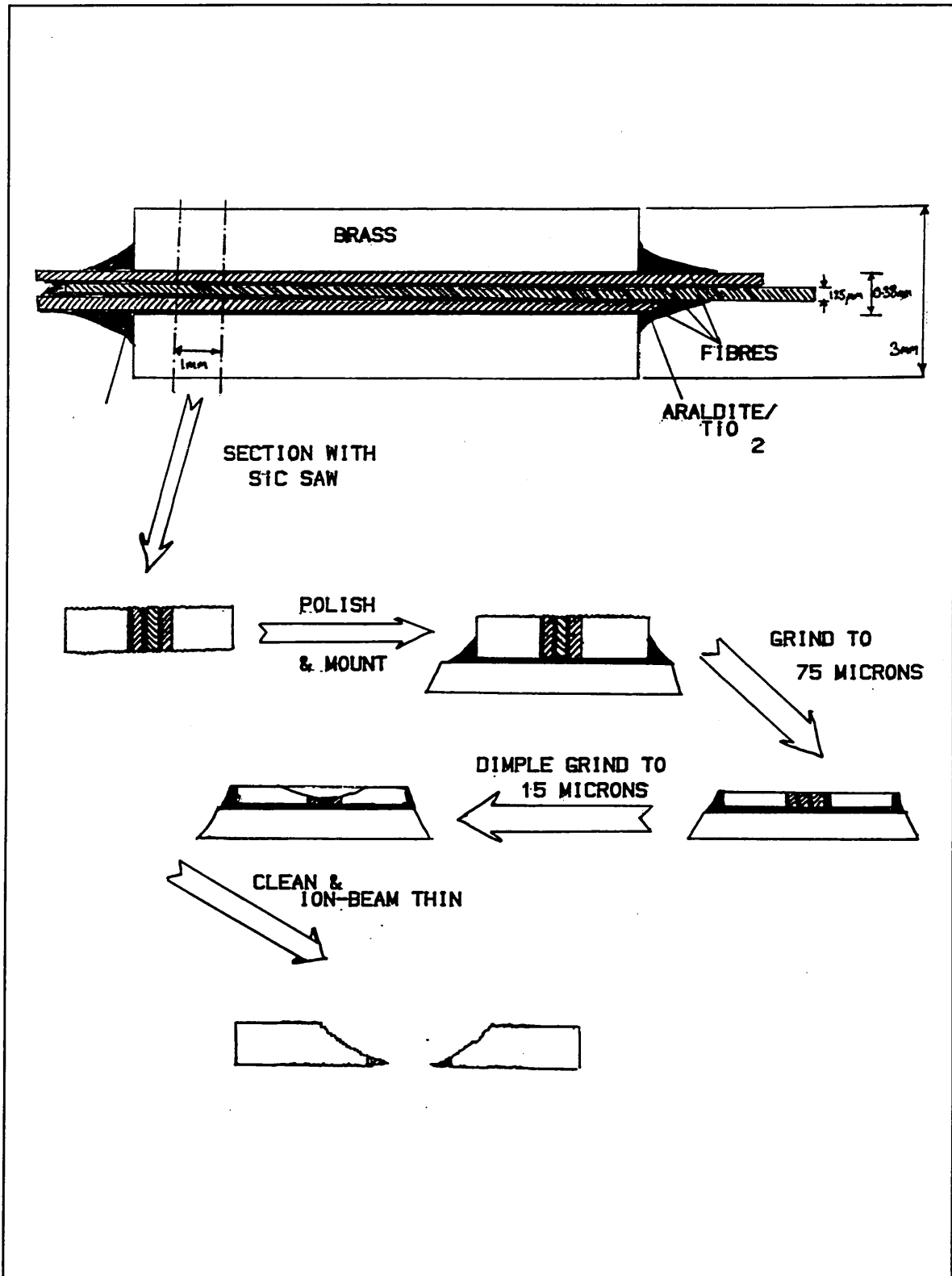


Figure 15. Various stages in the preparation of a sample.

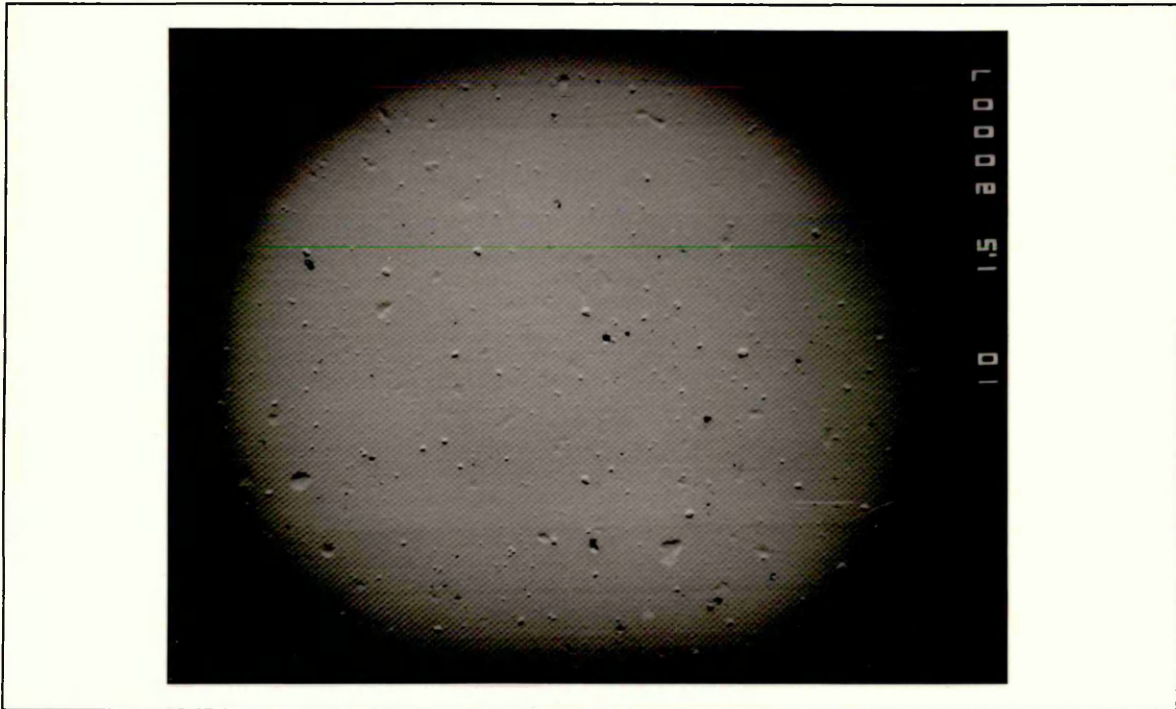


Figure 16. Calibration Specimen x1500

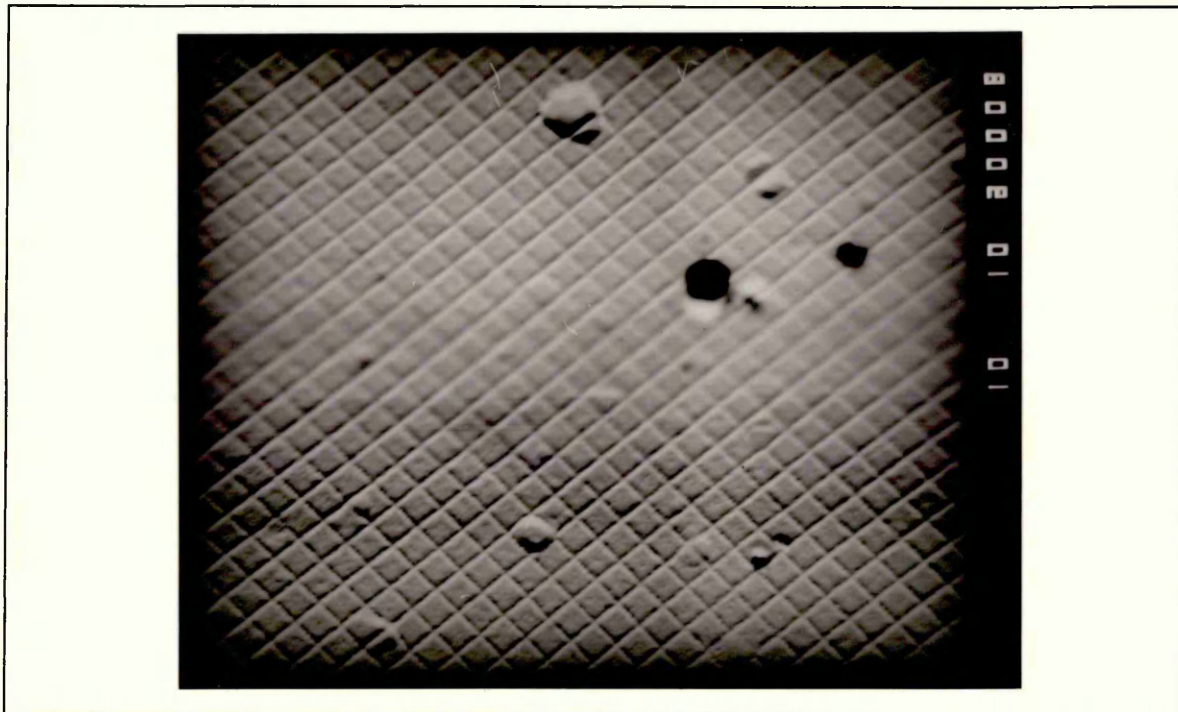


Figure 17 Calibration Specimen x10000

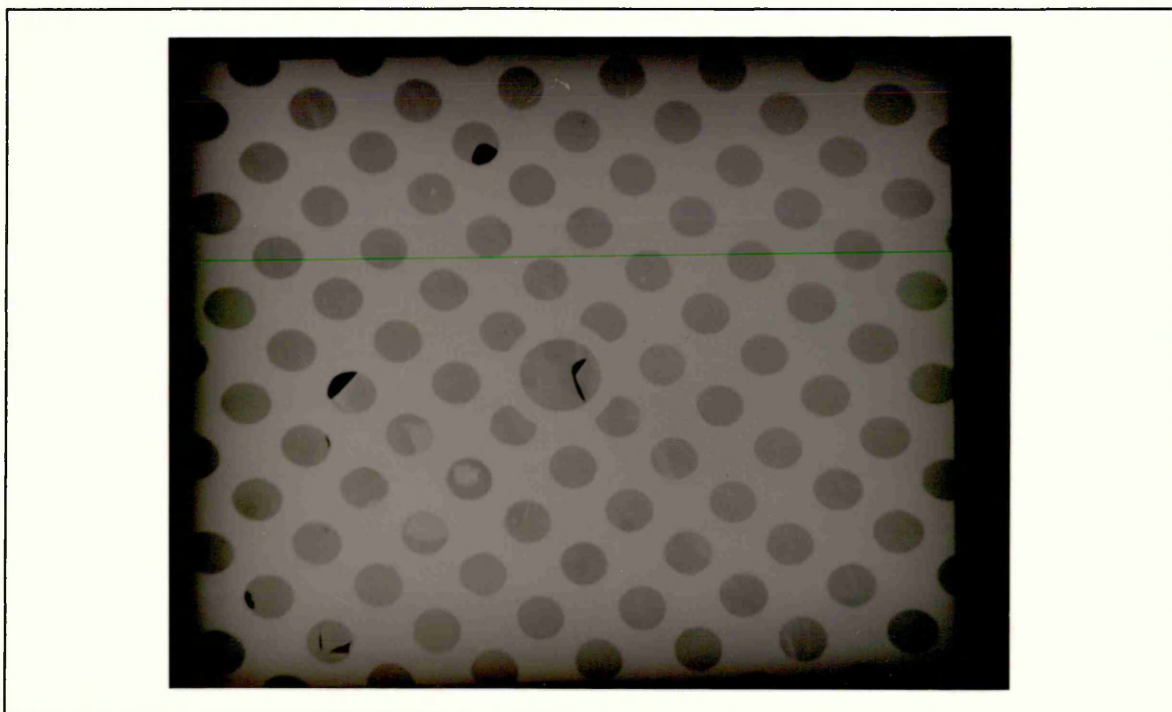


Figure 18. Calibration Specimen x100

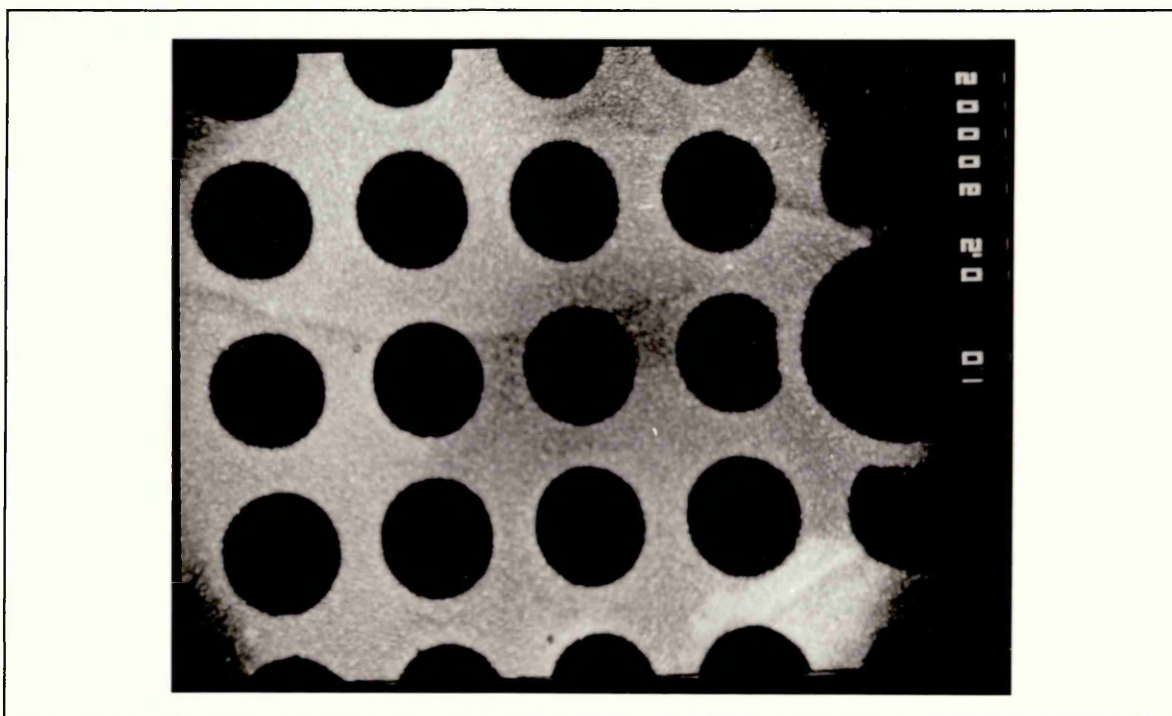


Figure 19. Calibration Specimen x200

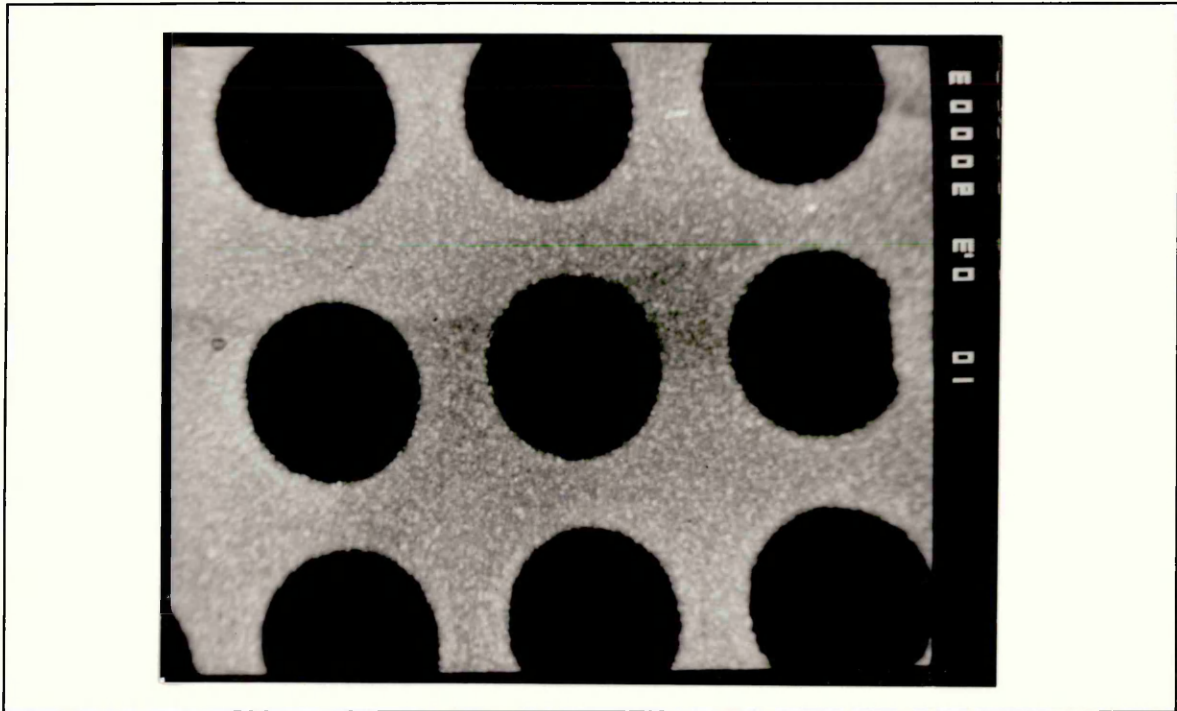


Figure 20. Calibration Specimen x300

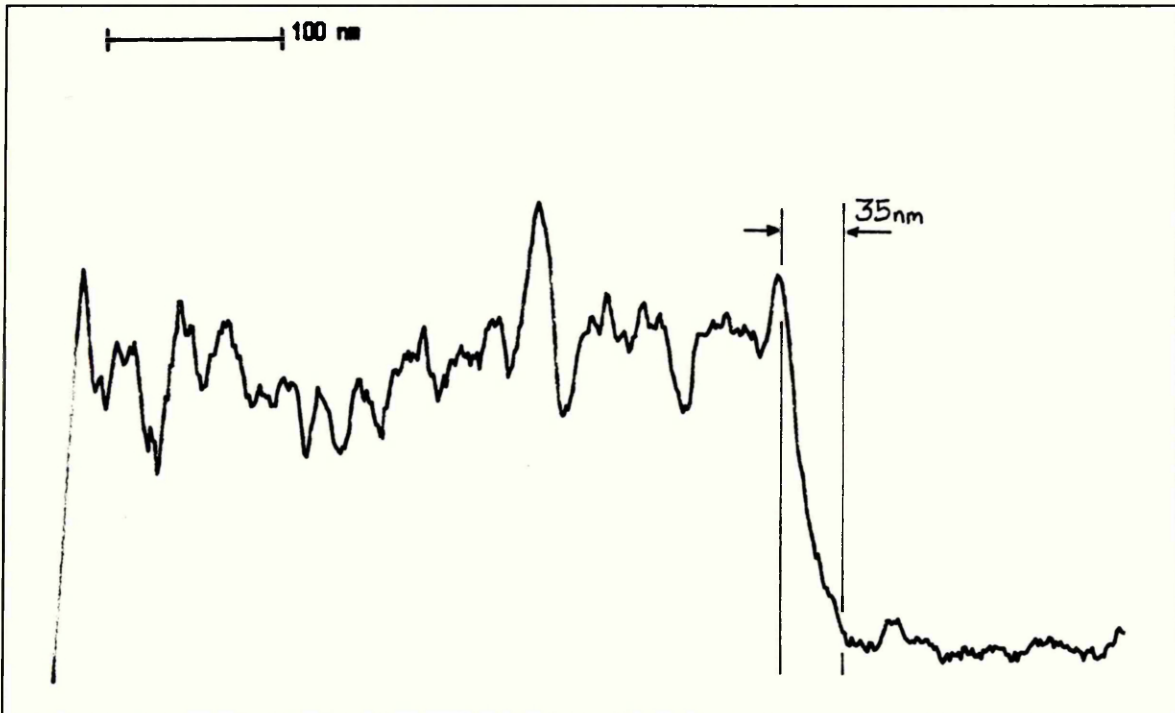


Figure 21. X-ray linescan of a platinised carbon film.

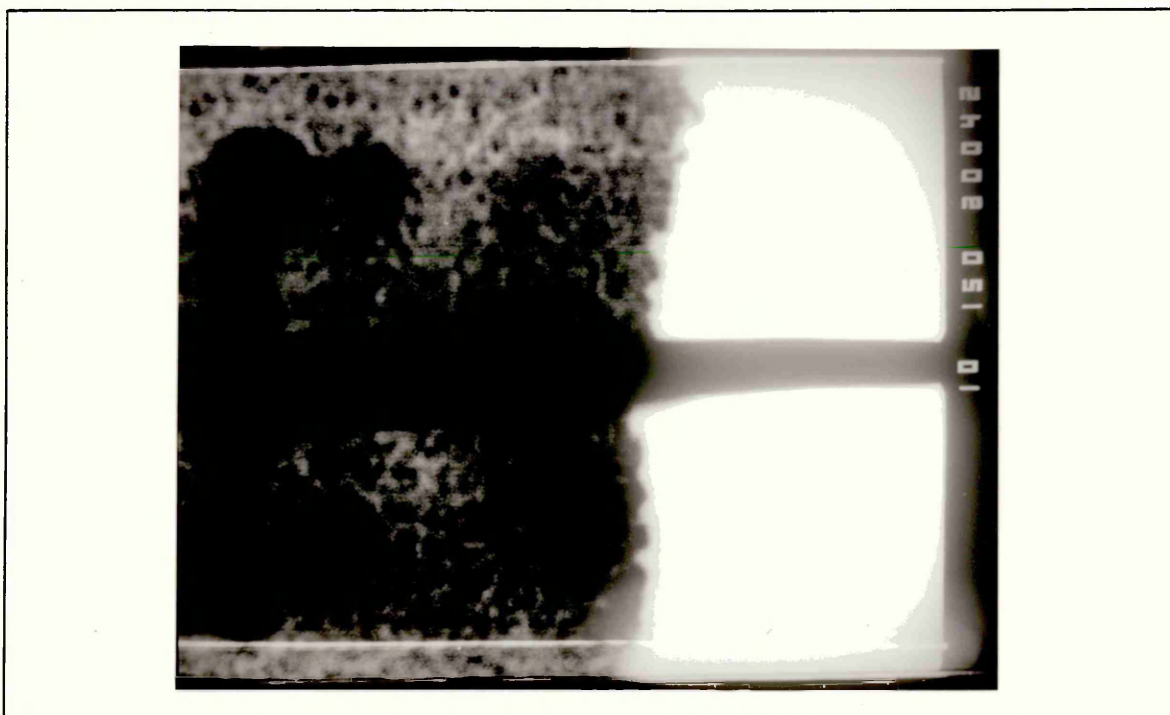


Figure 22. Micrograph of platinised carbon film x150,000

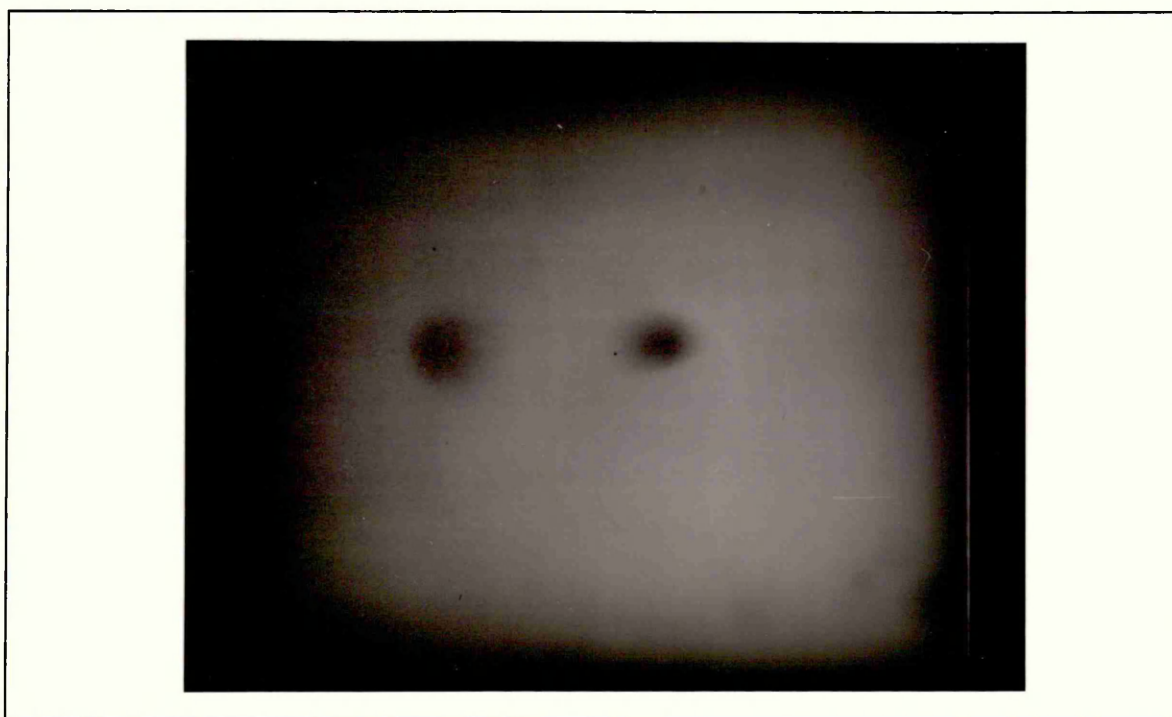


Figure 23. Contamination spots on fibre 9695.01.01. x100,000



Figure 24. Contamination spots on fibre type 5111.01. x200,000

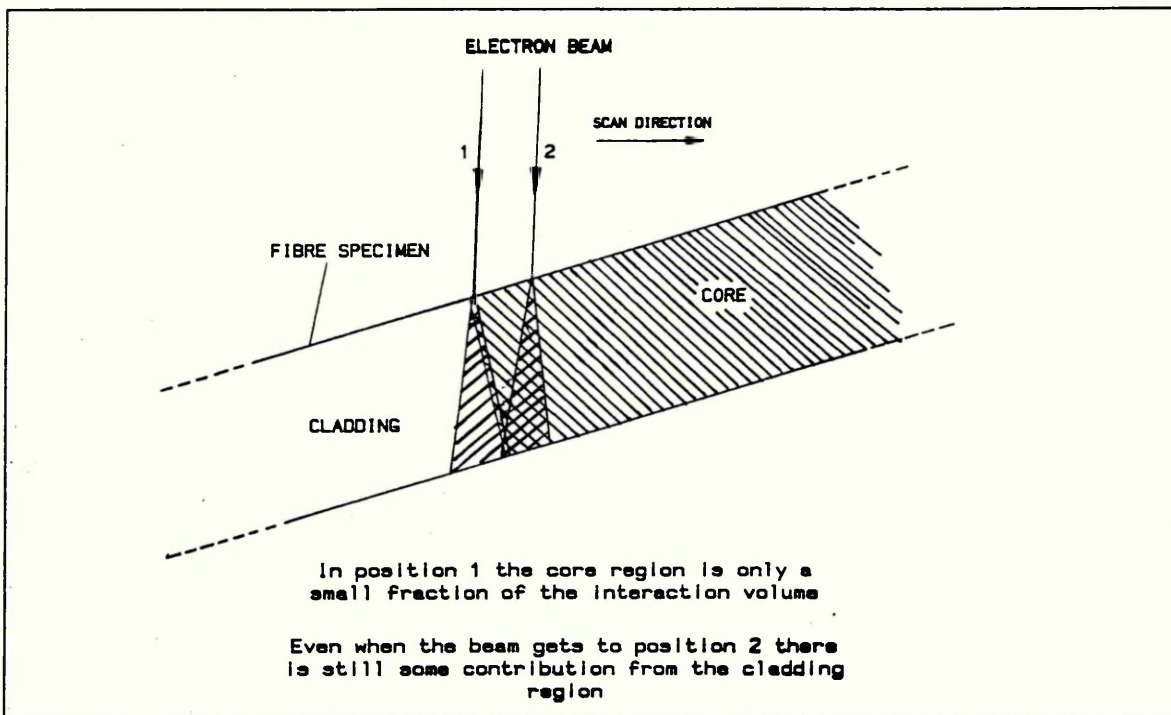


Figure 25. Diagram of the interaction of an electron beam with a tilted sample.

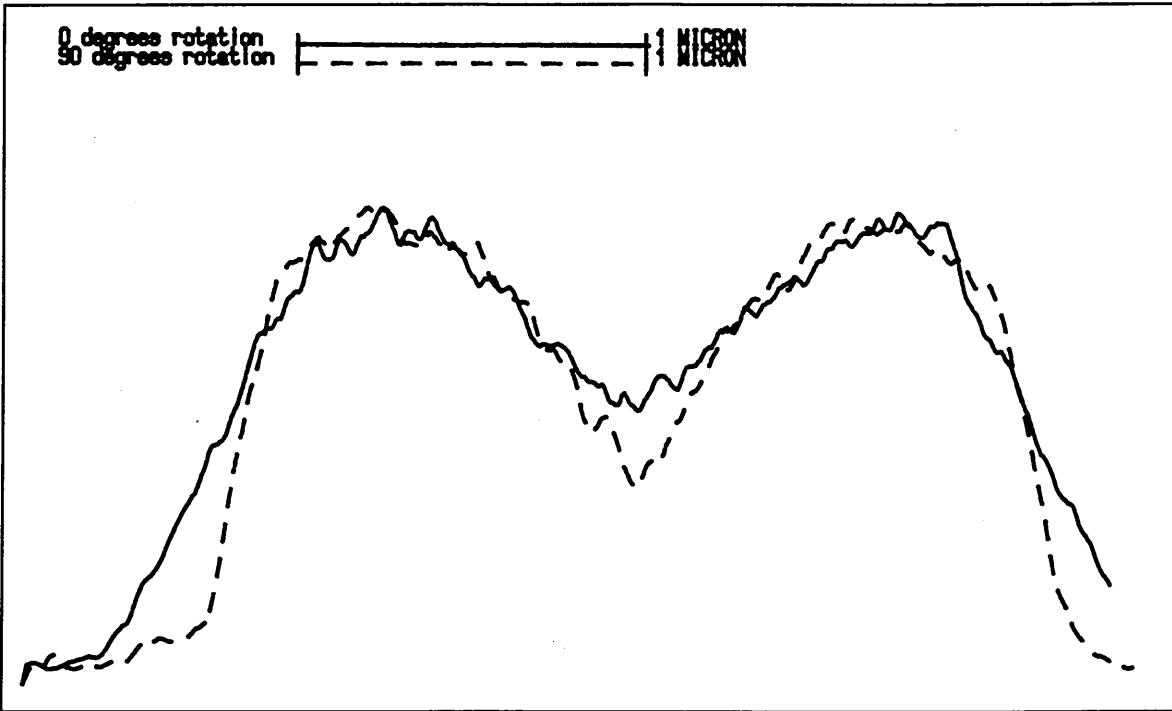


Figure 26. Pair of orthogonal germanium linescans from fibre type 5111.01

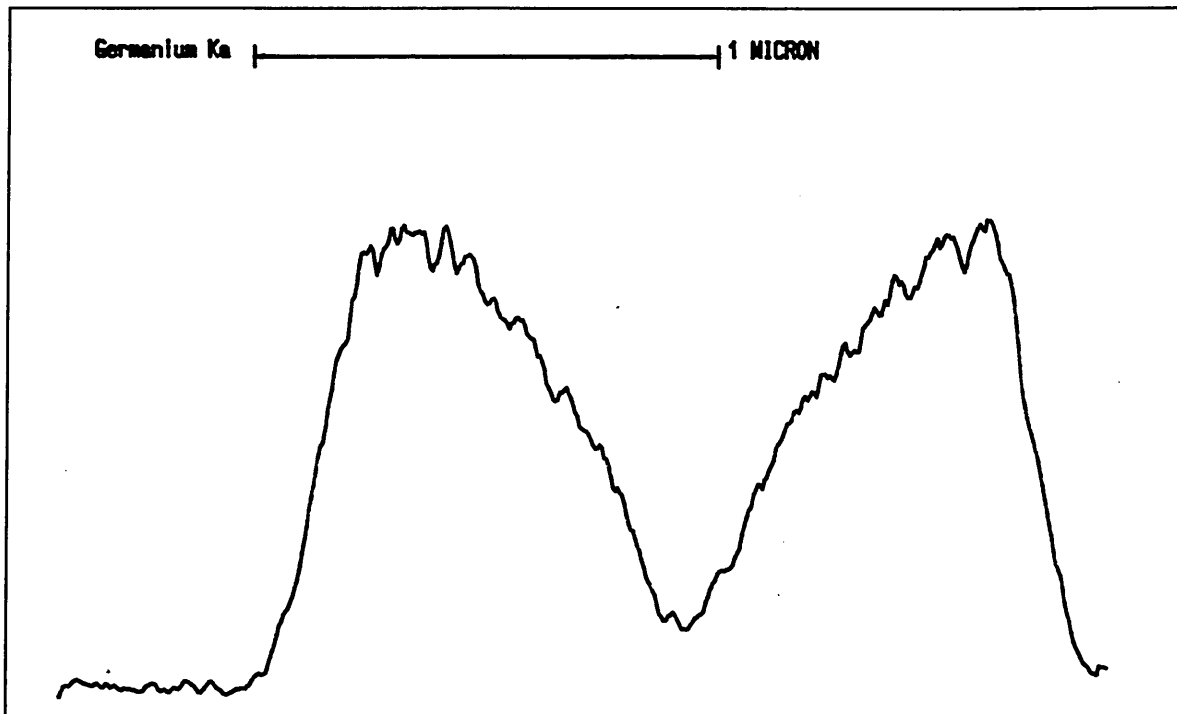


Figure 27. Germanium Linescan. Fibre type 5111.01

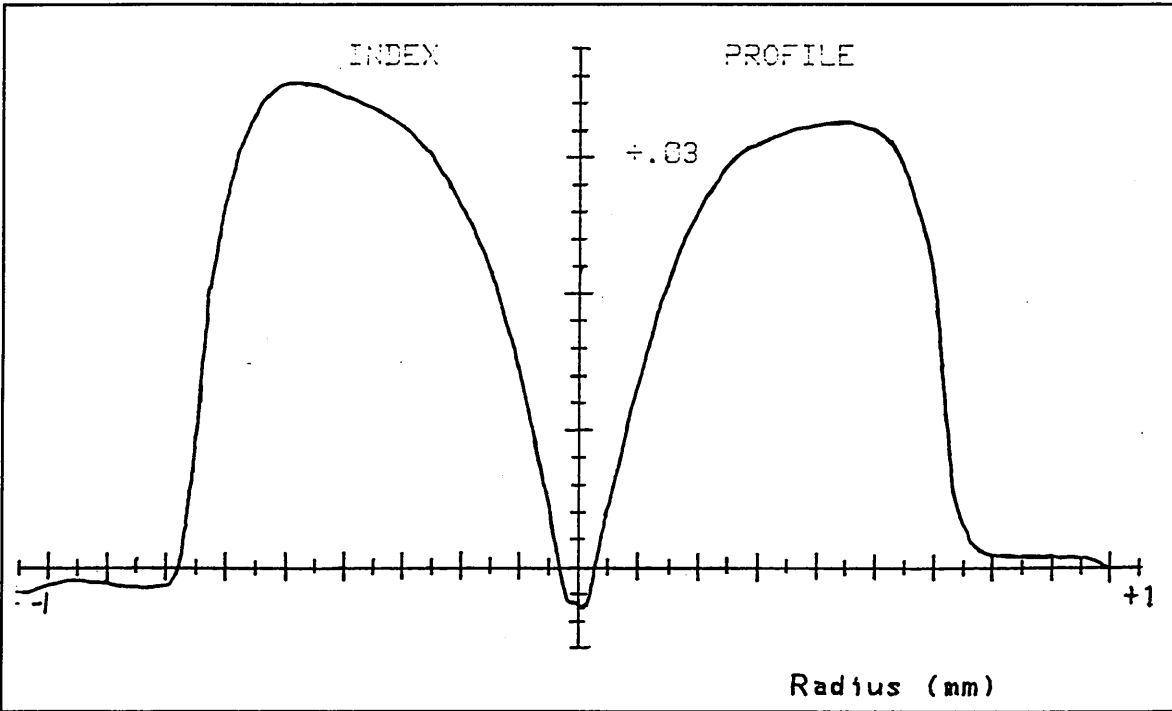


Figure 28. Preform Refractive index profile for the 5111 preform. (Courtesy of BTRL)

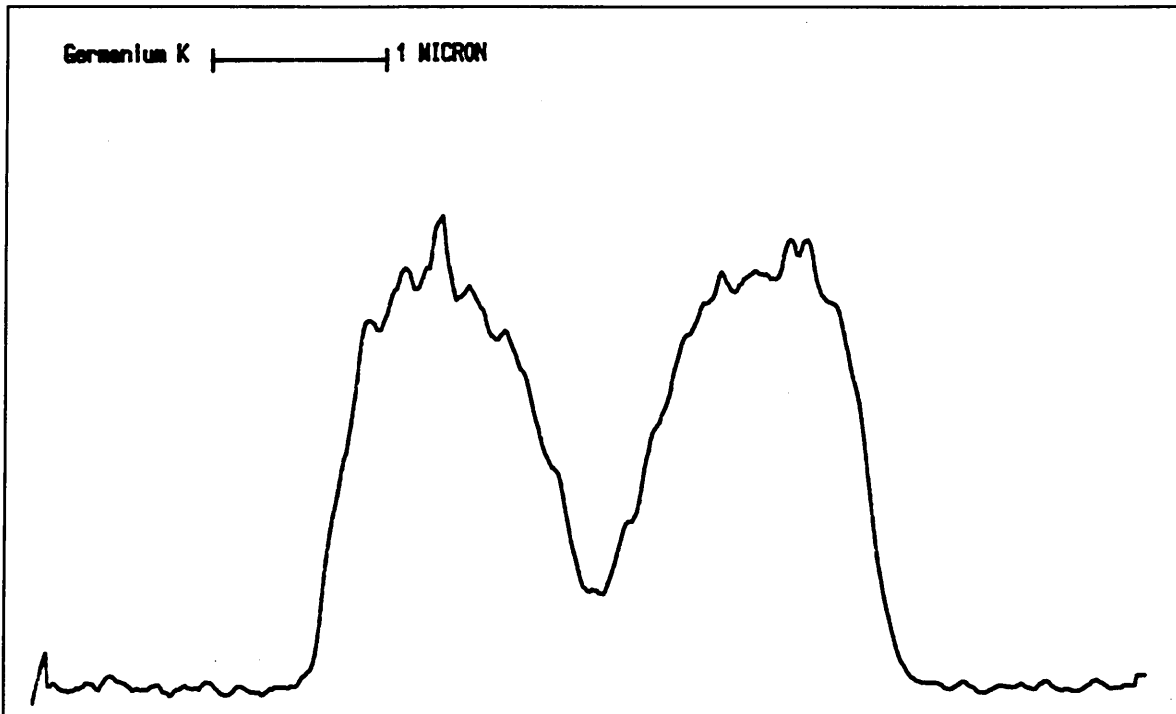


Figure 29. Germanium linescan for fibre type 5111.06.

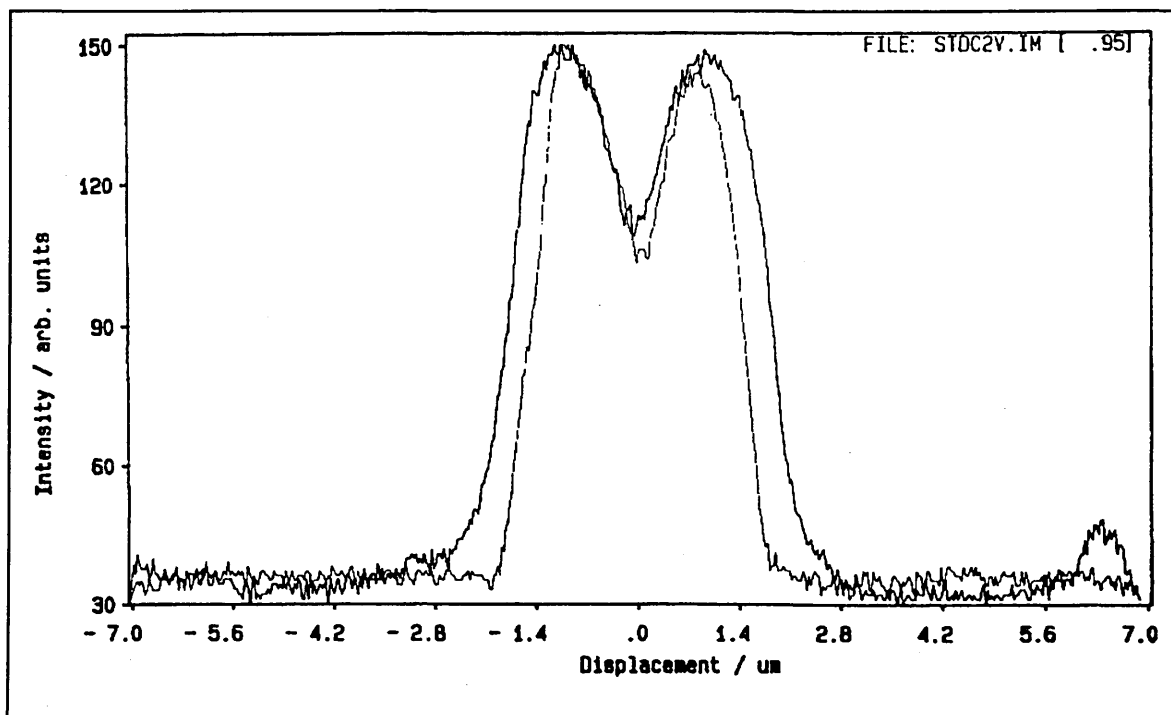


Figure 30. Backscattered electron intensity plot for fibre type 5111.06. (Courtesy of BTRL)

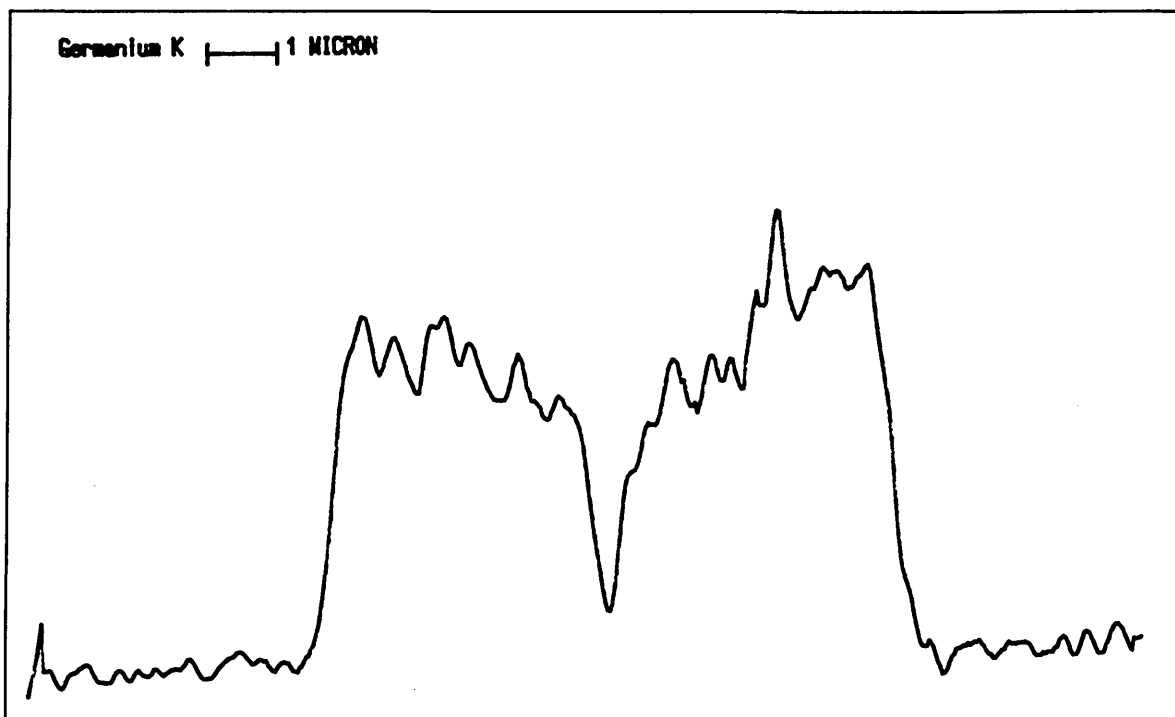


Figure 31. Germanium Linescan. Fibre type 9695.01.01

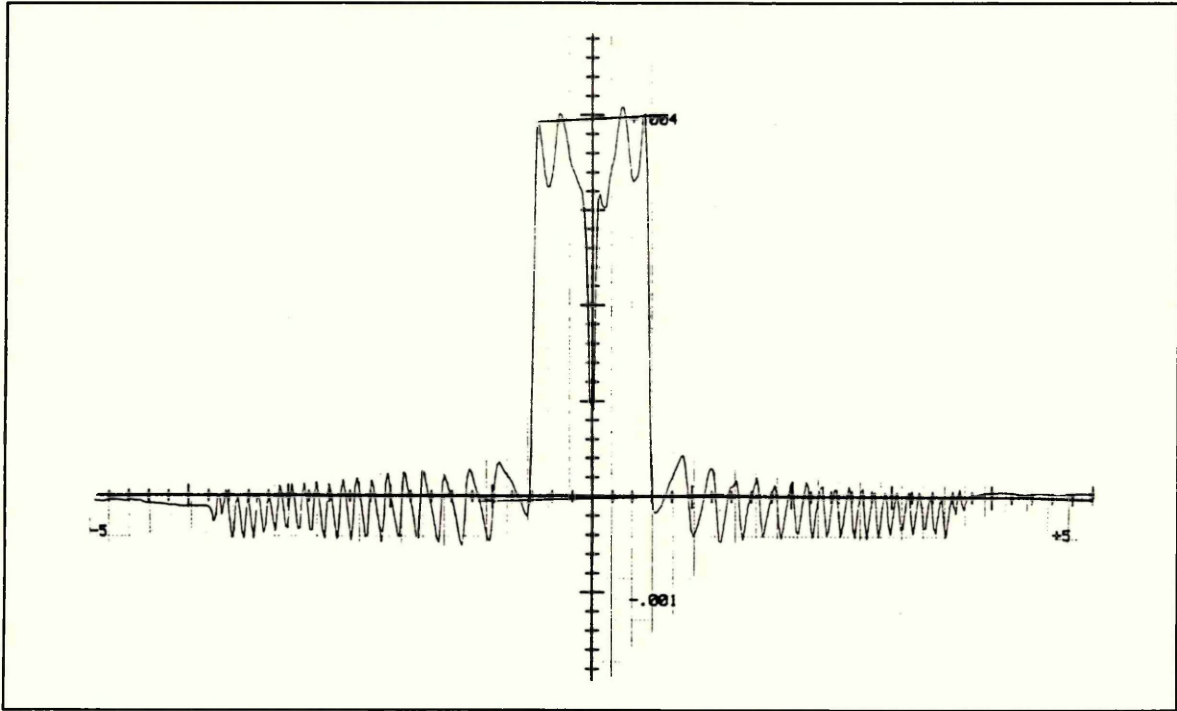


Figure 32. Preform refractive index profile. 9695 preform.
(Courtesy of BTRL)

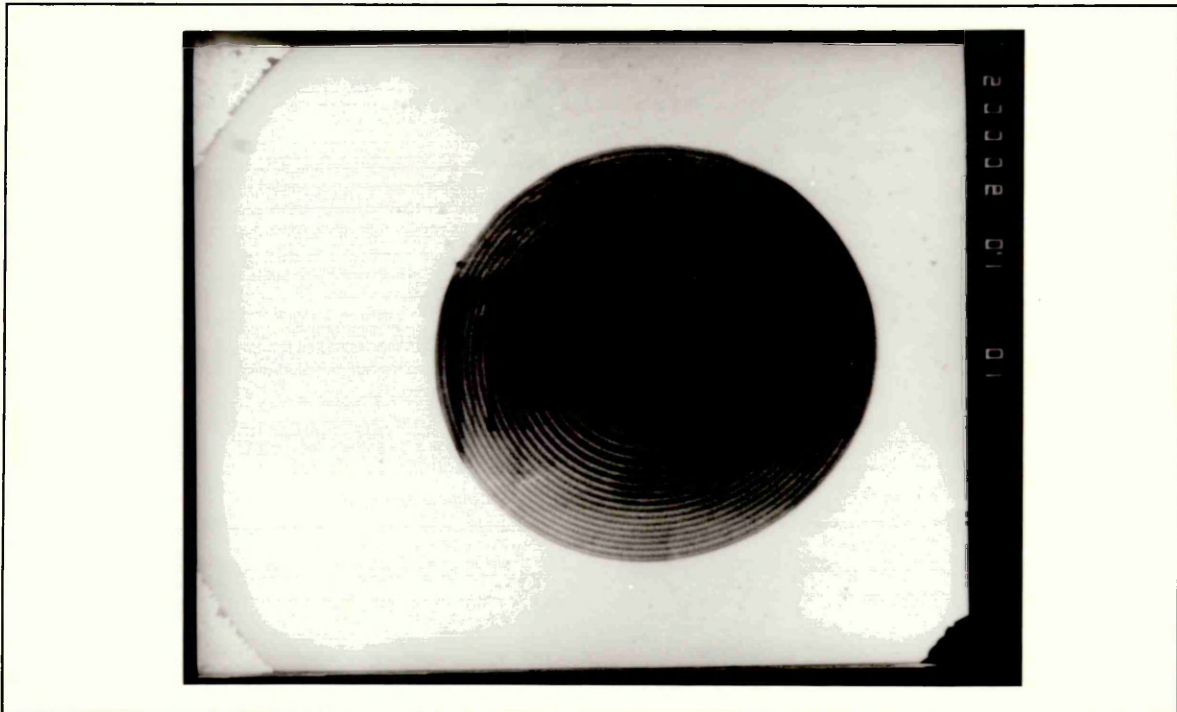


Figure 33. Fibre type 9695.01.01. x1000. SEI.

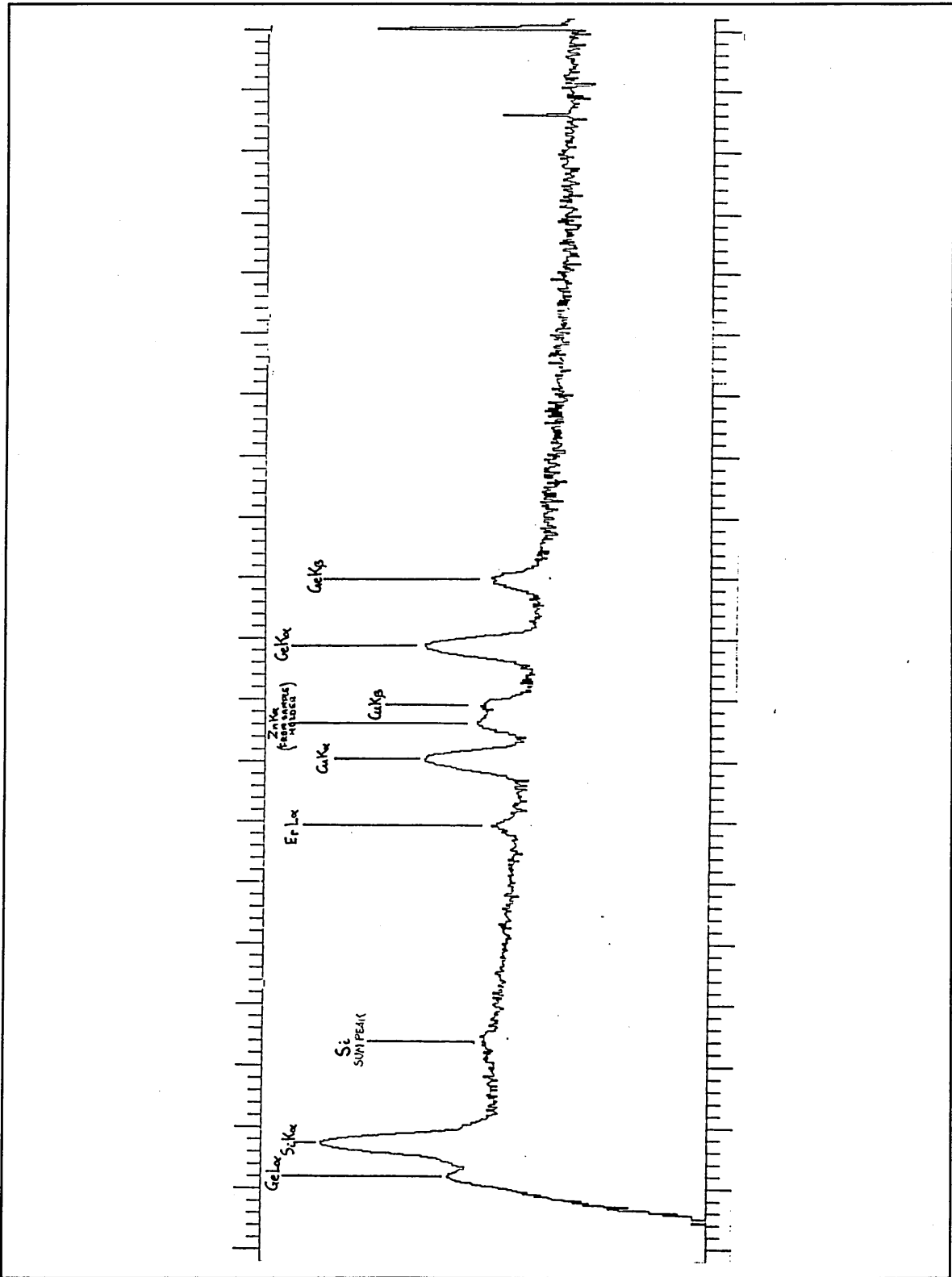


Figure 34. X-ray spectrum. Fibre type 3023.02.

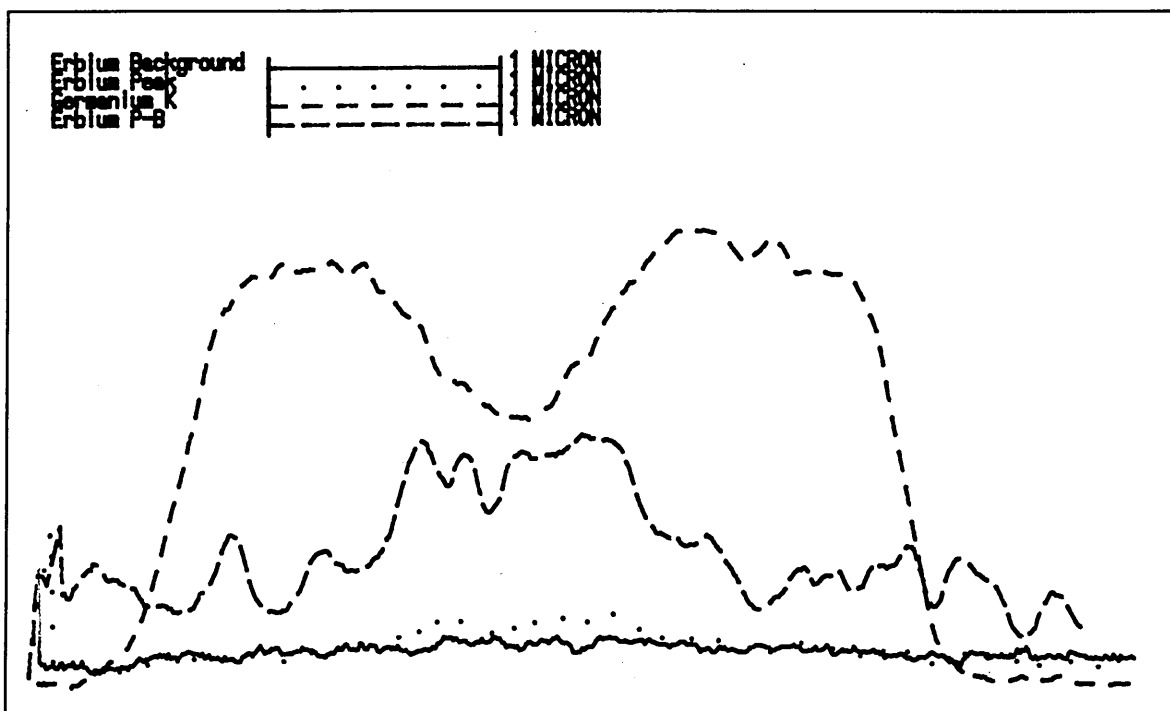


Figure 35. X-ray linescans. Fibre type 3023.02. Germanium, erbium peak, erbium background and erbium peak-background.

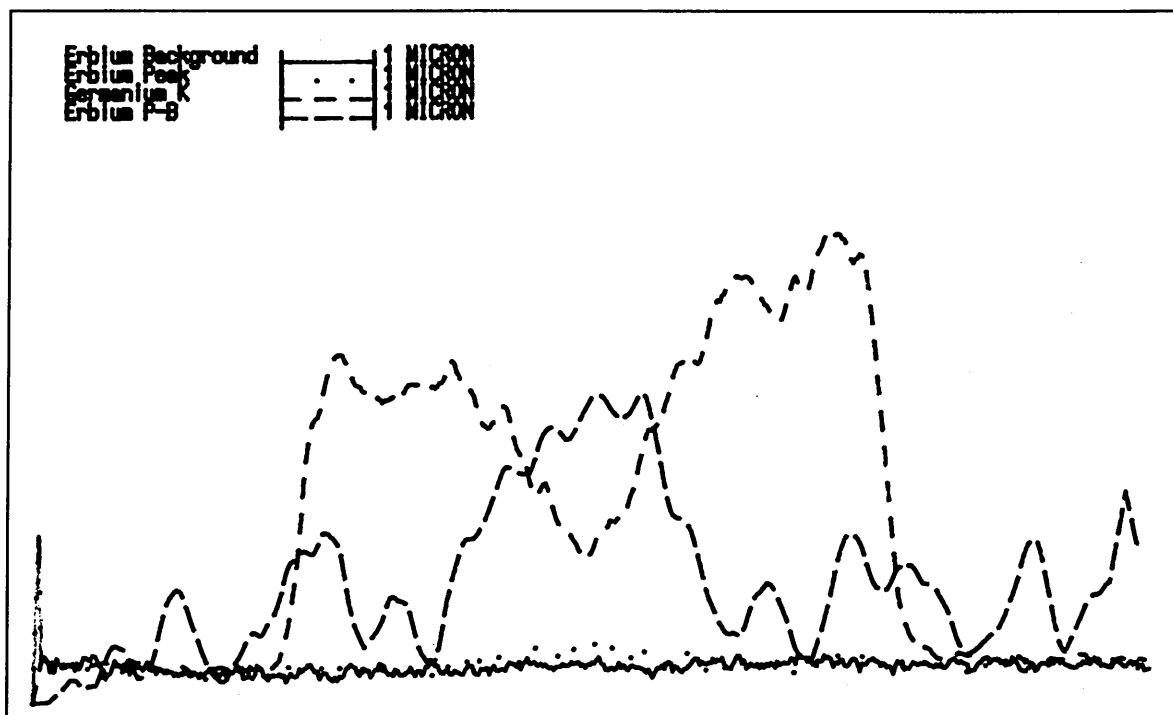


Figure 36. Fibre type 3023.03. Germanium, erbium peak, erbium background and erbium peak-background.

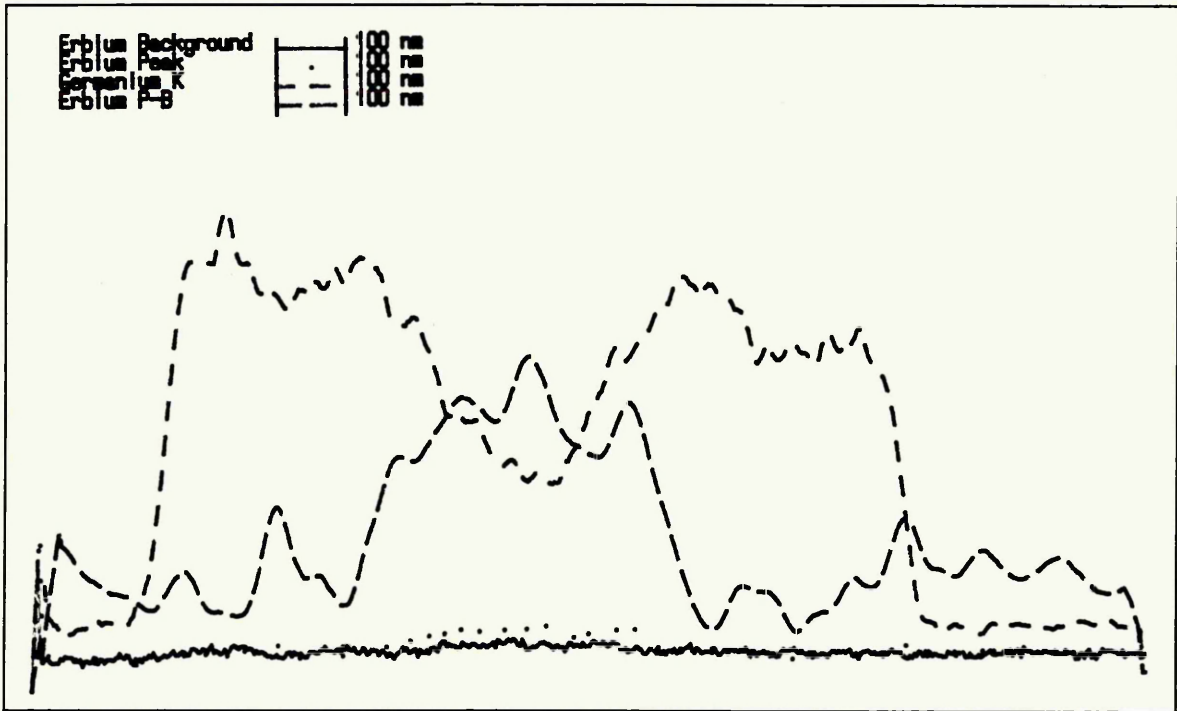


Figure 37. Fibre type 3023.04. Germanium, erbium peak, erbium background and erbium peak-background.

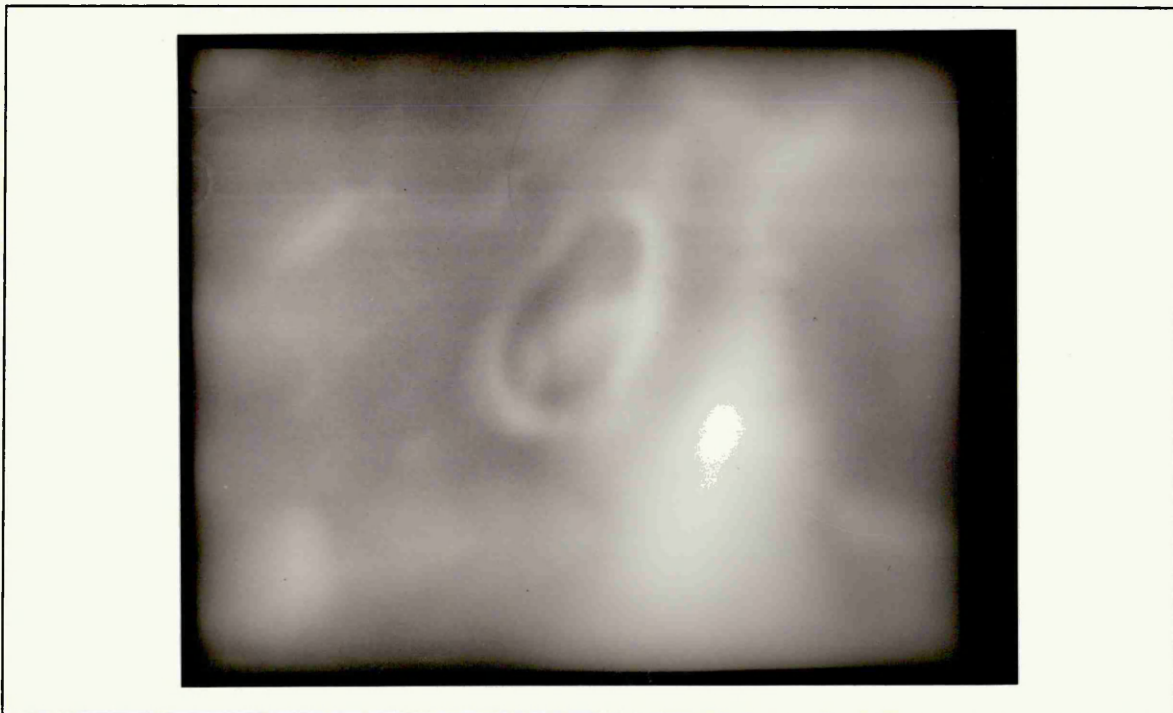


Figure 38. Core of fibre type 2073.02. x2,000

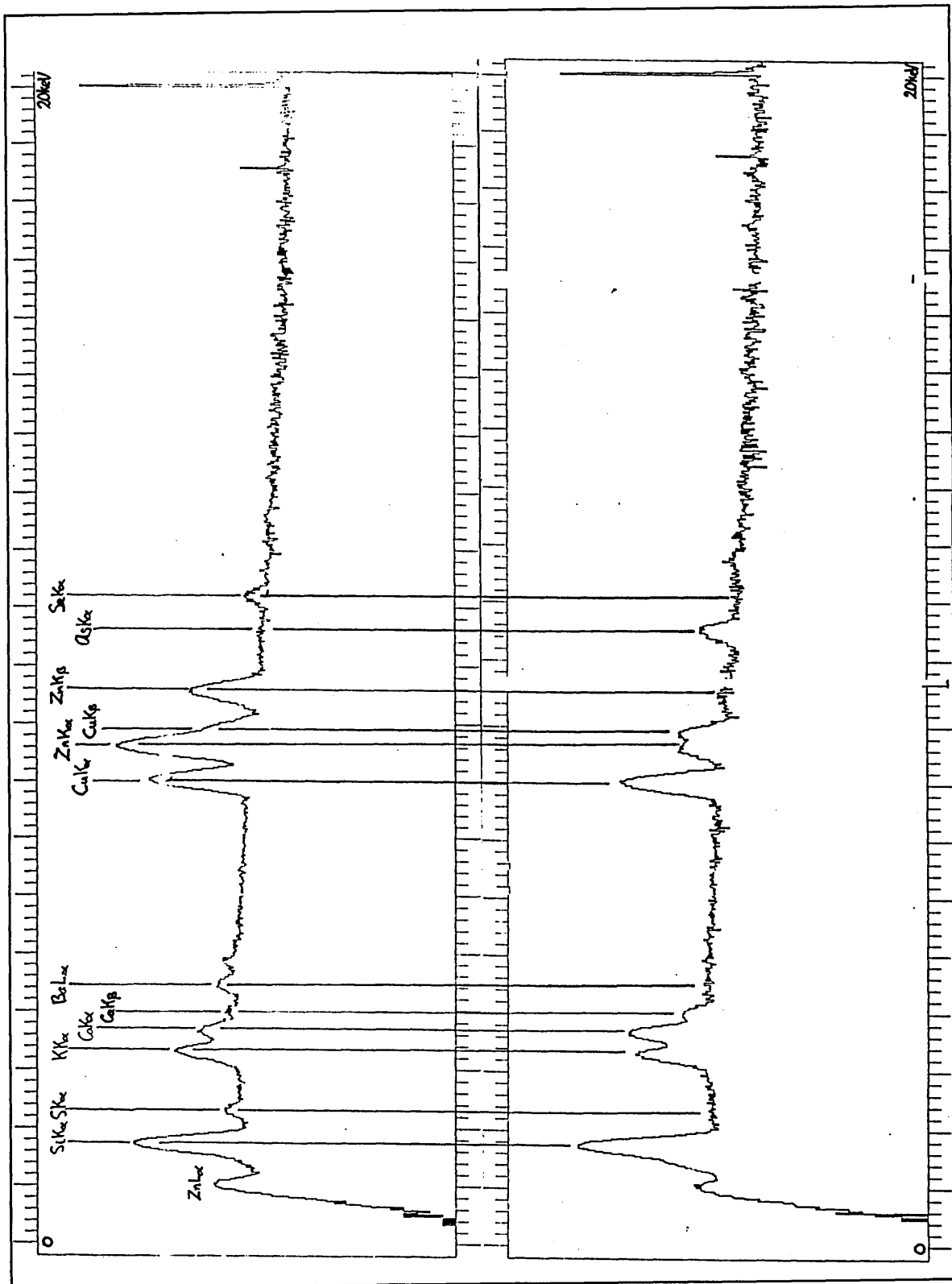


Figure 39. X-ray spectra for core and cladding regions of semiconductor fibre 2073.01.

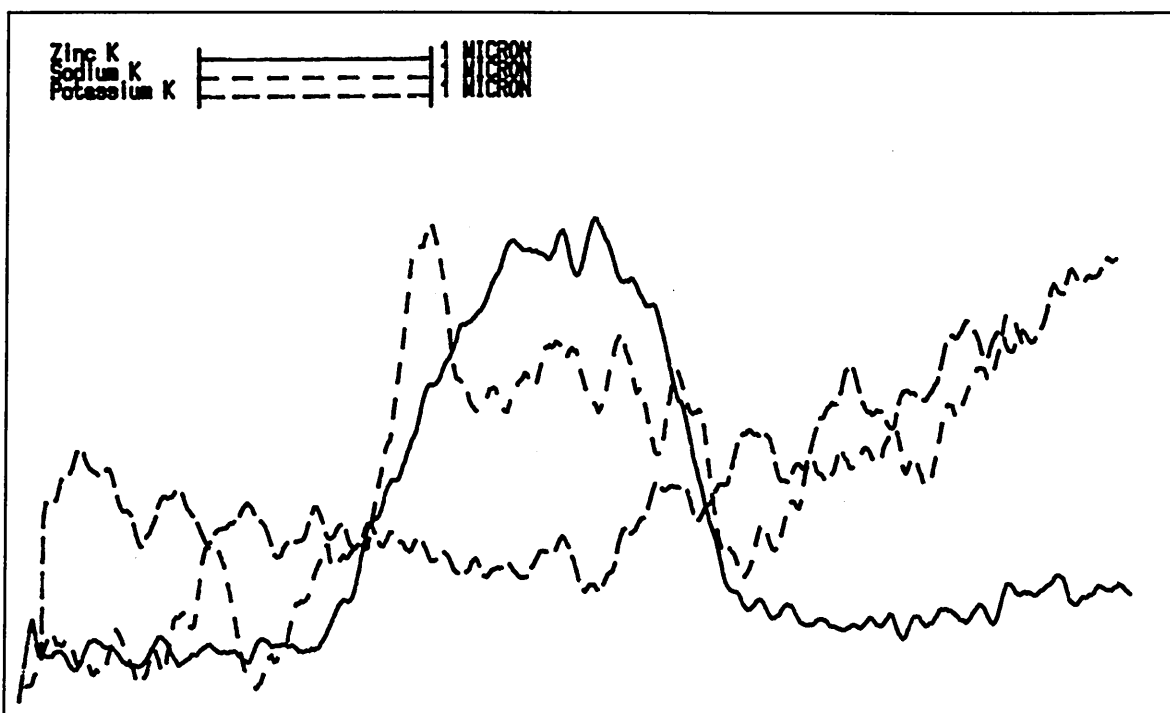


Figure 40. X-ray linescans for zinc, sodium and potassium. Fibre type 2073.01.

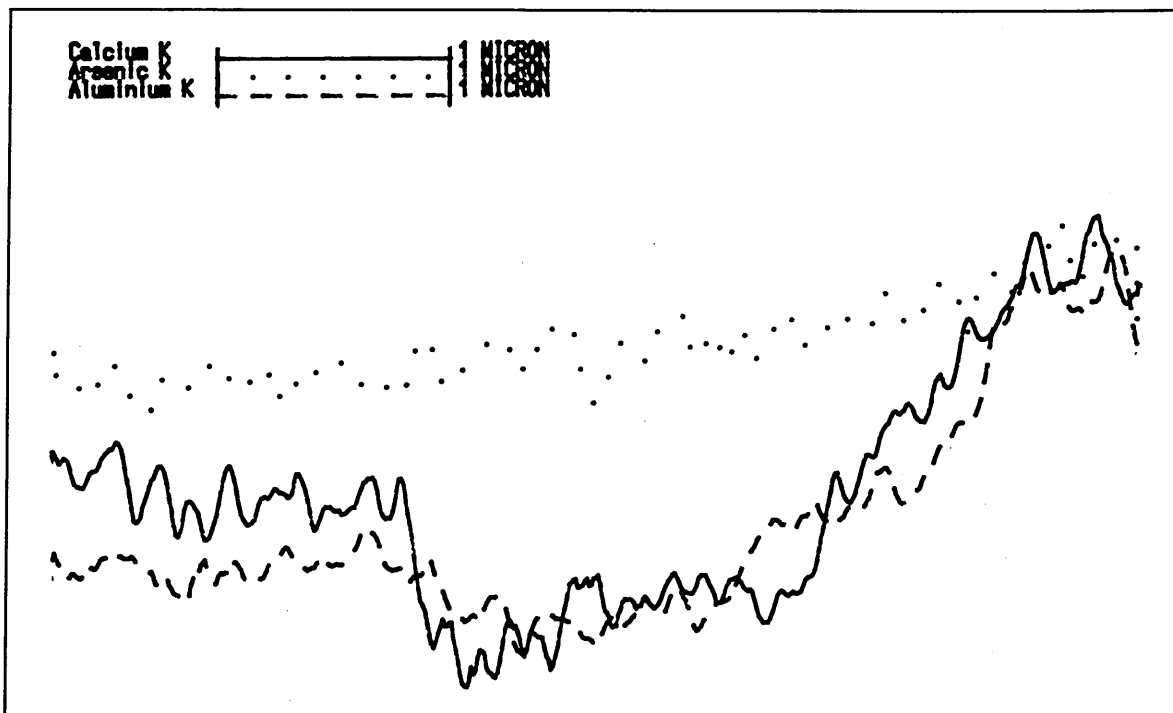


Figure 41. Fibre type 2073.01. Elements calcium, aluminium, arsenic and selenium.

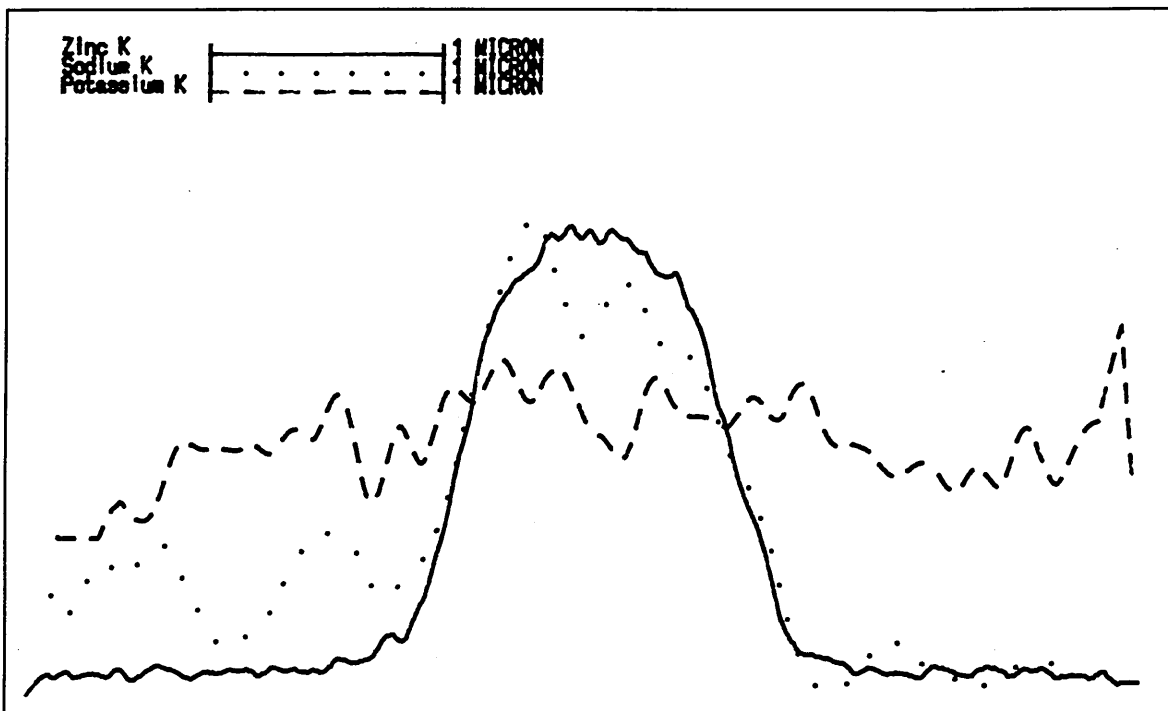


Figure 42. Fibre type 2073.02. X-ray linescans for zinc, sodium and potassium.

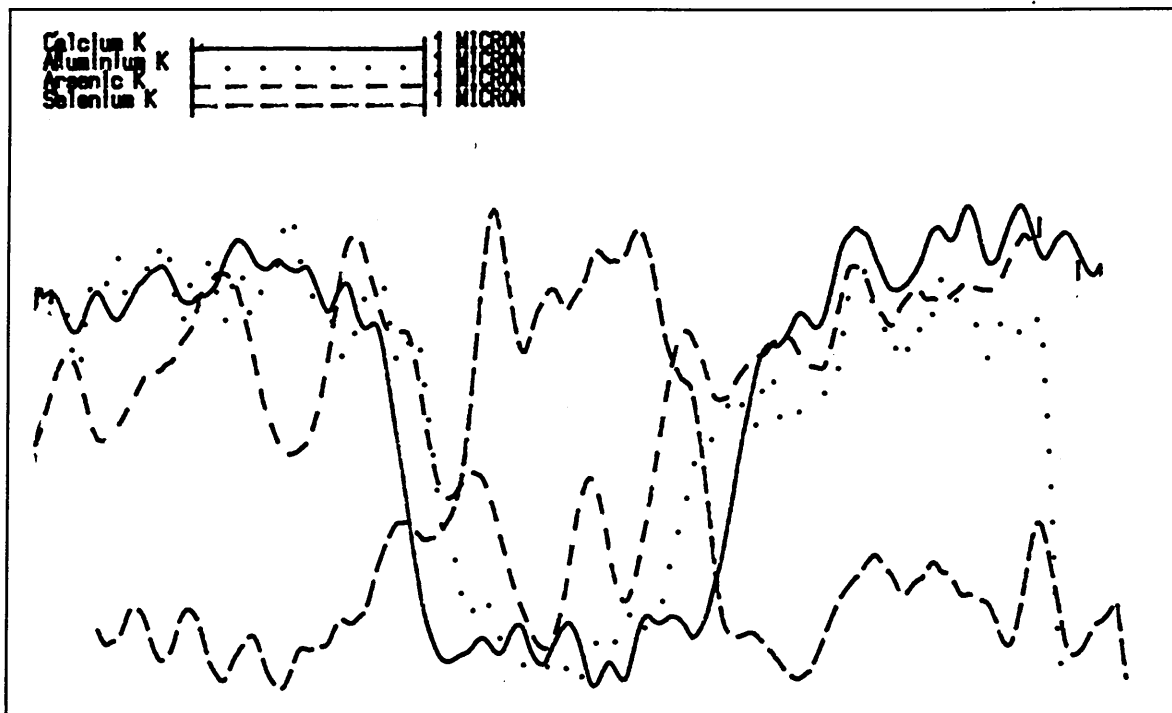


Figure 43. Fibre type 2073.02. X-ray linescans for calcium, aluminium, arsenic and selenium.

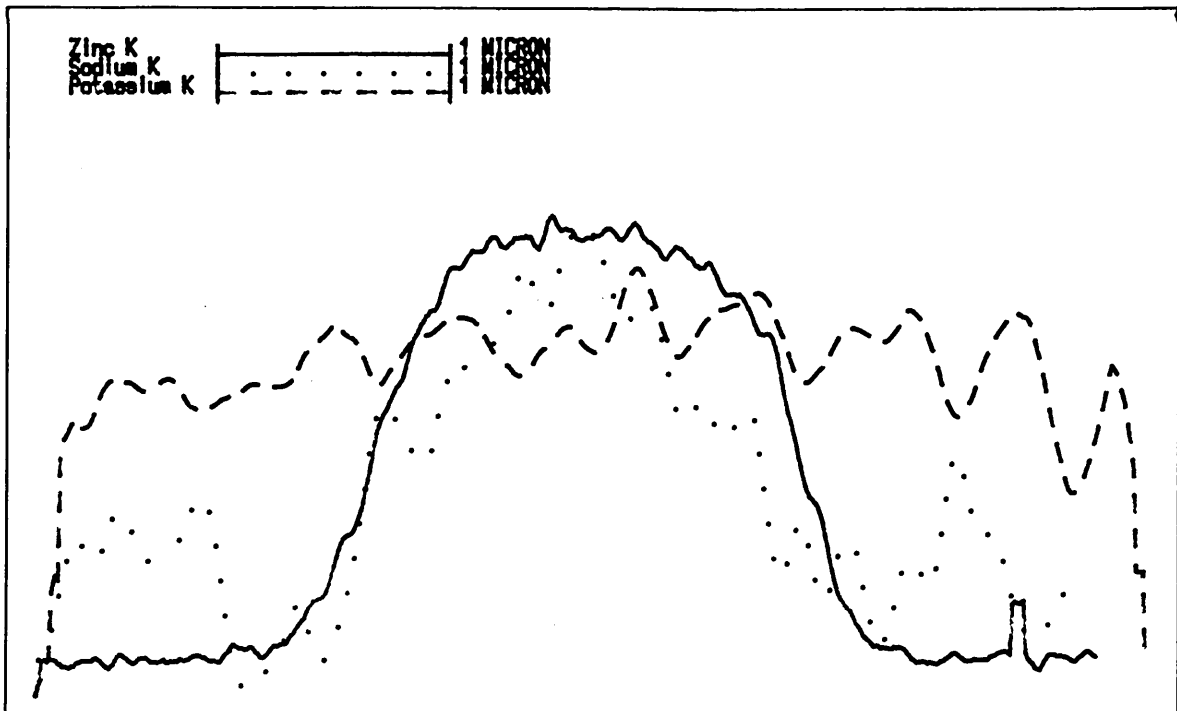


Figure 44. Fibre type 2073.03. X-ray linescans for zinc, potassium and sodium.

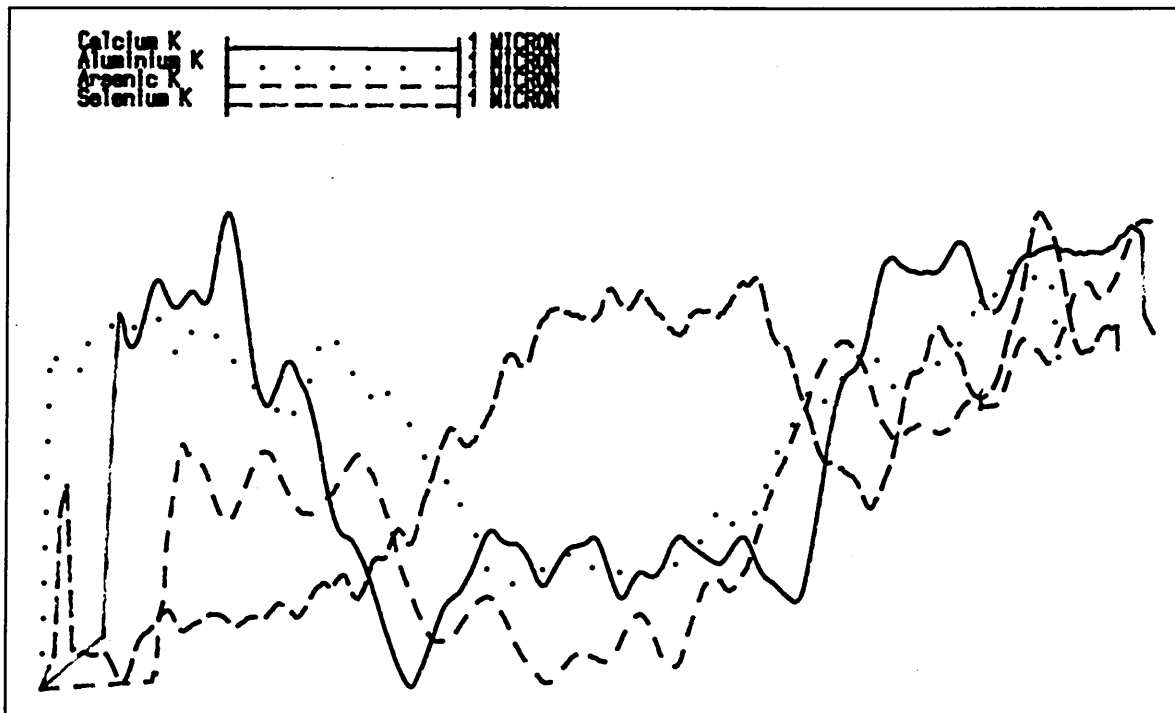


Figure 45. Fibre type 2073.03. X-ray linescans for calcium, aluminium, arsenic and selenium.

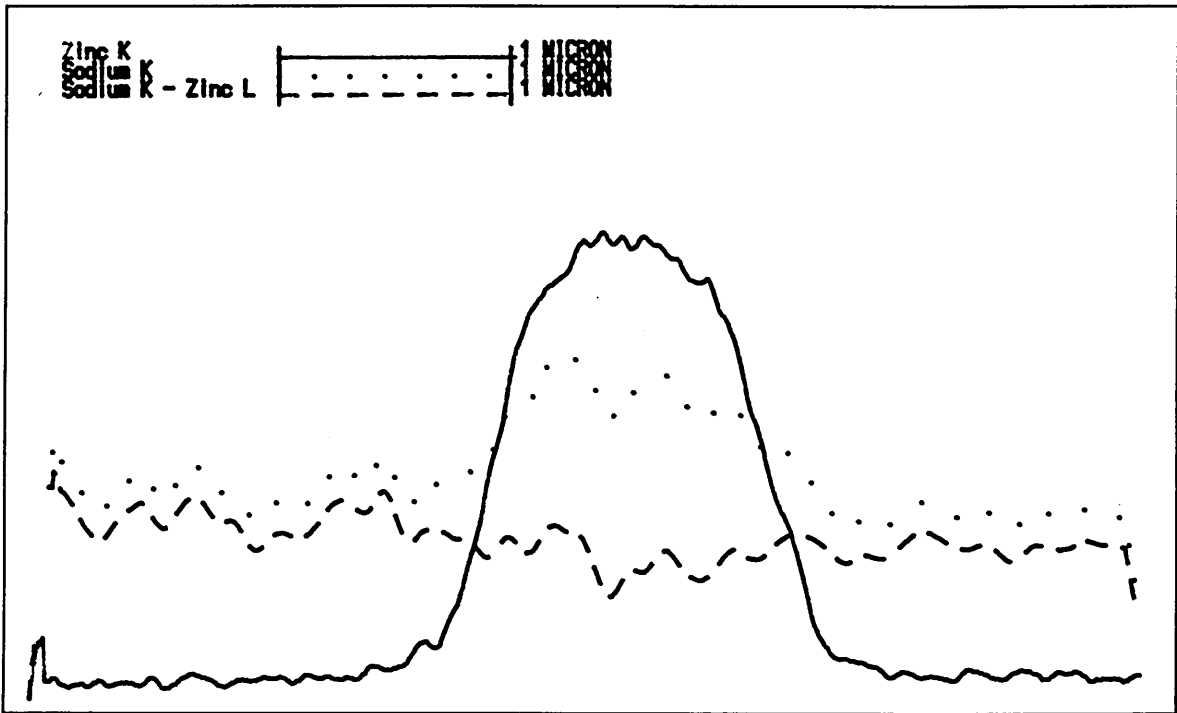


Figure 46. Linescan showing the effects of subtracting a proportion of the zinc signal from the sodium signal.

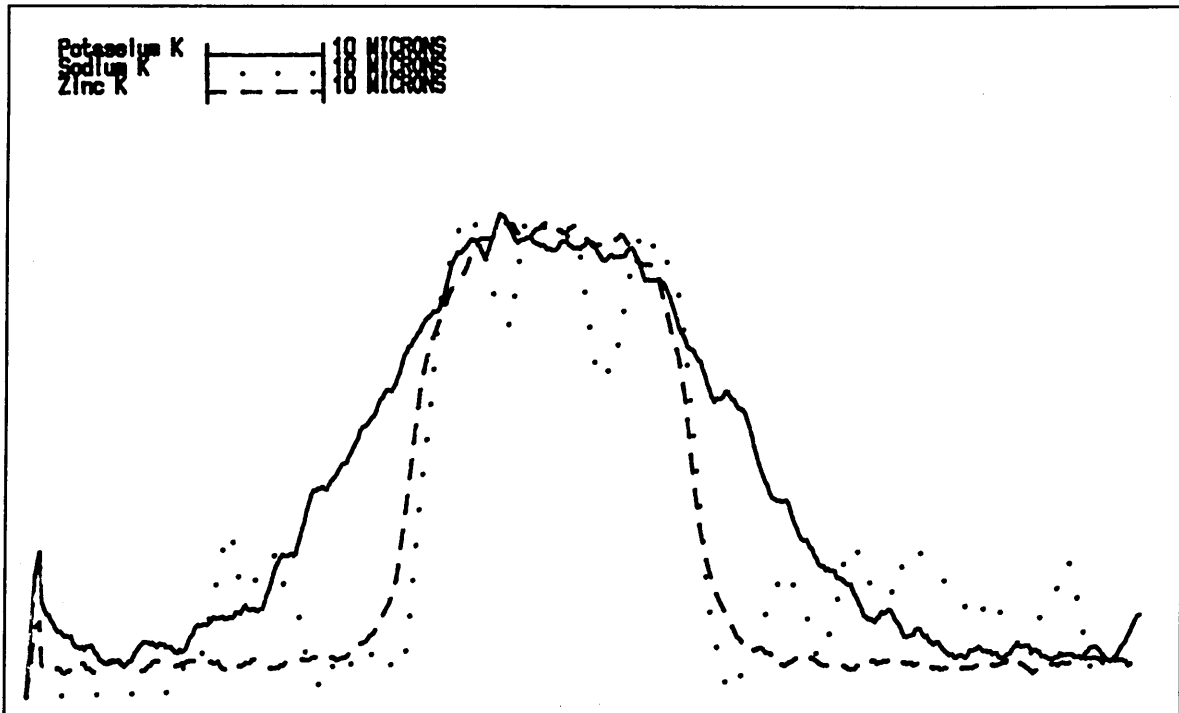


Figure 47. Fibre type 2074.01. X-ray linescans for zinc, potassium and sodium.

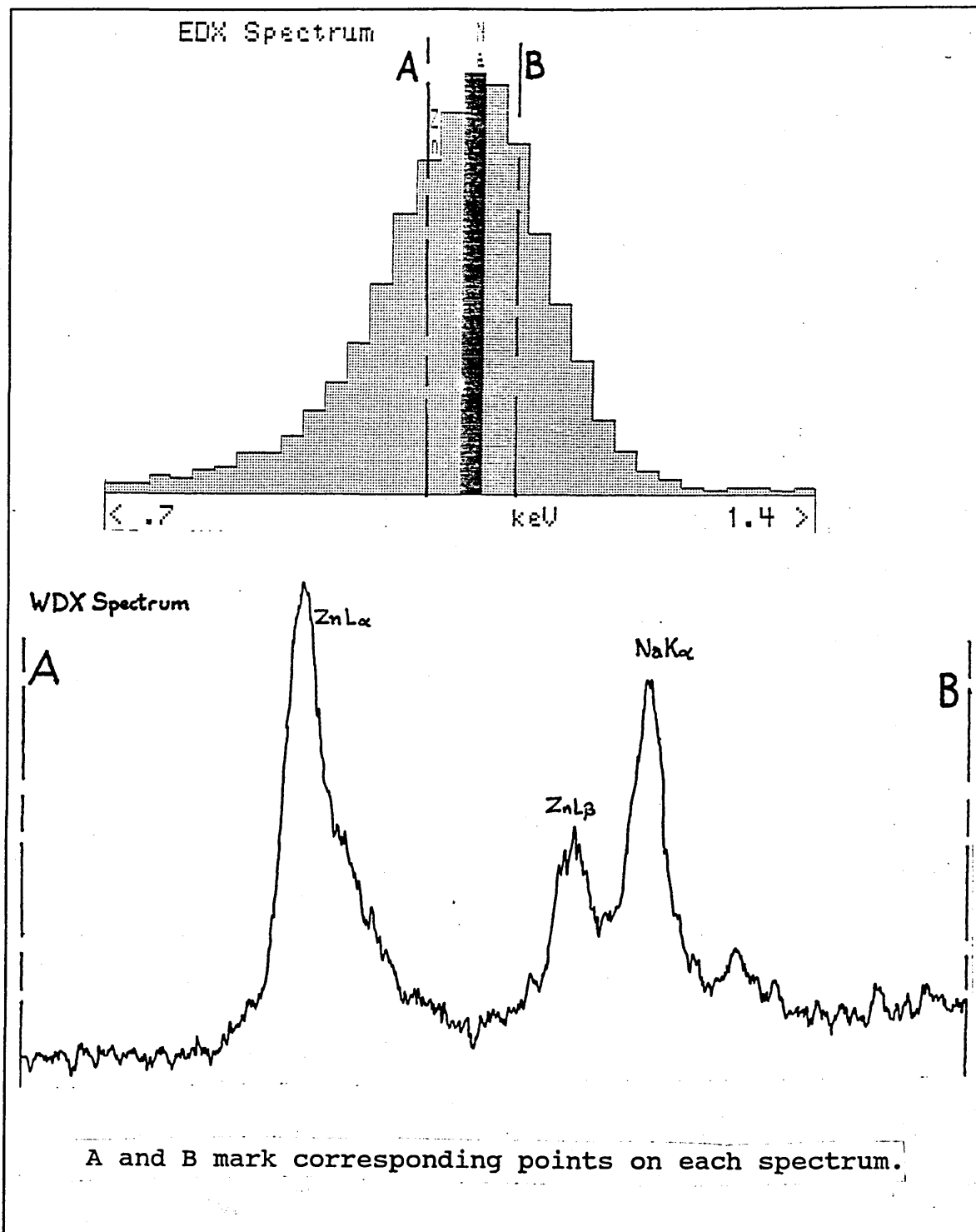


Figure 48. Comparison of the sodium region of the x-ray spectrum as resolved by wavelength and energy dispersive techniques.

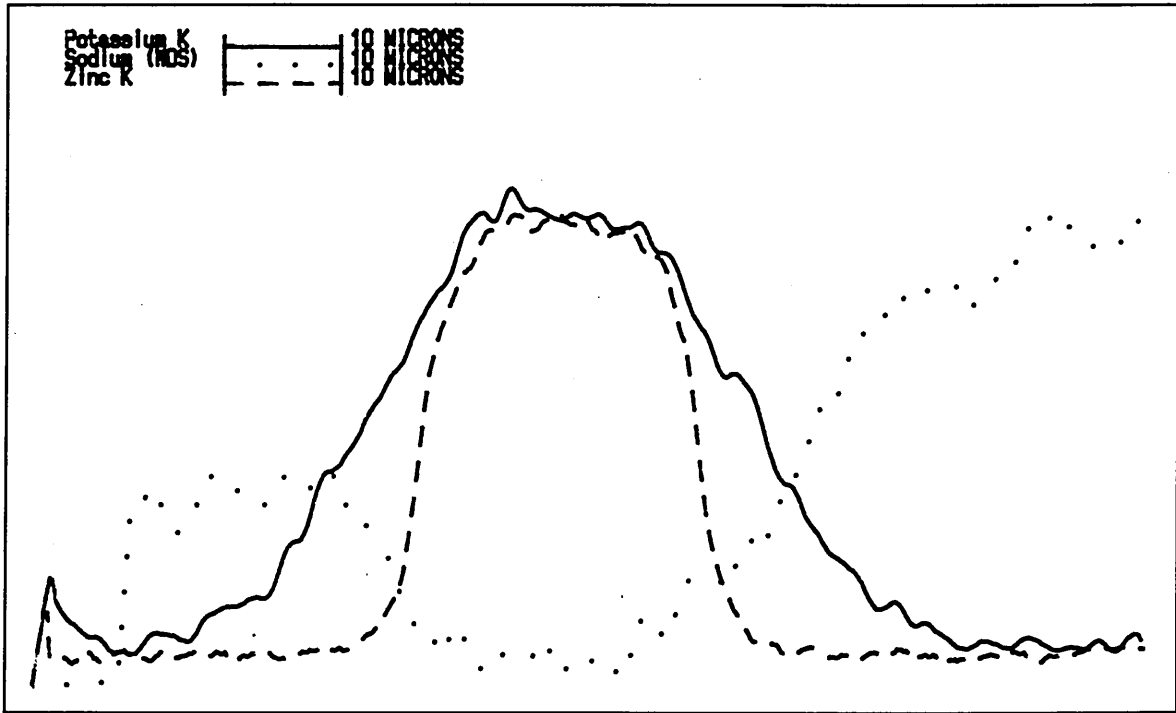


Figure 49. Fibre type 2074.01. Energy Dispersive X-ray linescans for potassium and zinc. Wavelength dispersive x-ray linescan for sodium.

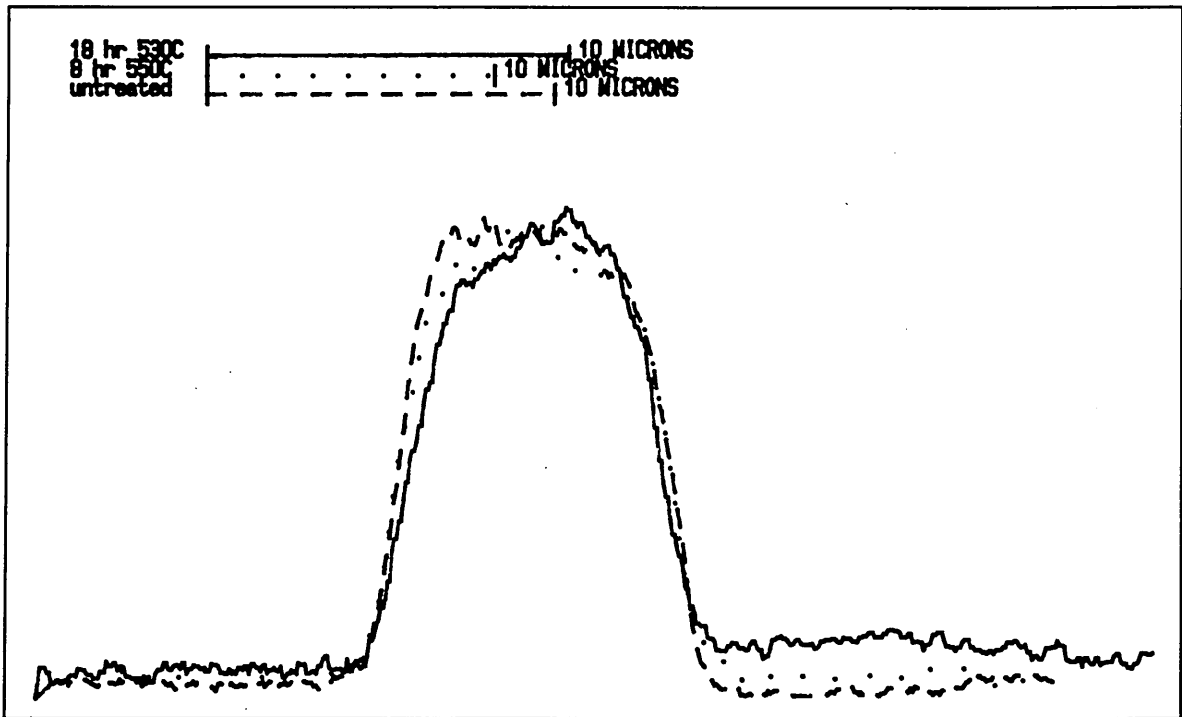


Figure 50. X-ray linescans for zinc. Fibre type 2075.04. Untreated fibre, fibre treated at 530°C for 18 hours and fibre treated at 550°C for 8 hours

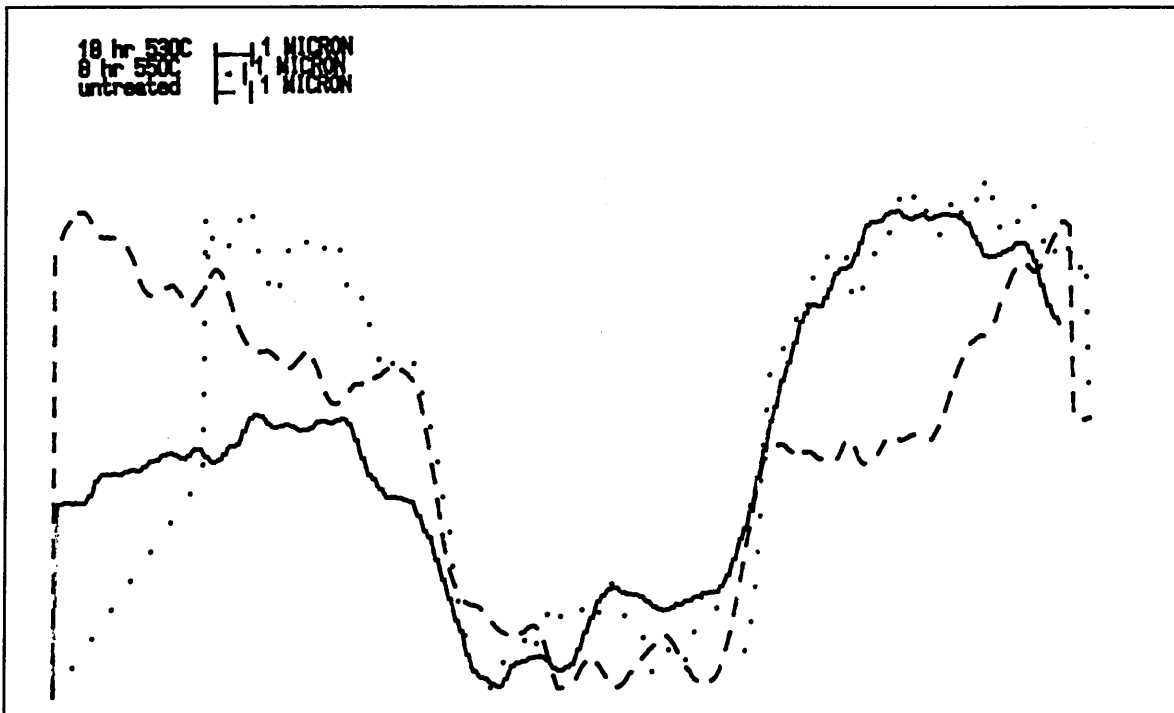


Figure 51. X-ray linescans for calcium for three differently heat treated samples of fibre type 2075.04

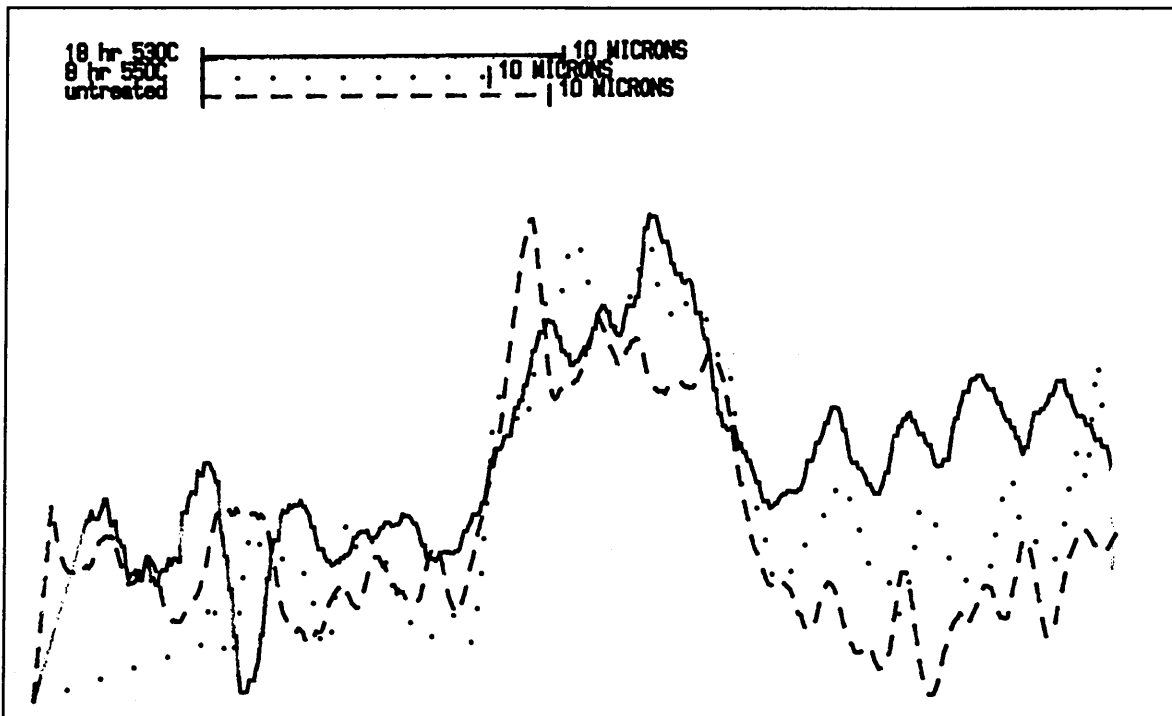


Figure 52. Selenium linescans for differently heat treated samples of 2075.04 fibre.

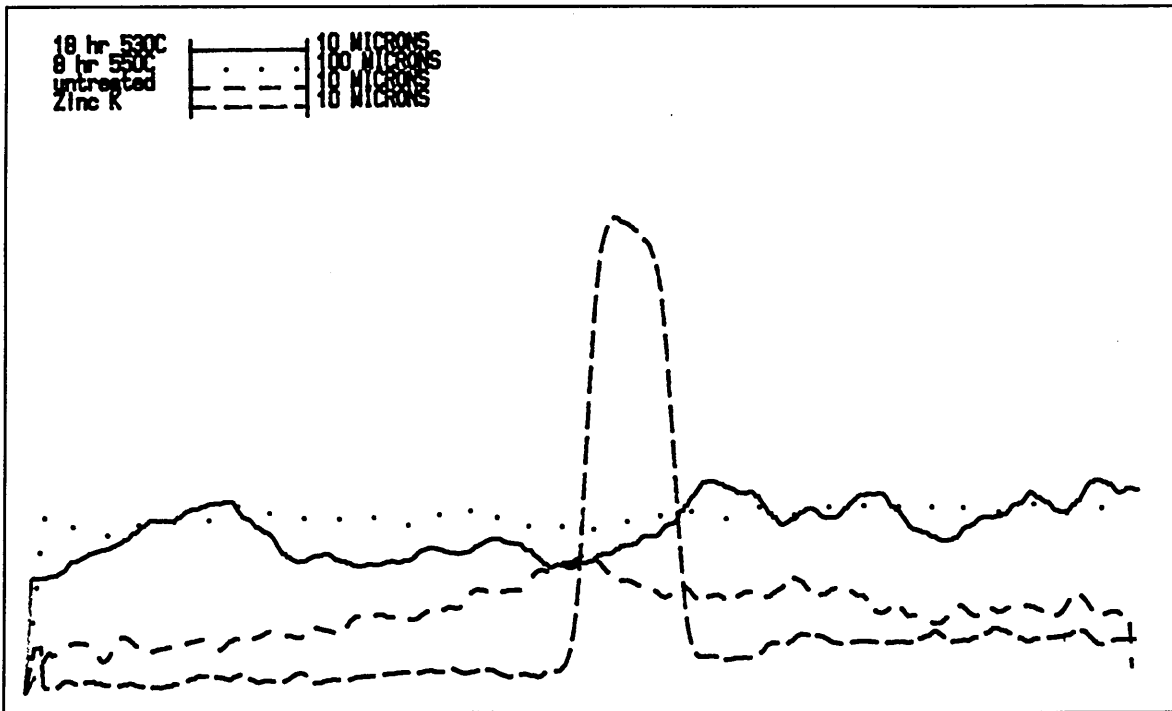


Figure 53. Potassium profiles for fibre type 2075.04 after a variety of heat treatments.

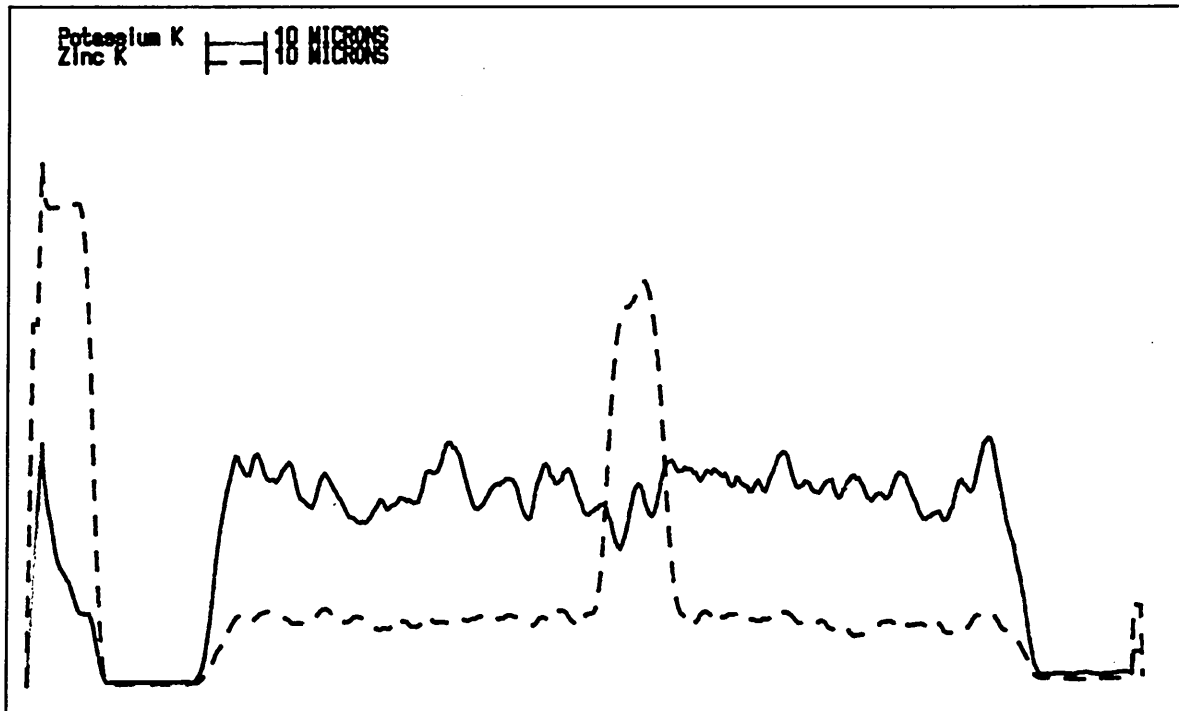


Figure 54. Zinc and potassium profiles across full fibre diameter for fibre type 2075.04.

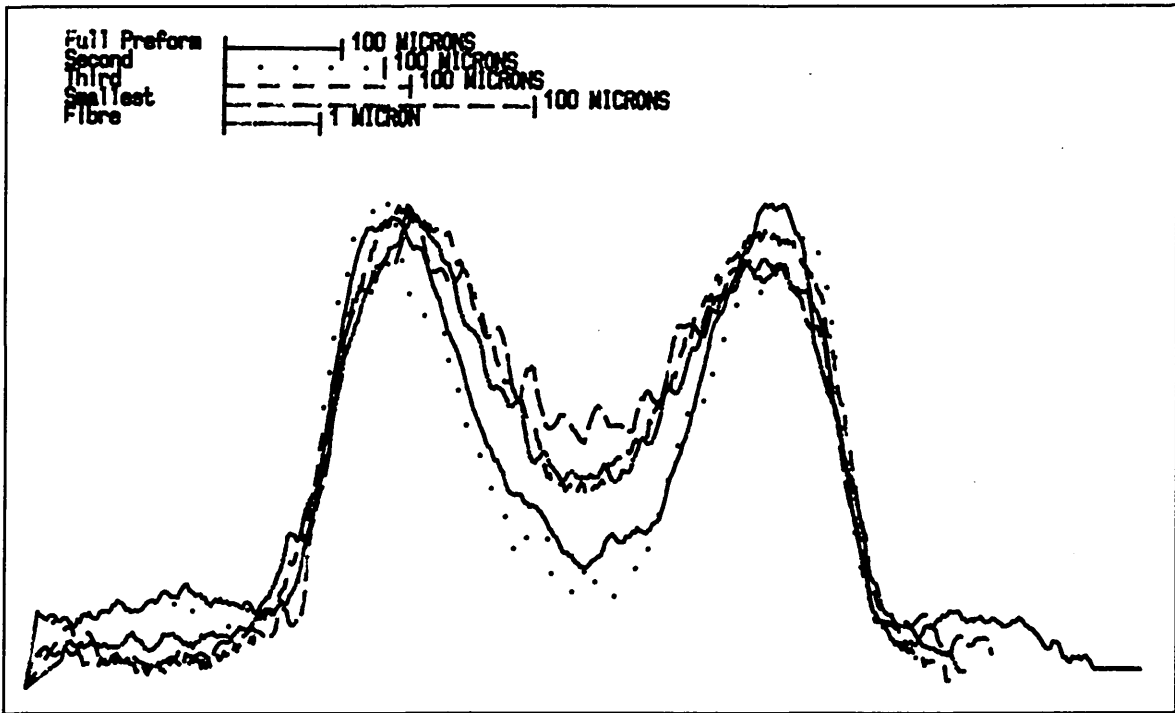


Figure 55. Fibre type 3115.01 and 3115 preform germanium profiles.

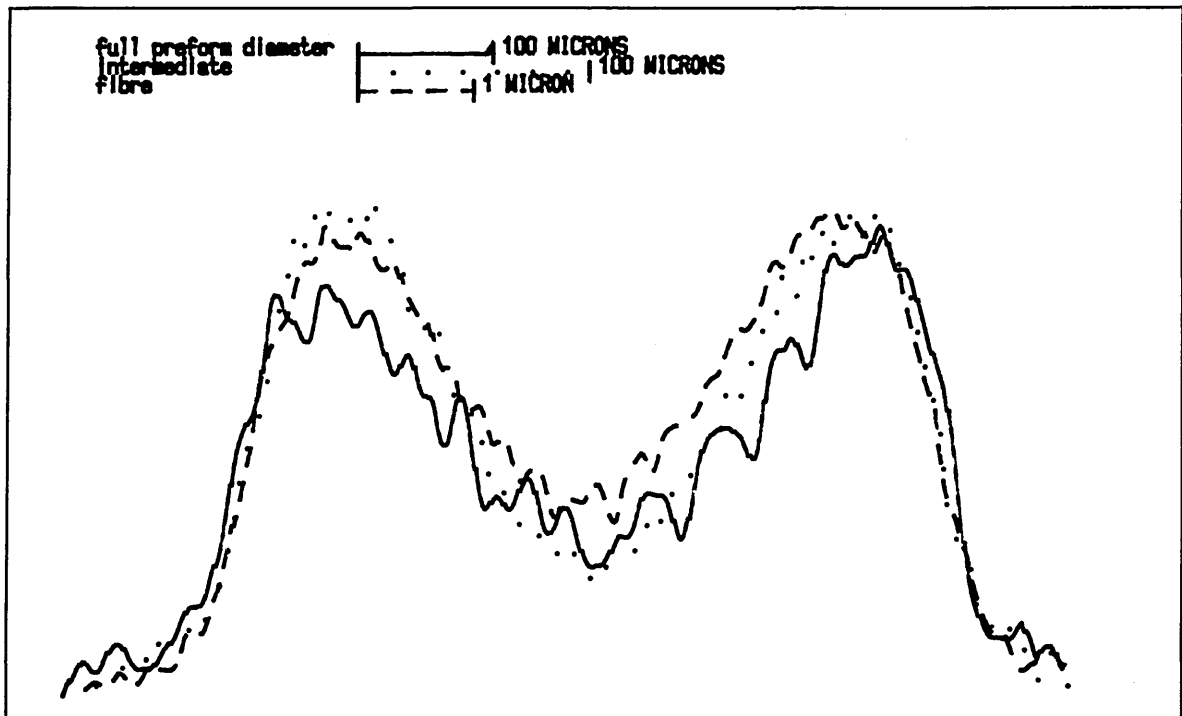


Figure 56. Germanium concentration profiles from 3115.01 fibre and several sections of 3115 preform.

pendix 1, Program to Acquire Data

```
000 REM program to read in rs232 data and write to a file in 500 seconds wort
010 INPUT "name for output file ";O$:O$=O$+".edx"
020 OPEN "COM1:75,N,8,2,RS,CS,DS,CD" AS #1
030 OPEN O$ FOR OUTPUT AS #2
040 GOSUB 10240:'HEADER DATA
050 FOR X=1 TO 500
060 T=0
070 FOR Y=1 TO 4
080 A$=INPUT$(1,#1)
090 A=ASC(A$)
100 B=0
110 FOR P=0 TO 7
120 A=A/2
130 BIT=-(A<>INT(A))
140 B=B+(2^(7-P))*BIT
150 A=INT(A)
160 NEXT P
170 T=T+B
180 NEXT Y
190 T=T/4:PRINT X;"----";T
200 WRITE #2,T
210 NEXT X
220 CLOSE
230 RETURN
240 'HEADER
250 INPUT "FIBRE TYPE:";F$
260 INPUT "DATE:";D$
270 INPUT "MAGNIFICATION:";M$
280 INPUT "Comments ";C$
290 PRINT #2,F$;CHR$(13);D$;CHR$(13);M$;CHR$(13);C$;CHR$(13)
300 RETURN
```

```

1 KEY OFF
10 REM PROGRAM TO PLOT OUT RESULTS
15 DIM A(9,500),T$(8),D$(8),F$(8),C$(8),GX(500),GY(500),I$(300)
16 F=0:NF=0:YSAVE =1
20 REM MENU
25 SCREEN 0:COLOR 1,5,5:CLS
26 KEY (11) OFF:KEY(12) OFF:KEY(13) OFF:KEY(14) OFF
30 LOCATE 3,25:PRINT "1 LOAD FILES"
40 LOCATE 6,25:PRINT"2 SET UP PLOT"
45 LOCATE 9,25:PRINT"3 OUTPUT TO PLOTTER"
47 LOCATE 12,25:PRINT"4 SAVE PLOT FILES"
48 LOCATE 15,25:PRINT "5 LABELS"
50 A$=INKEY$:IF A$="" THEN GOTO 50
60 IF A$<"1" OR A$>"5" THEN 50
70 ON VAL(A$) GOSUB 1000,2000,4000,500,5000
80 GOTO 25
500 COLOR 1,3:CLS
510 INPUT "FILENAME: FOR PLOT FILE ";N$
520 INPUT "PLOTS TO SAVE (PLOTNUMBERS ONLY)";A$
525 INPUT "DESCRIPTION FOR INDEX ";O$
530 N$=N$+".PLT":OPEN N$ FOR OUTPUT AS #1
540 PRINT #1,A$,CHR$(13)
550 FOR A=1 TO LEN(A$)
555 F=VAL(MID$(A$,A,1))
560 PRINT
      #1,T$(F),CHR$(13),D$(F),CHR$(13),M$(F),CHR$(13),C$(F),CHR$(13)
570 FOR B=1 TO 500:PRINT #1,A(F,B):NEXT B
580 NEXT A
585 CLOSE #1
586 OPEN "INDEX.IDX" FOR APPEND AS #1:PRINT #1,N$;A$;O$:CLOSE #1
590 RETURN
600 RETURN
1000 COLOR 5,2:CLS:Y=YSAVE:X=1:YD=1
1002 KEY(11) ON:KEY(12) ON: KEY(13) ON: KEY(14) ON
1003 ON KEY(11) GOSUB 1400:ON KEY (14) GOSUB 1460
1010 OPEN "INDEX.IDX" FOR INPUT AS #1:FOR A=1 TO 300:IF NOT
      EOF(1) THEN INPUT #1,I$(A):NEXT A
1012 IF A<10 THEN SMALL=-1
1015 CLOSE #1
1020 TOP=1
1025 IF YD<>0 THEN YDD=YD:YD=0
1030 IF YDD<0 THEN Y=Y+YDD:IF Y<TOP THEN TOP=Y
1035 IF YDD>0 THEN Y=Y+YDD:IF Y>(TOP+10) THEN TOP=Y-10
1040 IF YDD<>0 THEN YDD=0:FOR A=0 TO 10:LOCATE A+1,1 :COLOR
      5,(2-((A+TOP)=Y)):PRINT I$(A+TOP);SPACE$(80-
      LEN(I$(A+TOP))):NEXT A
1050 IF I$(Y)<"!" AND TOP>0 THEN Y=Y-1:TOP=Y-10:GOTO 1050
1060 A$=INKEY$:IF A$=CHR$(13) THEN CLS:TOP=0:YSAVE=Y:RETURN
1065 IF A$<"1" OR A$>"7" THEN GOTO 1025
1070 F$=LEFT$(I$(Y),12):MID$(I$(Y),1)>("-----"+A$+"-----"):YD=1
1080 F=VAL(A$)
1155 A$="N"
1160 OPEN F$ FOR INPUT AS #1
1161 IF RIGHT$(F$,3)="PLT" THEN INPUT#1,A$,T$:NF=LEN(A$):F=0
1165 IF F>NF THEN NF=F

```

```

1166 IF A$<>"N" THEN F=F+1:A$=MID$(A$,2)
1170 INPUT #1,T$(F),D$(F),M$(F),C$(F)
1190 FOR A=1 TO 500:IF NOT EOF(1) THEN INPUT #1,A(F,A):NEXT A
1197 IF A$<>"N" AND A$<>"" THEN INPUT #1,Z:GOTO 1166
1198 CLOSE #1
1200 IF NF<9 THEN GOTO 1025
1210 RETURN
1400 IF Y>0-YD THEN YD=YD-1:RETURN
1410 RETURN
1460 IF Y<299+YD THEN YD=YD+1:RETURN
1470 RETURN
1480 RETURN
2000 F=0:CLS:SCREEN 8:WINDOW (0,0)-(500,300):X=251:Y=1
2001 ON KEY(4) GOSUB 9000
2005 GOSUB 2500
2006 KEY(11) ON:KEY(12) ON:KEY(13) ON:KEY(14) ON
2007 ON KEY(11) GOSUB 2600:ON KEY (12) GOSUB 2610:ON KEY (13)
GOSUB 2620:ON KEY(14) GOSUB 2630
2008 XD=0:YD=0
2009 A$=INKEY$:LOCATE 1,1:PRINT "Plot N,Smooth
N,Centre,Top,Bottom,Magnify,Expand,mAths,Home cursor,Fin
ished"
2010 LOCATE 1,1:PRINT " lot N, mooth N, entre, op, ottom, agnify,
xpand,m ths, ome cursor, inished"
2012 IF A$="" THEN 2009
2015 IF INSTR("PS",A$)THEN B$=INKEY$:IF B$="" THEN 2015
2016 IF A$="C" THEN B=Y:GOSUB 2400
2017 IF A$="B" THEN BOT=Y
2018 IF A$="T" THEN TOP=Y
2019 IF A$="F" THEN RETURN
2040 IF A$="P" THEN GOSUB 6000
2080 IF A$="S" THEN GOSUB 3000
2090 IF A$="E" THEN GOSUB 3120
2100 IF A$="F" THEN RETURN
2110 IF A$="M" OR A$="m" THEN GOSUB 3300
2120 IF A$="H" THEN YD=-Y:XD=251-X:GOSUB 2640
2130 IF (TOP*BOT)<>0 THEN GOSUB 7000
2140 IF A$="A" THEN GOSUB 3500
2399 GOTO 2006
2400 IF X>250 THEN B=X-250:GOSUB 7050
2410 IF X<250 THEN B=250-X:GOSUB 7060
2420 RETURN
2430 RETURN
2450 LOCATE (1,1):INPUT "MAX VALUE ";MAX;" MIN VALUE";MIN
2499 GOTO 2006
2500 PSET (0,0):LINE -(500,0)
2510 GET (0,0)-(500,0),GX
2520 PSET (250,0):LINE -(250,250)
2530 GET (250,250)-(250,0),GY
2540 RETURN
2600 YD=YD+1:XD=0:GOTO 2640
2610 YD=0:XD=XD-1:GOTO 2640
2620 YD=0:XD=XD+1:GOTO 2640
2630 YD=YD-1:XD=0:GOTO 2640
2640 PUT (0,Y),GX,XOR:PUT (X,0),GY,XOR

```

```

2650 X=X+XD:Y=Y+YD
2660 PUT (0,Y),GX,XOR:PUT (X,0),GY,XOR
2670 RETURN 2007
2999 GOTO 2006
3000 REM SMOOTH FILE
3010 IF VAL(B$)=0 THEN RETURN
3020 P=2*VAL(B$)+2
3025 GOSUB 6100
3030 FR=9:FS=F
3040 TOT=0
3050 C=INT(P/2)
3060 FOR B=1 TO P:TOT=TOT+A(FS,B):NEXT B
3070 FOR A=C TO 500-C
3080 A(FR,A)=TOT/P
3085 PRESET (A,A(FS,A)):PSET (A,A(FR,A))
3090 TOT=TOT+A(FS,(A+C))-A(FS,A-C)
3100 NEXT A
3105 FOR A=1 TO 500:A(FS,A)=A(FR,A):NEXT A
3110 RETURN
3120 REM? EXPAND?TO?FULL?SCALE
3140 MAX=0:MIN=256:A(F,2)=A(F,3):A(F,1)=A(F,2)
3150 FOR A=1 TO 500
3160 IF A(F,A)<MIN THEN MIN=A(F,A)
3165 IF A(F,A)>MAX THEN MAX=A(F,A)
3170 NEXT A
3180 MAX=MAX-MIN
3190 FOR A=1 TO 500
3195 PRESET (A,A(F,A))
3200 A(F,A)=(A(F,A)-MIN+3)/MAX*250
3205 PSET (A,A(F,A))
3210 NEXT A
3220 RETURN
3300 M=251/X
3305 IF M>.999 AND M<1.001 THEN LOCATE 1,1:INPUT "required magni
fication";M1:M=VAL(M$(F))/M1
3320 FOR A=1 TO 500
3325 C=(A*M):IF C<500 THEN A(7,A)=A(F,C) ELSE A(7,A)=0
3326 NEXT A
3330 FOR A=1 TO 500:PRESET (A,A(F,A)):A(F,A)=A(7,A):PSET
(A,A(F,A)):NEXT A
3340 M$(F)=STR$(VAL(M$(F))/M)
3350 RETURN
3500 LOCATE 1,1:PRINT SPACE$(80)
3510 LOCATE 1,1:INPUT "MATHEMATICAL EXPRESSION, USE [1] FOR
DATASET 1 ETC ";A$
3514 A$=" "+A$
3520 A= INSTR(A$,"["):IF A=0 THEN 3600
3530 V=VAL(MID$(A$,(A+1),1)):IF V=0 THEN 3600
3540 A$=LEFT$(A$,(A-1))+A(" "+MID$(STR$(V),2)+",A")+MID$(A$,(A+3))
3550 GOTO 3520
3600 LOCATE 1,1:PRINT SPACE$(80)
3620 LOCATE 1,1:INPUT "RESULT DATASET ";F :PRINT A$
3625 A$="A (" +MID$(STR$(F),2)+",A)="+A$:PRINT A$
3640 OPEN "HORRID.BAS" FOR OUTPUT AS #1:PRINT #1,"3655 FOR A= 1
TO 500:";A$;":NEXT A":CLOSE #1

```

```

3645 CHAIN MERGE "HORRID.BAS",3655,ALL
3655 FOR A= 1 TO 500:A(1,A)= A(1,A)-A(2,A):NEXT A
3670 B$=MID$(STR$(F),2):GOSUB 6000
3675 F$(F)=F$(V):M$(F)=M$(V):D$(F)=D$(V):C$(F)="MANIPULATED"
3680 GOSUB 2000
3690 GOTO 20
4000 REM PLOTTER OUTPUT
4005 COLOR 4,2,2:CLS:GOSUB 4400
4010 OPEN "COM1:9600,n,8,1,CS65535" AS #1
4020 PRINT #1,"IN SC ";I$;"
4030 FOR F=1 TO NF
4035 IF T$(F)="" THEN GOTO 4110
4040 PRINT #1,"PU 10,";(350-10*F);";SI .1,.2;":IF COLOUR=1 THEN
PRINT #1,"SP ";F
4045 IF COLOUR=0 THEN PRINT #1,"LT ";F;";,1;SP 1;"
4050 PRINT #1,"LB ";C$(F);CHR$(3)
4052 L=5.22*VAL(M$(F)):L$="1 MICRON"
4053 IF L<10 THEN L=L*10:L$="10 MICRONS"
4054 IF L<10 THEN L=L*10:L$="100 MICRONS"
4055 IF L<10 THEN L=L*10:L$="1 MILLIMETER"
4056 IF L>100 THEN L=L/10:L$="100 nm"
4060 PRINT #1,"PR 10,0;PD;XT;PR ";L;";,0;XT;LB ";L$;CHR$(3);";PU
0,0;"
4070 PRINT #1,"PA 0,0;PD"
4080 FOR A=1 TO 500
4090 IF A(F,A)>0 THEN PRINT #1,"PA";A;";,";A(F,A);";"
4100 NEXT A
4110 PRINT #1,"PU;SP 0;"
4120 NEXT F
4127 GOSUB 5010
4130 RETURN
4400 REM set type of plot
4405 CLONG=0
4410 INPUT "colour or black and white (c,b)";C$:IF C$="C" OR
C$="c" THEN COLOUR=1 ELSE COLOUR =0
4420 INPUT "top (T), bottom (B) or whole screen (W)";C$
4430 IF INSTR("tbwTBW",C$)=0 THEN GOTO 4420
4440 IF C$="w" OR C$="W" THEN I$="-10,1000,-10,510;"
4450 IF C$="b" OR C$="B" THEN I$="-10,1280,-140,790;"
4460 IF C$="t" OR C$="T" THEN I$="-10,1280,-570,380;"
4470 CLS
4480 FOR F=1 TO NF
4490 LOCATE F,1: PRINT T$(F);" ";D$(F);" ";C$(F):LOCATE (F+10),1
:INPUT "COMMENT";C$(F)
4495 IF CLONG<LEN(C$(F)) THEN CLONG=LEN(C$(F))
4500 NEXT F
4510 FOR F=1 TO NF:C$(F)=LEFT$((C$(F)+SPACE$(40)),CLONG):NEXT F
4520 RETURN
5000 REM LABELS
5005 OPEN "COM1:9600,n,8,1,CS65535" AS #1
5009 PRINT #1,"IN SC -10,1000,-10,510;"
5010 COLOR 4,1,1:CLS:X=50:Y=290:XD=0:YD=0
5015 INPUT "Label Title Box or Quit";T$:T=1+INSTR("LTBQ",T$):ON T
GOTO 5015,5020,5200,5300,5400
5020 INPUT "LABEL";A$

```

```

5050 INPUT "PEN TO USE ";P
5060 GOSUB 5600
5070 PRINT #1,"SI 0.1,0.2;SP ";P;" ;LB ";A$;CHR$(3)
5150 GOTO 5010
5200 COLOR 0,6,6:CLS
5205 L=0:GOSUB 5600:Y=Y+12
5210 INPUT "TITLE ?";T$
5215 INPUT "PEN TO USE ";P
5220 U$="":IF LEN(T$)>55 THEN T=INSTR(50,T$," "):U$=MID$(T$,T+1)
      :T$=LEFT$(T$,T-1)
5230 X=((55-LEN(T$))/2)*9:Y=Y-12
5250 PRINT #1,"SP ";P;" ;PU ";X;" ,";Y;" ;SI .225,.225;LB";T$;
      CHR$(3)
5260 T$=U$:IF T$<>" " THEN GOTO 5220
5270 GOTO 5010
5300 COLOR 2,5,5:CLS
5310 INPUT "BOX ROUND PLOT?";Y$: IF Y$<>"Y" THEN 5340
5315 INPUT "pen to use ";P
5320 PRINT #1,"PU -10,-10;SP ";P;" ;PD 510,-10;PD 510,355;PD -10,
      355;PD -10,-10;PU"
5340 INPUT "HORIZONTAL LINES ? ";Y$:IF Y$<>"Y" THEN GOTO 5010
5350 GOSUB 5600
5360 PRINT #1,"SP ";P;" ;PD -10,";Y;" ;PD 510,";Y;" ;PU"
5370 GOTO 5340
5400 CLOSE #1:RETURN
5600 PRINT "MOVE PEN TO REQUIRED POINT USING CURSOR KEYS, PRESS
      ENTER WHEN READY+/- TO CHANGE LENGTH OF LABEL"
5610 KEY(11) ON:KEY(12) ON:KEY(13) ON:KEY(14) ON
5620 ON KEY(11) GOSUB 5660:ON KEY (12) GOSUB 5670:ON KEY (13)
      GOSUB 5680:ON KEY(14) GOSUB 5690
5625 REM
5630 XD=0:YD=0:
5640 REM PRINT #1,"PU ";X;" ,";Y;"PU ";X+L;" ,";Y-----
5641 I$=INKEY$
5645 IF I$="+" THEN L=L*1.05
5646 IF I$="-" THEN L=L*.95
5647 IF I$="=" OR I$="-" THEN PRINT #1,"PU ";X;" ,";Y;" ;PU";(X+
      LEN(A$)*L);" ,";Y
5650 IF I$<>CHR$(13) THEN GOTO 5630
5655 RETURN
5660 YD=YD+4:XD=0:GOTO 5700
5670 YD=0:XD=XD-4:GOTO 5700
5680 YD=0:XD=XD+4:GOTO 5700
5690 YD=YD-4:XD=0:GOTO 5700
5700 X=X+XD:Y=Y+YD
5705 LOCATE 1,1:PRINT XD
5710 PRINT #1,"PU ";X;" ,";Y
5720 RETURN 5640
6000 IF B$<"1" OR B$>"8" THEN BEEP:BEEP:RETURN
6010 IF F<>0 THEN COLOR 2:GOSUB 6100
6015 COLOR 4:F=VAL(B$):GOSUB 6100
6017 LOCATE 2,1:PRINT T$(F);" ,";D$(F)" ,";M$(F)" ,";C$(F);:PRINT
      SPACE$(80-POS(1))
6020 RETURN
6100 FOR A=1 TO 500:PSET(A,A(F,A)):NEXT A

```

```

6110 RETURN
6500 FOR A=1 TO 500:PRESET (A,A(F,A)) :NEXT A
6510 RETURN
7000 LOCATE 1,1:INPUT;"MAX VALUE,MIN VALUE ";MAX,MIN:LOCATE 1,1
      :PRINT SPACES(30);
7010 FOR A=1 TO 500:PRESET (A,A(F,A))
7020 A(F,A)=A(F,A)-BOT:IF A(F,A)<0 THEN A(F,A)=0
7025 A(F,A)=A(F,A)/(TOP-BOT)*(MAX-MIN)+MIN
7030 PSET (A,A(F,A)):NEXT A:TOP=0:BOT=0:RETURN
7040 FOR A=1 TO 500:PRESET (A,A(F,A)):A(F,A)=A(F,A)-B
      :PSET(A,A(F,A))
7042 IF A(F,A)<0 THEN A(F,A)=0
7044 NEXT A:RETURN
7050 FOR A=1 TO 500-B:PRESET (A,A(F,A)):A(F,A)=A(F,A+B)
      :PSET(A,A(F,A))
7054 NEXT A:FOR A=500-B TO 500:PRESET(A,A(F,A)):A(F,A)=0:NEXT A
      :RETURN
7060 FOR A= 500 TO B STEP -1:PRESET (A,A(F,A)):A(F,A)=A(F,A-B)
      :PSET(A,A(F,A))
7064 NEXT A:FOR A=B TO 1 STEP -1:PRESET(A,A(F,A)):A(F,A)=0:NEXT A
      :RETURN
7070 RETURN
9000 STOP
9999 FOR A=1 TO 2 STEP 0:A$=INKEY$:IF A$<>"" THEN PRINT ASC(A$)
      :NEXT
10000 GOTO 9999

```

